Master's thesis

2021

Susanne Rosvoll

NTNU
Norwegian University of
Science and Technology
Faculty of Information Technology and Electrical
Engineering
Department of Electronic Systems

Susanne Rosvoll

Fabrication of Supermagnetic Metamaterials

February 2021

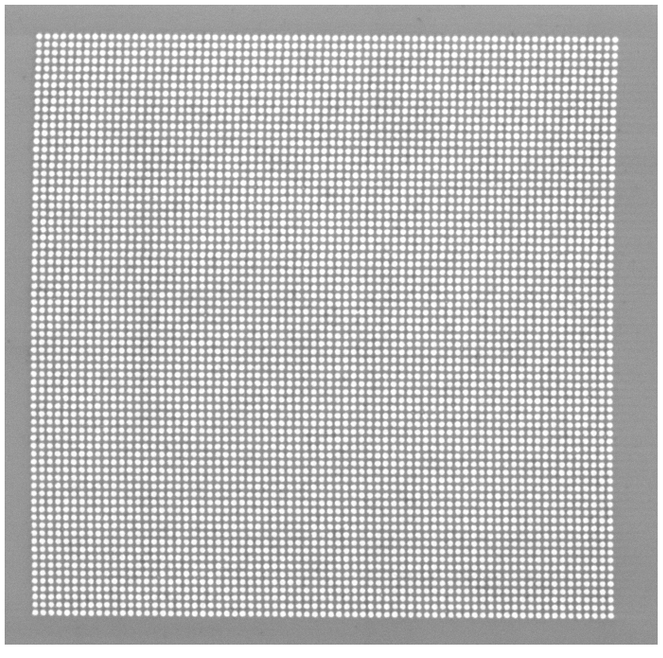

NTNU
Norwegian University of
Science and Technology

NTNU
Norwegian University of
Science and Technology

NTNU

Norwegian University of
Science and Technology

Fabrication of Supermagnetic Metamaterials

Susanne Rosvoll

Nanotechnology
Submission date: February 2021
Supervisor: Erik Folven, IES
Co-supervisor: Anders Strømberg, IES

Norwegian University of Science and Technology
Department of Electronic Systems

Abstract

In recent years, it has been found that a magnetic metamaterial can display signs of supermagnetism, making them a point of interest for both research and possible technological applications. To facilitate the use of these materials in future technologies, investigations into the engineering and tailoring of supermagnetic properties are necessary. Through these investigations, important parameters and requirements for specific properties can be identified. Until now, most research has been devoted to small-scale experiments, which only describes local microscopic composition. The goal of this project is to create samples containing sufficient magnetic material to be characterized by larger-scale traditional methods of magnetic measurement. These measurements will produce data that regards the macroscopic, effective, magnetic arrangement.

This work creates and studies larger patterns of square lattice nanodisks in the single-domain state, which forms a 2D XY-spin system. Large arrays of square lattice single-domain Permalloy disks were fabricated by electron beam lithography and a lift-off process, and subsequently measured in a vibrating sample magnetometer at room temperature. The fabrication process was fine-tuned to the desired parameters of the magnetic system.

We observe that the extended square lattice does not produce the expected superantiferromagnetic state but rather displays signs of superferromagnetism. Investigations suggest that the disk ellipticity and the lattice anisotropy may be interacting to form an unpredicted supermagnetic response. Following this finding, we suggest that further research into magnetic XY-spin systems should include deliberate pattern defects to understand how these may be utilized as a tailoring parameter to create novel magnetic responses and possibly new supermagnetic states.

Sammendrag

De siste årene har studier innen magnetiske metamaterialer funnet tegn på supermagnetisme i enkelte magnetsystemer, noe som gjør feltet attraktivt både for forskning og framtidig teknologi. For å muliggjøre bruken av disse materialene i teknologi behøves forskning i hvordan man kan utvikle og skreddersy supermagnetiske egenskaper til å passe utallige krav og parametere. Frem til nå har mesteparten av forskningen foregått på liten skala, som kun gir informasjon om lokal mikrostruktur. Målet for dette arbeidet er å lage prøver som inneholder nok magnetisk materiale til å karakterisere prøven med større tradisjonelle måleverktøy. Disse resultatene vil kunne gi informasjon om den generelle magnetiske makrostrukturen.

Dette arbeidet fabrikerer og undersøker monodomene disker mønstret i kvadratisk gittergeometri som danner et todimensjonalt XY-spin system. Større områder med mønstret Permalloy ble fabrikkert med elektronlitografi og resist avløftning, og senere undersøkt med et Foner-magnetometer ved romtemperatur. Fabrikasjonsprosessen ble optimalisert for de ønskede parameterne ved det magnetiske mønsteret.

Vi observerer at det utvidede kvadratgitteret ikke avgir magnetisk respons som passer med den forventede superantiferromagnetiske tilstanden, men heller ser ut til å være i den superferromagnetiske tilstanden. Nærmere undersøkelser tilsier at det er mulig en elliptisitet i diskene interagerer med gitterstrukturen for å danne en uforventet magnetisk respons. Som følge av disse resultatene anbefales det videre forskning i supermagnetiske XY-spin system som inkluderer introduserte defekter for å undersøke hvordan disse kan brukes som vilkår for å lage skreddersydde magnetiske responser og muligens nye supermagnetiske tilstander.

Preface

This master thesis was written as a part of a Master of Technology in nanotechnology at the Norwegian University of Science and Technology (NTNU). The work presented was carried out during the autumn and winter of 2020/2021 under the supervision of Assoc. Prof. Erik Folven and co-supervisor Ph.D cand. Anders Strømberg.

The work presented in this master thesis is original and unpublished work done by the author, including all figures, graphs, and micrographs. The exception to this is the VSM measurements. Due to restricted access to the lab during the COVID-19 pandemic, the co-supervisor carried out these measurements.

The Research Council of Norway is acknowledged for the support to the Norwegian Micro-and Nano-Fabrication Facility, NorFab, project number 295864. I want to thank my supervisor and co-supervisor for providing advice, ideas, and knowledge at my disposal. I can say with certainty that this work would not have seen the light of day without their guidance and words of encouragement. Also, I would like to extend my thanks to the kind workers at NTNU Nanolab for accommodating the project, and my co-student Marte Stalsberg for merry co-operation on our lab and thesis work. Lastly, I am in gratitude to Mathias Backsæther for his calm advice and collected demeanor during these 25 weeks. I guess one humorously can say that "opposites attract".

Contents

List of Figures

Acronyms

BSE	Backscattered Electron
CVD	Chemical Vapor Deposition
EBL	Electron Beam Lithography
MFM	Magnetic Force Microscopy
PAC	Photoactive Compound
PEC	Proximity Error Correction
PVD	Physical Vapor Deposition
SAFM	Superantiferromagnetism
SE	Secondary Electron
SEM	Scanning Electron Microscope
SFM	Superferromagnetism
SQUID	Superconducting Quantum Interference Device
VSM	Vibrating Sample Magnetometer
XPEEM	X-ray Photoemission Electron Microscopy

Introduction

Magnetism is without a doubt one of the most fascinating physical phenomena known to man. The invisible force of a permanent magnet has the power to warp and move magnetic objects and has intrigued scientists for over a millennia. Why are humans so fascinated by magnetism, and what are the limits to utilizing its extraordinary powers? Traditionally magnets have been used in compasses [1], magnetic resonance imaging, speakers, and microwave devices [2]. Today, magnets are also commonly found in digital storage applications [3], credit cards, and virtually all electronic devices. The continued research into the subject has uncovered many prospective uses, including superconduction, spintronics, magnetic nanoparticles and more. All substances exhibit some form of magnetism, and it is only the imagination that is holding humanity back from the endless opportunities that magnetism presents. One such proposition is to use magnetic metamaterials for energy-efficient computing.

Motivation

When the transistor was invented in 1947, the main goal was to miniaturize and simplify the bulky vacuum tube computers [4]. However, this achievement only marked the advent of the miniaturization developments to be achieved in the following decades. Moore's law states that "*The complexity for minimum component costs has increased at a rate of roughly a factor of two per year*" [5], which has been interpreted as that the number of transistors on a computer chip should double every two years [6]. Until recently, this prediction has been remarkably accurate due to the extensive research into both semiconductor physics and the fabrication process. Now the industry is at a major pivot-point, as the transistors cannot be any smaller with the current technology. This blockage is due to gate lengths being so small that they allow tunneling of electrons and give rise to irreparable issues with the chip power dissipation [7].

In the last decade, the notion of *more than Moore* has gained traction in the scientific community. The idea is that the end of computation complexity is not necessarily in the hands of miniaturization alone. More than Moore emphasizes the use of novel technologies and techniques, and opens the possibility of abandoning the semiconductor-based transistor altogether. Suggestions have

been made to use 2D semiconductors [8] and 3D transistor structures such as fin field-effect transistors [9] and carbon nanotubes [10] to continue the advancement in the industry. An innovative idea is to create an entirely new type of computing device with field-coupled nanocomputing, which uses what is called nanomagnetic logic (NML) [11]. This approach is different from the use of magnetic materials in quantum computing, as the driver for the computation does not rely on quantum phenomena. To utilize NML and other magnetic technologies in the future, a consistent and well-designed fabrication process must be made to fulfill the requirements posed by this suggested technique. One particular area of interest to achieve magnetic technologies is the research of magnetic metamaterials.

A metamaterial differs from conventional materials in that artificial micro- and nanostructures create new material properties. This structuring entails that creating structures and patterns out of conventional materials can produce drastically different material properties than that of the original material. There are many possible uses for magnetic metamaterials, including use in magnetic computers and computation. Magnetic metamaterials are also of interest in sensor technology [12] and to further explore the physics of magnetic systems [13]. Learning how to tailor and engineer metamaterials is crucial also for these future applications. This work is focused on the fabrication and characterization of 2D XY-spin systems with circular magnetic disks as a continuation of a project carried out in the spring of 2020.

The Field Of XY-spin systems

Whereas most of the field today studies systems such as kagome [14] and artificial spin ice [15], some research has also been devoted to studying 2D XY-spins. In these systems, single-domain magnets are patterned in various designs, the most common being the square, hexagonal, and honeycomb lattices. These systems display long-range ordering of magnetic superspins from inter-disk dipolar coupling, and experience supermagnetism. Studies in these systems have already revealed how they vary with temperature [16], how they may arise both in magnetic nanoparticles and patterned magnets [17, 18], and the prediction and imaging of the type of supermagnetism that arises from the different patterns [19, 20]. Even realizations of how these systems can be used in bit pattern media have been researched [21]. Despite progress in the field, there remains to be done characterization of more extensive areas of magnets, and investigations of macroscopic material properties. In these systems, the magnetic response is often imaged or measured magnet-by-magnet or area by area, but the minimum magnification of X-ray Photoemission electron microscopy (XPEEM) or magnetic force microscopy (MFM) typically limits the imaging of larger areas. It is desirable to examine the hysteresis response of these magnetic systems, as this is a

material property than can be used in tailoring future metamaterials. For this purpose, a larger patterned area must be made to obtain enough magnetic material to have an acceptable signal-to-noise ratio for vibrating sample microscopy (VSM). This need for larger areas covered with microscopic structures pressures the fabrication process, requiring clean room facilities and state-of-the-art instruments and materials.

Project Outline

This project aimed to fabricate relatively large (4 - 16 mm^2) areas of square lattice single-domain Permalloy disks with electron beam lithography (EBL). This fabrication was done with CSAR 62, a positive tone resist, and the accompanying lithographic steps. The metal was deposited using an electron beam evaporation technique. During the process, optimization of several fabrication steps was done. Creating this sample was done to obtain the magnetic response of the patterned array in a vibrating sample magnetometer (VSM) and to examine the hysteresis response for signs of single-domain structures with superantiferromagnetic ordering.

The work is presented in two parts, where Part I contains the background of the project and Part II contains the project outcome. Structurally, the work starts with the background theory and the experimental methods, before the results and discussion concurrently are presented. The decision to present both results and discussion in the same chapter was made to increase the coherency of the work, as some early findings resulted in postliminary changes to the fabrication process. Part I begins with chapter 1 and contains an introduction to magnetism, as well as the notion of supermagnetism. The theory on magnetism is supplemented with fabrication theory in chapters 2 and 3, where chapter 2 introduces the lithography technique, and chapter 3 explores the theory of electron beam lithography (EBL) and scanning electron microscopy (SEM). These chapters are followed by chapter 4, which details the experimental methods, including the characterization process, used in this project. The presentation of the experimental methods marks the conclusion of Part I. Part II contains the results and discussion (chapter 5), conclusion (chapter 6), and finally, the recommendations for further work (chapter 7).

Part I

Theory and Method

Chapter 1

Magnetism

1.1 What is a Magnet?

One of life's greatest mysteries is how most people associate magnetism with the horseshoe magnet, even though this magnet has been irrelevant for over 50 years [1]. The horseshoe magnet is only the tip of the iceberg of what a magnet is and what magnetism does for the everyday life of humanity. This chapter explores the concepts of magnetism, from the general to the highly specific. First, the origin of the magnetic moment is presented, followed by the theory on magnetic fields. A discussion on magnetic materials follows this presentation, before the different magnetic materials are reviewed. The final parts of the chapter are devoted to micromagnetism, and the phenomenon of supermagnetism.

1.1.1 The Magnetic Moment

In short, a magnetic material is a substance comprised of magnetic moments. The total magnetic moment of a substance is comprised of countless microscopic contributions arising from different microscopic sources. Although both the nuclei and electrons of atoms have a magnetic moment, the nucleus moment is a factor $\sim$ 1000 smaller than that of the electron. Therefore, the point of interest lies in determining the magnetic moment arising from the electrons. This section is based on *Introduction to Magnetic Materials* by Cullity and Graham [22] and *Magnetism in Condensed Matter* by Blundell [23].

Quantum Mechanical Origin

Electrons in an atom have two modes of motion that give contributions to the magnetic moment; the orbital angular momentum ($\vec{L}$); and the intrinsic angular momentum ($\vec{S}$). The orbital angular momentum arises from the orbital path of the electron, which can be visualized as the well-known current loop, seen in fig. 1.1a. The intrinsic angular momentum relates to the electron spin, which

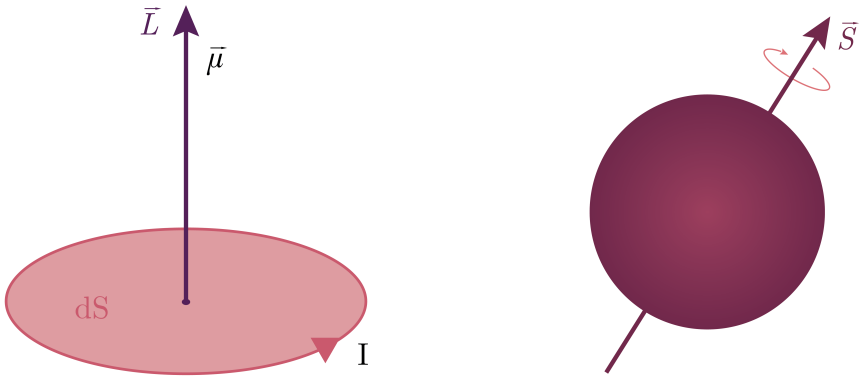

(a) Representation of orbital angular momentum $\vec{L}$.

(b) Representation of intrinsic angular momentum $\vec{S}$.

Figure 1.1: Visual representation of the different angular momentums in an electron.

may be visualized as the electron spinning about its axis, as seen in fig. 1.1b. These visualizations are not scientifically accurate but give a sense of how the magnetic moments arise. A current loop such as in fig. 1.1a produces a magnetic field, of which the dipole moment can be calculated as

$$\vec{\mu}_{\mathrm{L}} = (\text{current}) \cdot (\text{area of loop})$$
$$\vec{\mu}_{\mathrm{L}} = I \int d\vec{S} \tag{1.1}$$

where $\vec{\mu}_{\mathrm{L}}$ is the magnetic moment, I is the current, and $d\vec{S}$ is the loop area. Evaluating the size of this moment takes into account both the orbital path and charge of the electron. The simplest way to do this is to analyze a single-electron atom. The electron creates a current $I = -e/\tau$, where e is the electron charge and τ is the loop period. This period is calculated by $\tau = 2\pi r/v$ where r is the radius and v is the tangential orbital speed. Combining this with the fact that the magnitude of angular momentum must equal to an integer multiple of $h/2\pi$, where h is the Planck constant, the resulting moment is

$$\mu = \frac{eh}{4\pi m_{\mathrm{e}}} \tag{1.2}$$

where m_{e} is the relative mass of the electron. Equation (1.2) results in the contribution to the magnetic moment from one electron due to its orbital motion.

The contribution to the magnetic moment from the electron spin is, in fact, of the exact same magnitude as the contribution from orbital motion. This quantity is known as the natural unit of the magnetic moment and is termed the Bohr magneton (μ_{B}). The spin-moment magnitude can be written as

$$\mu_{\mathrm{s}} = g\mu_{\mathrm{B}} m_{\mathrm{s}} \tag{1.3}$$

where g is the spin g-factor and m_s is the value of the spin quantum number. For electrons, $g \approx 2$ and $m_s \pm 1/2$. Due to the nature of the spin, this results in

$$\mu_s = \mp \mu_B. \tag{1.4}$$

When the magnetic moment of each atom is determined, μ_L and μ_S are combined to determine the total moment.

1.1.2 Magnetic Fields

The contents of this section largely follows chapter 2 in *Introduction to Magnetic Materials* by Cullity and Graham [22].

The total magnetic moment of a permanent magnetic material creates magnetic poles due to the directionality of the total moment. These poles generate a flux of magnetism from the north pole (N) to the south pole (S), which generates a magnetic field $\vec{H}$ as seen in fig. 1.2. This field includes an internal demagnetizing field and an external field due to surface charging. Magnetic fields can also arise from the motion of current as in eq. (1.1). The flux density $\vec{B}$ is tied to the magnetic field $\vec{H}$ by

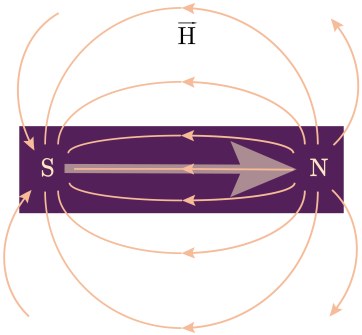

Figure 1.2: The magnetic field from a bar magnet. The larger inset arrow indicates the direction of the sum magnetic moment.

$$\vec{B} = \vec{H} + 4\pi\vec{M}$$

where $\vec{M}$ is the *magnetization* of the magnetic material. The magnetization is the total magnetic moment over the volume of the material, and characterizes the magnetic strength of the material. The magnetic flux density is a useful notation, as shown in Faraday's law of induction

$$\vec{\nabla} \times \vec{E} = -\frac{\delta \vec{B}}{\delta t} \tag{1.5}$$

where $\vec{E}$ is the induced electric field. This entails that for any change in $\vec{B}$ an electric field is induced. The material parameter regarding the ability to interact with is defined as

$$\mu = \frac{B}{H} \tag{1.6}$$

where μ is the *permeability* of the magnetic material. Note that B and H are the field amplitudes, and so the permeability is often presented alongside a field vector. When a magnet is placed in a magnetic field, it alters the shape of the

field depending on the permeability. This effect can be taken advantage of to create, for example, magnetic shields in electronic circuits.

Hysteresis

When investigating the magnetic nature of a material, it is common to create a hysteresis loop. The hysteresis loop can be used to characterize important material properties such as the moment switching field. An initially depolarized magnet is placed in a magnetic field, and the field strength is gradually increased. When the material has reached *magnetic saturation*, M_s, the field strength is gradually decreased toward zero. Magnetic saturation is reached when all magnetic moments in the material are parallel and in the same direction as the applied field. A permanent magnetic material will now display remanent magnetization and the current magnetic state is dependent on the previously applied field. This phenomenon is known as hysteresis.

Similarly, if the field strength continues below zero, which in this reference system implies that the field is pointing in the opposite direction, the material will eventually reach a point saturation again. Increasing the field strength will create a loop back to the first tableau of saturation, and this is what is known as a hysteresis loop. Figure 1.3 shows the expected hysteresis loop of a ferromagnetic material and how to read out M_s and the coercive field strength.

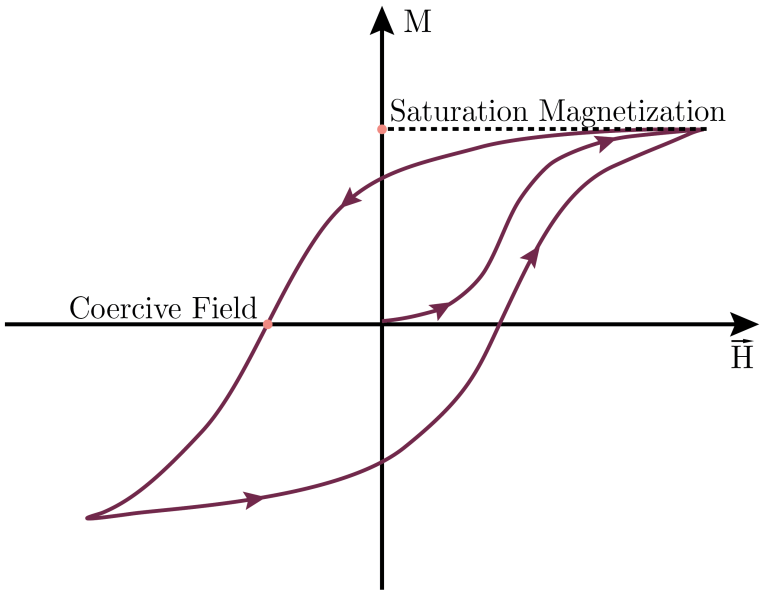

Figure 1.3: A typical hysteresis curve for a ferromagnetic material.

1.2 Magnetic Materials

In an atom, there is typically more than one electron contributing to the magnetic moment. The sum of these moments cannot be rigorously calculated but, instead, must be determined experimentally. The different overall arrangements can be visualized; either all moments are oriented to cancel each other out, or the moments only partially cancel, which results in a material with either a net magnetic moment or no net magnetic moment [22]. From this point on, when referring to the magnetic moment, it is the atomic magnetic moment that is meant, not the moment of individual electrons.

1.2.1 Magnetic Susceptibility

The magnetization ($\vec{M}$), is a continuous vector field except at the edges of the magnetic material [23]. A linear and isotropic magnet will obey [24]

$$\vec{M} = \chi_{\mathrm{m}} \vec{H} \tag{1.7}$$

where χ_{m} is a magnetic quantity termed the *magnetic susceptibility*. Following this equation, the magnetic susceptibility identifies the amount of magnetization in a material due to an applied magnetic field. As the magnetic moments will prefer to align with the applied field, this increases the magnetization. The notion that an increased magnetic field will increase the magnetization is only true for materials with predominantly ferromagnetic or paramagnetic responses. A negative susceptibility would lead to a negative magnetic response, such as in diamagnetism. Different magnetic susceptibilities will lead to different formations of moments, leading to different magnetic materials. This phenomenon is explored in the following sections.

1.2.2 Diamagnetism and Paramagnetism

If the magnetic susceptibility is negative and of low magnitude, the material is diamagnetic [23] and exhibits *negative magnetism* [22]. Intuitively, this means that the magnetic moments will prefer to align against the applied magnetic field. This reversed alignment occurs to lower the effective current of the electron orbit, so when discussing a diamagnetic material one cannot have a spontaneous net magnetic moment due to unpaired electrons. The exception is under the influence of a field, where a diamagnetic material will display a net magnetic moment. All materials exhibit a degree of diamagnetism, but it is typically ignored due to its low magnitude compared to the other contributions of magnetic energy.

On the other hand, paramagnetism is exhibited in materials with a weakly positive magnetic susceptibility. Here, the magnetic moments prefer to align

with the applied field. The main difference between a paramagnetic and ferromagnetic material is that the paramagnetic material does not display magnetic remanence after the application of a magnetic field. Rather, the moments will relax to a random state. A more detailed description of diamagnetic and paramagnetic materials can be found in *Magnetism in Condensed Matter* by Blundell [23].

1.2.3 Ferromagnetism

The magnetic moments may align spontaneously for a material with high magnetic susceptibility, regardless of any applied magnetic field. These materials are known as ferromagnetic, and the spontaneous magnetization occurs due to the exchange energy from electrostatic interaction between neighboring atoms [23].

Exchange Interaction

Consider a simple system of two neighboring atoms, each with one free electron. The electrons have positions $\vec{r_1}$ and $\vec{r_2}$, and their wave functions are $\psi_A(\vec{r_1})$ and $\psi_B(\vec{r_2})$, respectively. The joint state can be written as a product of the single states, but must obey rules of exchange symmetry

$$\Psi(\vec{r_1}, \vec{r_2}) = \phi(\vec{r_1}, \vec{r_2})\chi(\vec{r_1}, \vec{r_2}) \tag{1.8}$$

where ϕ is the spatial part, and χ is the spin part of the wave function. Electrons are fermions, and so the wave function is anti-symmetric

$$\Psi(\vec{r_1}, \vec{r_2}) = -\Psi(\vec{r_2}, \vec{r_1}) \tag{1.9}$$

As a consequence, if the spatial part of the wave function is symmetric, the spins must be in the anti-symmetric singlet state χ_S ($S = 0$). Similarly if the spatial part is anti-symmetric, the spins must be in the symmetric triplet state χ_T ($S = 1$). The energies of the respective states can be written, assuming normalized spin parts, as

$$E = \int \Psi^*(\vec{r_1}, \vec{r_2})\hat{H}\Psi(\vec{r_1}, \vec{r_2})d\vec{r_1}d\vec{r_2} \tag{1.10}$$

where $\hat{H}$ is the Hamiltonian. The spatial part can be written as

$$\phi_S(\vec{r_1}, \vec{r_2}) = -\phi_S(\vec{r_2}, \vec{r_1}) \tag{1.11}$$

$$\phi_T(\vec{r_1}, \vec{r_2}) = +\phi_T(\vec{r_2}, \vec{r_1}) \tag{1.12}$$

$$\phi_{S/T} = \frac{1}{\sqrt{2}}[\,\psi_A(\vec{r_1})\psi_B(\vec{r_2}) \mp \psi_A(\vec{r_2})\psi_B(\vec{r_1})] \tag{1.13}$$

for the singlet and triplet states respectively. The Pauli exclusion principle states that no two electrons may have the same position and quantum number, and so electrons in the triplet state may not be found in the same position.

The eigenvalue of the joint state of the electrons is either $1/4$ (singlet) or $-3/4$ (triplet), from this the effective Hamiltonian can be written as [23]

$$\hat{H} = (1/4)(E_{\mathrm{S}} + 3E_{\mathrm{T}}) - (E_{\mathrm{S}} - E_{\mathrm{T}})\vec{S}_1\vec{S}_2 \tag{1.14}$$

where the first term is the constant energy, and the second is the spin-dependent energy. The difference between the energy of the singlet and triplet state is

$$E_S - E_T = 2\int \psi_a^*(\vec{r}_1)\psi_b^*(\vec{r}_2)\hat{H}\psi_a(\vec{r}_2)\psi_b(\vec{r}_1)d\vec{r}_1 d\vec{r}_2. \tag{1.15}$$

The splitting of energy between the singlet and triplet state is $2J$ [1], where J is the exchange integral

$$J = \frac{E_S - E_T}{2} = \int \psi_A^*(\vec{r}_1)\psi_B^*(\vec{r}_2)\hat{H}\psi_A(\vec{r}_2)\psi_B(\vec{r}_1)d\vec{r}_1 d\vec{r}_2 \tag{1.16}$$

following from Equation 1.15. Using the spin part of Equation 1.14 and combining with Equations 1.15 and 1.16, the formula for the exchange energy (E_{ex}) can be written as

$$E_{\mathrm{ex}} = -2J\vec{S}_1 \cdot \vec{S}_2 = -2J\vec{S}_1\vec{S}_2 \cos\theta \tag{1.17}$$

where θ is the angle between the spins. If J is positive, the system will be at an energetic minimum for parallel spins ($\cos\theta = 1$), and similarly if J is negative the system will prefer antiparallel spins ($\cos\theta = -1$) [22]. This entails that a positive exchange integral is a condition for obtaining ferromagnetism. A material with a positive exchange integral will have exchange interacting spins that align parallel, and create spontaneous magnetization.

Stoner Criteria

Which materials are subject to a positive exchange integral? Examining the band structure of ferromagnetic metals such as Fe, Co, and Ni might give a clue. All these metals have a large density of states around the Fermi level. This can lead to spontaneous spin-split bands, in which one of the spin directions become energetically favorable. The full derivation of the so-called Stoner model is outside the scope of this thesis, and the interested reader may read about the derivation of this model in Chapter 7.3 of [23].

1.2.4 Antiferromagnetism

In an antiferromagnet, the magnetic moments align antiparallel to create a zero net magnetic moment. Building on the explanation of ferromagnetism, the explanation for antiferromagnetic ordering lies in the exchange integral. A negative exchange constant J makes antiparallel spins energetically favorable. The exchange interaction is, therefore, also the reason for antiferromagnetism. The difference between ferromagnetic and antiferromagnetic alignment is shown in fig. 1.4. When the moments are aligned antiparallel, but the magnitude of the opposite directions is not equal, the material has a net magnetization and is termed ferrimagnetic. While this form of magnetism is not directly used in this work, the antiferromagnetic state is used analogously for the metamaterial magnetic state.

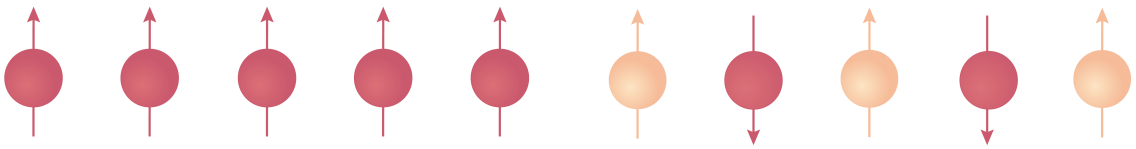

(a) Ferromagnetic ordering **(b)** Antiferromagnetic ordering

Figure 1.4: Magnetic ordering of microscopic spins for the ferromagnetic and antiferromagnetic case.

1.2.5 Temperature Dependence

The magnetic behavior of a material is often temperature-dependent. The paramagnetic and antiferromagnetic phenomena cannot be distinguished merely on field measurements, as they both have a net magnetization of zero. Sweeping measurements over a range of temperatures reveal a different story. Materials that exhibit antiferromagnetic responses only do so below a temperature known as the Néel temperature T_N. Similarly, the spontaneous magnetization associated with ferromagnetism does not occur above the Curie temperature, and the material is paramagnetic due to randomized spins. The Curie and Néel temperatures are analogous, and the associated magnetic phase transitions occur due to thermal energy $E_{\text{th}} = k_{\text{B}}T$, where k_{B} is the Boltzmann constant and T is the temperature in Kelvin. The phase transitions occur as the thermal energy contributes to the increase in high energy electrons that interfere with the order and alignment of magnetic moments.

1.3 Micromagnetism

The atomic magnetic moments described in earlier sections are not individually probed, but rather the entire material is viewed as a micromagnetic system. As discussed in Section 1.2.3, the magnetic moments in a ferromagnet are aligned without the presence of a magnetic field. In imagining a ferromagnetic material, it might be tempting to envision that all magnetic moments point in the same direction. However, other energetic contributions facilitate the formation of magnetic *domains*, an area-confined region in which all magnetic moments are aligned, separated from other regions by a domain wall.

Four major contributions are working either with or against each other to influence the microstructure of the magnet, all outlined in the sections below.

1.3.1 The Energy Equation

Shape Anisotropy

It is not without reason that the wheel of a car is round. The geometric properties of a substance can drastically change the substance abilities, and the same is true for ferromagnets. A fundamental property of magnetism is captured in one of Maxwell's equations

$$\nabla \cdot \vec{B} = 0 \tag{1.18}$$

which states that there are no magnetic monopoles. If all magnetic moments are aligned, some are necessarily aligned perpendicular to the magnet surface, but as Equation 1.18 states, this must create surface charge, inducing an external magnetic field. The creation of this demagnetizing field has an energetic cost, and this is termed the demagnetization energy

$$E_{\mathrm{D}} = -\frac{\mu_0}{2} \int \vec{M} \cdot \vec{H}_{\mathrm{d}} \, dV \tag{1.19}$$

where μ_0 is the magnetic permeability of the material and $\vec{H}_{\mathrm{d}} = -\vec{N}_{\mathrm{d}}\vec{M}$ is the demagnetizing field. The energetic contribution from shape anisotropy is lowered when the magnetic moments align along the surface direction. For a rectangular

(a) Hard Axis **(b)** Easy Axis

Figure 1.5: The shape anisotropy of ferromagnetic needles create easy and hard axes of moment orientation.

and two-dimensional case, this seems intuitive, forming four distinct domains as seen in fig. 1.6. In the case of a circular two-dimensional disk, however, there are no distinct domains. The magnetic moments may prefer to create flux closure loops with out-of-plane vortex cores. This loop-state is in an energetic battle with the exchange energy, and as described in section 1.3.3 it is possible to override the vortex state and create single-domain disks if the magnet is small enough. The shape anisotropy can create preferred axes of orientation, as seen in fig. 1.5, where the preferable axis is termed the *easy* axis, and the non-preferable is termed the *hard* axis.

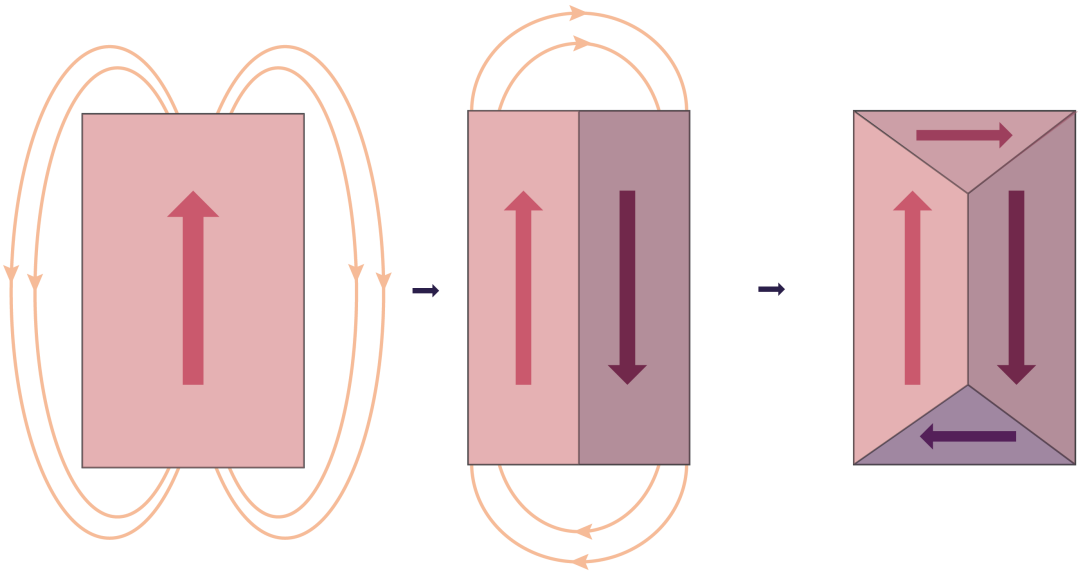

Figure 1.6: Domain formation to minimize energy expended on external field for a rectangular ferromagnet.

Magnetocrystalline Anisotropy

The atoms contributing to the magnetic moment are often part of a crystal lattice. Magnetization is coupled to the lattice via spin-orbit coupling, and this leads to a magnetocrystalline anisotropy, where the energetically preferable state is when the magnetic moments align along with the principle directions of the crystal lattice. These preferable axes will work either with or against the easy axis arising from shape anisotropy when determining magnet microstructure. When examining the energetic contribution of magnetocrystalline anisotropy, different crystal lattice configurations have separate formulas. Considering the energy arising from a cubic crystal lattice

$$E_k = K_0 + K_1(\alpha_1^2\alpha_2^2 + \alpha_2^2\alpha_3^2 + \alpha_3^2\alpha_1^2) + K_2(\alpha_1^2\alpha_2^2\alpha_3^2) + ... \tag{1.20}$$

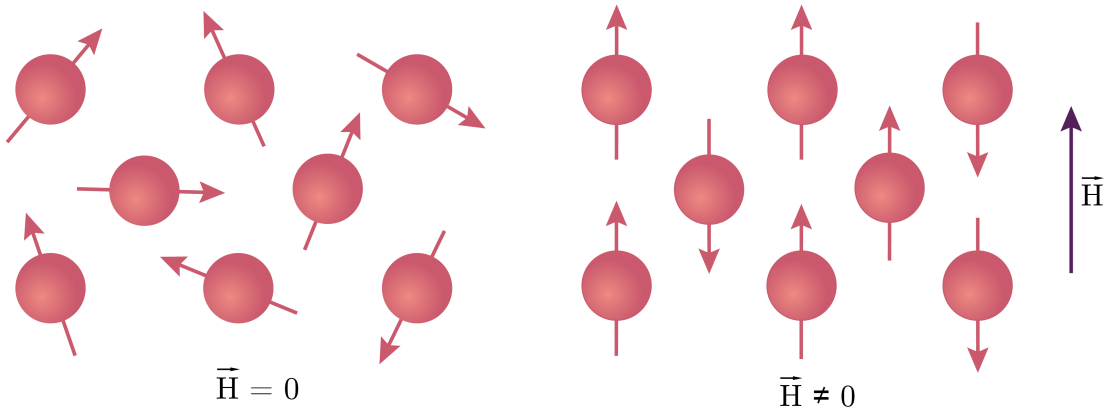

(a) Random ordering of moments

(b) Moments mostly aligning with field

Figure 1.7: Alignment of microscopic magnetic moments with an applied field.

where $K_{0,1,2...}$ are constant and material dependant, and $\alpha_{1,2,3}$ are direction cosines of M_s [22]. For a hexagonal crystal lattice the equation is

$$E_k = K_0 + K_1 \sin^2\theta + K_2 \sin^4\theta + ... \tag{1.21}$$

where θ is the angle between the z-axis and M_s. This yields a *uniaxial* anisotropy for positive K-values. The magnetocrystalline anisotropy is often considered during the material selection in a fabrication process, as it is an intrinsic property to the material. If a material has strong magnetocrystalline anisotropy, it is known as a hard ferromagnet, and similarly for a weak magnetocrystalline anisotropy it is called a soft ferromagnet. Polycrystalline materials will effectively have a negligible magnetocrystalline anisotropy.

Zeeman Energy

Sometimes the system is subject to an external magnetic field, which gives rise to an energy

$$E_H = \mu_0 \vec{M} \cdot \vec{H}_a \tag{1.22}$$

where E_H is the Zeeman energy and $\vec{H}_a$ is the applied magnetic field. There is an energetic cost to the magnetic moments associated with not aligning to the direction of the field, and so increasing the field strength will increase the probability that the moments have aligned. This feature is exploited when characterizing magnetic matter to create hysteresis loops. Figure 1.7 shows how magnetic moments prefer to align along with the direction of the applied field.

Exchange Energy

As detailed in section 1.2.3, the condition for a ferromagnetic material is the exchange energy. This energetic contribution will come into play when discussing domain formation, as the exchange interaction entails that the system energetically prefers the magnetic moments to align. The formula for exchange energy is stated in eq. (1.17).

The Final Equation

All the contributions discussed above must be evaluated in light of the other when trying to determine the microstructure of the magnetic material

$$E = E_{\mathrm{D}} + E_{\mathrm{K}} + E_{\mathrm{H}} + E_{\mathrm{ex}}. \tag{1.23}$$

The shape anisotropy may contribute in the creation of domains, whereas the magnetocrystalline anisotropy determines which directions the moments will prefer to align within those domains. Should the shape be at odds with the crystalline directions, more or fewer domains may arise. The exchange energy will contribute to keeping the moments aligned, working against the formation of domains, and add to the energetic price of the domain walls separating each domain. Finally, the Zeeman energy is applicable when there is an applied magnetic field and will contribute in variable ways depending on field direction and magnitude. Figure 1.5 shows an example of the creation of domains, where the exchange energy and energy from shape anisotropy are the two relevant parameters.

1.3.2 Domain Walls

Separating the regions of aligned magnetic moments are the *domain walls*. More of a figurative than a literal wall, these regions vary in thickness and contain transitionally rotating moments so that there is no abrupt change in moment direction which would entice a high energetic price regarding exchange energy. Typically, one distinguishes two types of domain wall, *Bloch walls* and *Néel walls*. The main difference between these sub-types is how the internal moments rotate to accommodate the bordering magnetic domains, and an exhaustive explanation can be read in chapter 9.2 in [22]. The main characteristic of Bloch walls is the out-of-plane rotation in the wall, whereas the moments in the Néel wall rotate in-plane. The Néel wall-type is prominent when the material film thickness decreases to become comparable to the width of the domain wall.

1.3.3 Monodomain Magnets

Magnetic materials can be single-domain if the material is under a certain critical size [25]. This occurs as the energetic price of creating domain walls becomes to high compared to the savings in demagnetization energy, and the energetic cost of the out of plane vortex core is too high. For round particles, it makes sense to use the parameter of critical radius. The critical radius r_c can be found by [25]

$$r_c \approx 9\frac{(AK_u)^{1/2}}{\mu_0 M_s^2} \tag{1.24}$$

where A is the exchange stiffness and K_u is the uniaxial anisotropy constant. The critical radius is dependent on the properties of the material. When discussing monodomain magnetic disks, disk thickness is also an important parameter. Reducing the film thickness will eventually trap the moments to the motion in the XY-plane. This evolution is similar to the shift from Bloch to Néel walls.

Important Note

The term monodomain implies that all internal magnetic moments are aligned. This is generally not the case, as there will most certainly be edge effects as a result of the shape anisotropy. For a sphere or disk, this will have the edge moments align with the edge direction and so the moments of monodomain specimen are only approximately aligned.

1.4 Supermagnetism

Magnetic ordering due to dipole interaction between individual and spatially separate monodomain magnets is known as *supermagnetism* [25]. Taking advantage of this phenomenon realizes multiple opportunities to engineer magnetic materials with the required features without relying on the magnetic parameters of the metal. At a micro-level, the dipole energy is small compared to the thermal energy, and so its effects are imperceptible. However, at the macro-level the dipoles from so-called *superspins* are much larger in energy, and so the interaction gives rise to long-range magnetic ordering in certain systems. This section describes how superspins align in supermagnetic states, and how these properties are utilized to create new magnetic metamaterials. The section mostly follows the review by Bedanta [25] unless otherwise stated.

1.4.1 The Superspin

When a magnet is single-domain, one can approximate the total magnetic moment to be pointing in one direction, known as the *superspin* of the magnet. A system of exchange-isolated superspins will behave much like a system of atomic spins, so studying these islands may also give valuable insight into how magnetism works. To achieve exchange-isolation, monodomain disks are spatially isolated at a distance at which the exchange interaction is negligible while maintaining a distance where dipolar interactions may occur. Though the islands may be isolated spatially, the superspins will still interact with their environment. Much like for magnetic atoms, thermal fluctuations may randomize the superspins at high enough temperatures. With the effects of anisotropy, the superspins can also maintain a hard and easy axis. The notion of superspin replaces the atomic magnetic moment in a magnetic metamaterial, and the ability to fabricate these single-domain magnets give the opportunity of building a metamaterial with the desired spin-parameters.

1.4.2 Stoner-Wohlfarth Model

Stoner and Wohlfarth studied the magnetization reversal of single-domain elliptical magnets, and their calculations led to the Stoner-Wohlfarth (SW) model, which describes the magnetic response of these magnets [26]. The main assumptions of the SW model are that the particle has *(a)* coherent rotation of the magnetization, and *(b)* negligible interaction with other particles. A magnetic field was applied at an angle to the easy axis, and for a spherical particle they found that the hysteresis curves would vary for different angles. The model is applicable to systems that befit assumptions *(a)* and *(b)*.

1.4.3 Supermagnetic States

Similar to micromagnetic systems, there is a clear temperature dependence for magnetism in these supermagnetic systems. For non-interacting particle systems, the thermal limit is

$$k_B T >> \Delta E_B = KV \tag{1.25}$$

where ΔE_B is the activation energy, K is the anisotropy constant and V is magnet volume. When this temperature is reached, the thermal energy randomizes the superspins, and the system becomes superparamagnetic. The temperature for which this happens is called the single-particle blocking temperature. Note that when the magnets are interacting, the total free energy of the system is more important than that of a single particle, and a system will maintain some form of order even above the single-particle blocking temperature.

The term *superferromagnetism* (SFM) refers to the ferromagnetic ordering of superspins. This occurs in highly ordered systems of particles, such as patterning monodomain magnets in a hexagonal lattice, as seen in fig. 1.8a. Here, the dipole interactions align the spins. Note that this will be dependent on magnetic material and pattern spacing, as these dictate the magnitude of the dipole interaction. Similarly, *superantiferromagnetism* (SAFM) refers to antiferromagnetic ordering of superspins, but requires different patterning lattice. The magnets should be arranged in a square pattern, as seen in fig. 1.8b. For other supermagnetic state such as super spin glass, the reader is directed to the relevant sections of [25].

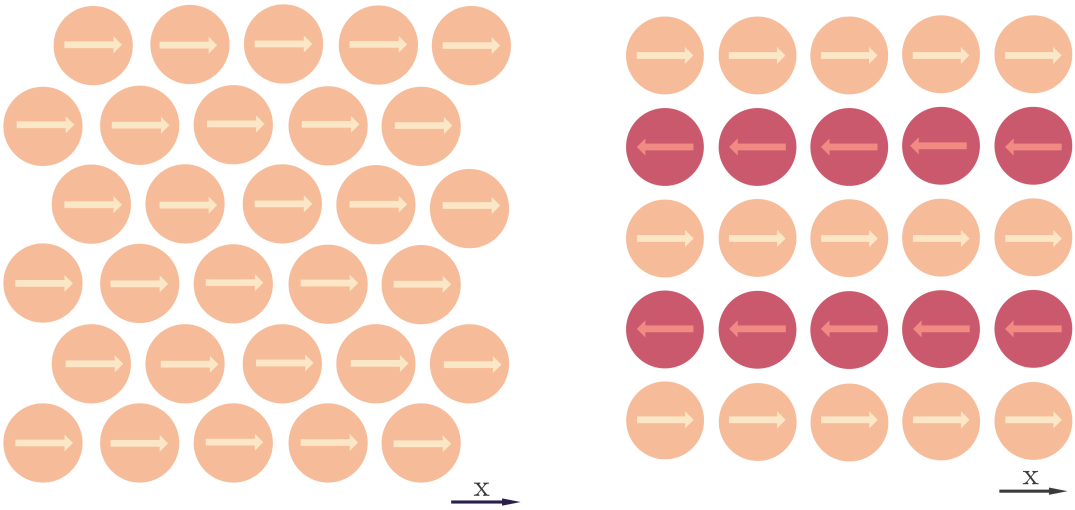

(a) SFM state in hexagonal lattice **(b)** SAFM state in square lattice

Figure 1.8: Alignment of microscopic magnetic moments with an applied field in the x-direction.

1.4.4 Engineering Magnetic Properties

There is a significant difference in the fabrication of magnetic nanoparticles suspended in fluids and artificial patterned magnets. This section will focus on the fabrication of nano-patterned assemblies on substrates. The creation of magnetic metamaterials relies heavily on engineering the magnetic properties of the structures. Permanent magnetic material patterned in different ways gives rise to different supermagnetic states, and so research in the field focuses on simulating and fabricating different patterns and structures to characterize what gives rise to different supermagnetic states.

When analyzing by simulations to predict the supermagnetic ordering, the simulations become computationally costly over many magnets. For analysis of larger magnetic systems, it might be easier to fabricate the system in suggestion.

Before fabrication, smaller-scale simulations may be done in order to predict the magnetic behavior of the system. Whereas the limitations of simulating a magnetic system are the large number of magnets, the limitation of the fabrication process is quite a different problem. The small size necessary to keep the magnet single-domain, while balancing the fine line of maintaining dipole interaction while not having exchange interactions is difficult, as the exchange isolation entails that no magnet must adjoin or touch another. This restriction means there is little margin for fabrication error.

Anisotropy

Different shapes and magnetic materials will contribute to the preferred easy axis, which will influence the magnetization and superspin direction. In general, magnets below a certain thickness will prefer to keep the magnetic moments in one plane, due to the energetic cost of the demagnetizing field as presented in eq. (1.19). There is no shape anisotropy in the plane with a thin circular disk, as all directions are equal. In addition, choosing a polycrystalline magnetic material will render the magnetocrystalline anisotropy negligible. With no preferential axis, there is an opportunity to create SFM and SAFM patterns such as in fig. 1.8, as the dipoles can reside in any direction but prefer to align with each other. Shape anisotropy may also be intentionally patterned into a system to examine directional properties or novel supermagnetic ordering.

Chapter 2

Lithography

What is lithography?

One of the key methods for the fabrication of micro-and nanoscale structures is the process of lithography. In the world of art, the term mainly refers to a technique for creating art-print, hailing to the original lithographic oil and water techniques invented[1] in the late 18th century [27]. However, the term lithography is something entirely different when it comes to fabrication. Photolithography is the foundational technique for mass production of semiconductor technology in the world today, much due to its speed and ability to upscale the fabrication of IC-chips. During the late 20th-century technology surge, the electronic consumer devices decreased in size while increasing their output, meaning the semiconductor industry was under pressure to create smaller and smaller transistors and circuits while maximizing their abilities. Therefore, the industry has devoted considerable funds to research in the area, exploring the optimization of both optical and electron beam lithographic techniques.

The lithographic process rests on a couple of principles. First, a material known as a resist is used, and this material must react to exposure by radiation or electrons. Secondly, the critical dimension of the structures that are to be created must not exceed the limits set by these exposure methods. In this chapter, the working principles of the resist are described before the fabrication process is presented in order of execution. This chapter focuses on the lithography process basics, whereas chapter 3 contains details specifically regarding electron beam lithography (EBL).

[1] One must note the possibility that this technique could have been utilized before a Caucasian male claims to have invented it.

2.1 Resists

The resist is the main component of the process. Research in the field since the late '50s has greatly improved the available resolution of lithography regarding to the exposure process and the resist. A resist can be composed of many different chemicals and materials but is commonly comprised of a resin, a photoactive compound (PAC), and a solvent [28]. The resin gives the material structure and chemical properties [29], the PAC is the reactive substance that changes material solubility, and the solvent is to ensure even distribution when coating by keeping the resist in a liquid form until applied to a wafer.

2.1.1 How does it work?

The resist contains reactive compounds that change solubility according to the amount of light exposure it has been subject to. Depending on the type of resist, the exposed area becomes more soluble, called a positive resist, or the exposed area becomes less soluble and called a negative resist. This difference in solubility is exploited by removing the more soluble areas during the development process. The different resist types are utilized to create different structures depending on the desired pattern and exposure type, and their differences can be seen in fig. 2.1.

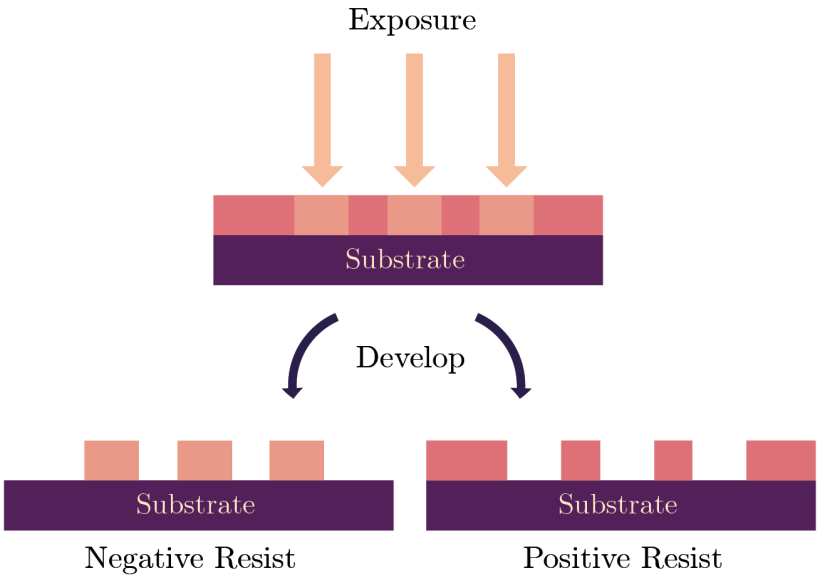

Figure 2.1: Figure of the post-development difference in the remaining structure between negative and positive resists.

Exposure by Photoradiation

The desired pattern is irradiated onto the resist by passing the radiation through a fabricated mask. Depending on resist thickness, the radiation will reflect off the substrate surface and interfere with the incoming radiation. This interference can lead to the formation of standing waves and swing curves [28], which alter the energy dosage delivered to the resist. To combat this effect, a bottom anti-reflectant coating (BARC) can be used. In a positive resist, the PAC is a long-chain polymer, and radiation breaks this polymer into smaller pieces by chain secession, making it more soluble [30]. Similarly, for a negative resist, the radiation allows the originally small polymer chains to form longer polymer chains. Negative photoresists are suitable for creating the undercut side-wall structure, an inward slanted wall, which is particularly handy for the metal deposition pattern transfer. There are several other types of photoresist, and not all work by having PAC-containing polymers.

Exposure by Electrons

For electron exposure, the PAC also often contains polymers. The typical example of a positive electron resist is poly-methyl methacrylate (PMMA). In PMMA, the polymer chains are so long they require more than one electron scission event to become soluble [31]. The negative resists are similar to the photoresist case, where the electrons make the material less soluble. More information on the EBL process can be read in section 4.3.2.

2.1.2 Process Parameters

On the subject of deciding for a resist, the important resist parameters are the *contrast* and *sensitivity*, viewed in light of the desired feature sizes [32]. The sensitivity of the resist determines how much exposure is needed to irradiate the resist down to the substrate. Development curves can be used to examine the resist sensitivity. These curves are created by exposing larger areas with different exposure doses and examining if there is any remaining resist. The amount of remaining resist is plotted against the exposure dose, and the dose-to-clear is the dose where there is no residual resist. If this exposure dose is low, the resist has a high sensitivity, and vice versa for a high exposure dose. There are, however, many factors that contribute to this parameter, including the exposure system parameters, resist thickness, and pattern density [30]. The many contributing factors necessitate exposure dosage tests to determine the correct exposure parameters for the specific process.

The contrast is a measure of how sharp edges the resist can create, defined as the development curve slope. For smaller *critical dimensions* of the structure, the preferred resist should have low sensitivity and high contrast.

2.2 Fabrication Process

This section presents a typical lithography process, with the steps presented in the order of execution. Figure 2.2 shows a schematic of the process.

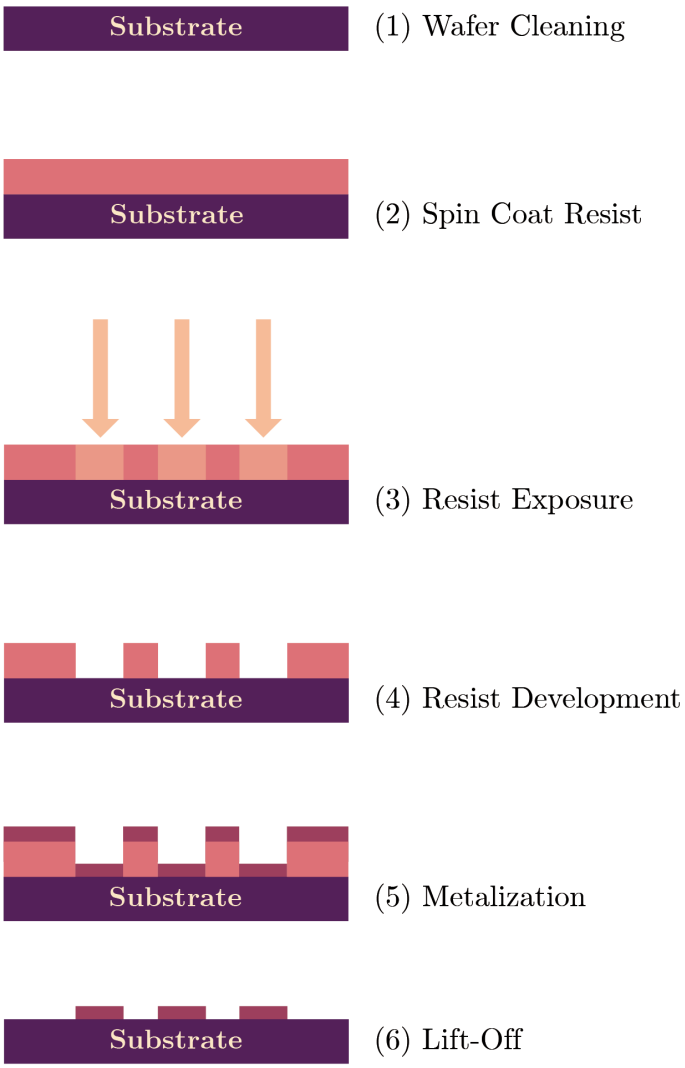

Figure 2.2: Schematic of a typical lithography process. The sizes in the figure are not necessarily to scale.

2.2.1 Substrate Preparation

Wafer Cleaning

The process begins by preparing a substrate by a thorough cleaning. The chosen substrate is often a Si(100) or Si(111) wafer [33]. These steps are to improve the resist adhesion to the substrate, and remove any surface impurities that may distort or destroy the finished structures later in the fabrication process.

There are several methods to clean the surface of a substrate: wet chemical methods such as the RCA procedure or submerging the wafer in other solvents such as acetone, gas-phase techniques such as HF vapor, plasma cleaning, and UV radiation [34]. All methods have their own strengths and weaknesses, so using a combination of several methods is standard practice. The goal is to remove any contamination without interacting with the wafer and avoid introducing new contamination in the form of residue. For a more comprehensive description of the pre-process cleaning of silicon wafers, see [34].

Dehydration Bake

To improve the resist adhesion, it is essential to remove any *surface hydration*. Wet chemical cleaning processes can leave behind molecules of water and solvent, and therefore the sample should be heated to evaporate any water or solvent residue. This evaporation can be achieved by baking on a hotplate or in an oven at adequate temperatures before further processing.

Wafer Priming

Some resists require an extra step to adhere to the wafer surface, and this is done by applying a primer that bridges the resist and wafer. An example of a primer is hexamethyldisilazane (HMDS), which ties up any water on the silicon surface [29]. The primer is applied by the vapor prime or spin coating method.

2.2.2 Spin Coating

Although there are several methods to disperse resist evenly onto a wafer, the most common is spin coating. In spin coating, the wafer is spun to create a centripetal force to evenly spread the resist onto the wafer, as seen in fig. 2.3. There are four basic steps to spin coating [29]:

1. **Dispense** - Resist is deposited onto the wafer
2. **Accelerate** - The wafer is spun up to the required speed to spread the resist
3. **Spin off** - Excess resist is spun off to create an even surface
4. **Evaporation** - The wafer spins for an extra time for solvents to evaporate

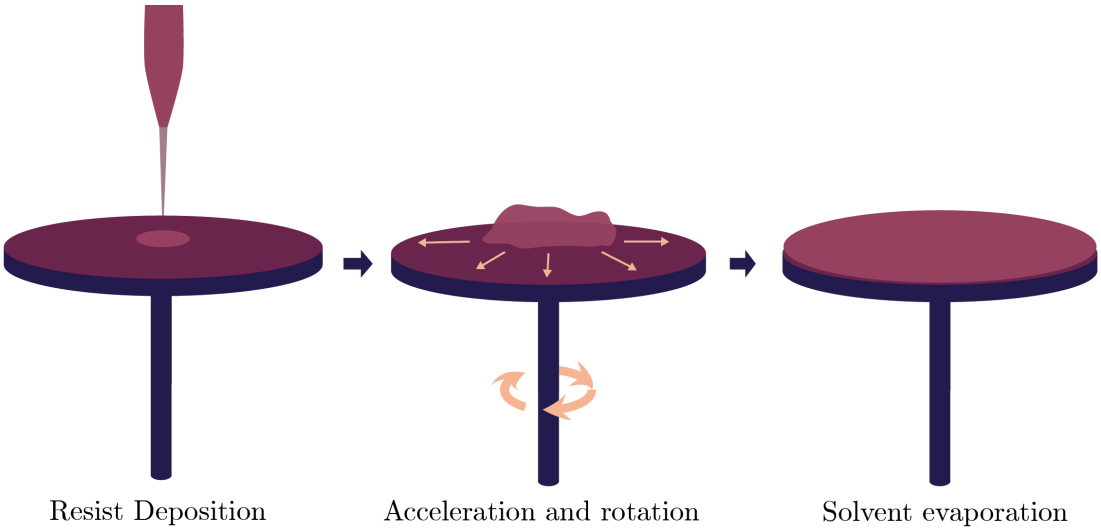

Figure 2.3: Schematic of the spin-coating procedure.

The wafer is attached to the rotation system by a vacuum chuck and is covered during spinning to prevent resist from contaminating the cleanroom. The timing and speed parameters of the acceleration and spinning steps depend on the resist viscosity and desired film thickness. After spin coating, the wafer is also baked to remove the remaining solvents in the resist. The typical spin coated resist thickness varies from 100 nm to 1 µm.

2.2.3 Exposure

After the sample has been coated in resist, the desired pattern is created by exposure. The exposure type varies depending on the resist being used. For photolithography, the exposure is done with electromagnetic radiation with wavelengths of about 400 - 800 nm, and patterns are usually achieved by a mask that physically blocks the radiation from hitting certain parts of the resist. When a process contains multiple layers and exposure sequences, the mask typically includes alignment marks to achieve precise overlapping exposures.

A physical mask is too labor-intensive for single exposures, as the mask fabrication process is done with an EBL method. The strength of this is that the mask can be reused multiple times, and so photo-radiation is favored in mass production. EBL uses electrons and a direct-writing method, where the electron beam is directed only over areas that need to be exposed according to the digital mask. Depending on the beam diameter, this process can be time-consuming, and so electron exposure is only done when the structure size calls for it. Some photolithography systems are also able to use digital masks and mask-less alignment. After exposure, some resists require a post-exposure baking (PEB) step.

2.2.4 Development

The exposure causes the resist to be of either higher or lower solubility than the surrounding resist. The low solubility areas must now be removed so that the remaining structures can withstand the pattern transfer process. The removal of soluble resist is done by development, a process in which a developer appropriate to the resist is applied to the substrate and removes soluble areas. The process must be meticulously timed, as both under- and overdevelopment may cause detrimental effects to the remaining structure. If the resist is underdeveloped, the structure walls are sloped, and there may be remaining resist covering the substrate in unwanted areas. Conversely, if the resist is overdeveloped, the developer will have started to eat away at the cross-linked areas of resist, and the structure walls appear rough and jagged, and this possibly leads to poorly defined results.

2.2.5 Pattern Transfer

Once developed, it is time to transfer the structure to the desired material, typically achieved by either additive or subtractive pattern transfer. In additive techniques, a thin film of metal is applied atop the resist, whereas in subtractive methods, the resist is patterned onto a layer of metal and is used as a mask for removing the metal. An example of a subtractive technique is etching. The etching is done using either liquid or gas chemicals, or ions such as in reactive ion etching (RIE), to remove the unmasked substrate or metal.

Lift-off

An example of an additive pattern transfer is the lift-off procedure. During lift-off, a chemical solvent dissolves the resist, and with it, the metal thin film on top of the resist is lifted off. This process leaves the remaining metal in the desired areas. The most crucial factor for an additive pattern transfer such as lift-off, is that there is a negligible amount of side-wall deposition, such that the stripper can reach the resist. Resist thickness should be matched with the desired metal thickness so that the resist is at least three times thicker than the deposited metal [30].

Metalization

To deposit the metal onto the substrate, the chosen technique depends on the metal, resist, and desired structure. If executing an additive pattern transfer such as lift-off, the resist structure must be preserved during the deposition process. The glass transition temperature of polymer resists define when the polymers start to soften [30], and so a deposition should always be done below this critical temperature. The following list displays common deposition techniques:

- **Epitaxy** - Layer by layer crystalline growth that matches substrate lattice structure.
- **Chemical Vapor Deposition (CVD)** - A chemical reaction in a reactor creates the desired compound and the molecules diffuse onto the substrate.
- **Physical Vapor Deposition (PVD)** - In high vacuum an electron beam heats a crucible filled with metal, and the vapor molecules travel in a straight mean free path to the substrate.
- **Sputtering** - A form of PVD where ions dislodge atoms from a metal target, that migrate onto the substrate.
- **Electroplating** - A substrate with a conductive surface is immersed in ion-solution and a voltage is applied creating a current which creates a reduction reaction and metal ions are deposited.

Comparing additive and subtractive pattern transfers shows that specific techniques lend themselves more to one or the other. Epitaxial growth is easier to achieve directly on a silicon substrate surface with metals holding a similar crystal structure. Resists are often poor conductors, so the electroplating method could be hard to achieve on resist-covered substrates.

In order to avoid side-wall deposition for lift-off, anisotropic deposition is favorable, entailing that the deposition is highly directional so that only a planar surface of the substrate is covered in metal. An illustration of this can be seen in fig. 2.4. CVD, sputtering, and electroplating typically depose metal in an isotropic manner. However, an electron beam PVD method will deposit the metal anisotropically.

(a) Isotropic metal deposition

(b) Anisotropic metal deposition

Figure 2.4: After isotropic metalization the resist walls are covered (a), but for anisotropic deposition the walls are exposed (b), which enables lift-off.

Chapter 3

Fabrication by Electrons

On the Limits of Light

In a lithography process for larger structures, a standard method of exposure is electromagnetic radiation. This method has the benefit of readily available radiation sources and the opportunity to run exposures in atmospheric pressure. However, as the size of critical structure dimensions becomes lower than that of the radiation wavelength, the wanted structures cannot be fabricated. The wavelength determines the smallest possible size of the structure. The second limitation of electromagnetic radiation is optical diffraction against the same size dimension features as the wavelength. Commonly known as the optical diffraction limit, this sets a hard cap to the resolution of both fabricating and imaging nanostructures. To overcome this limit, the phenomena of wave-particle duality of the electron are taken advantage of. Using electrons allows for both fabrication of smaller structures by electron beam lithography, and imaging by scanning electron microscope (SEM).

3.1 The Electron Source

In electron microscopy, the first electron sources initially utilized high power thermionic emission. A sharp tip filament, typically made from tungsten, is heated to a high temperature ($\sim$ 2700K) by driving a current through the filament. This heating thermally excites electrons by overcoming the filament work function [35]. This high temperature leads to a larger emission area from the thermal cathode, and the resulting electron current must be focused into a narrower beam by accelerating the electrons towards a strong lens using a potential difference between the cathode and lens (anode) [30]. A major disadvantage of thermal emission is this thermionic emission area size and the need to narrow the beam diameter. At a certain point the electron density in a cross-section of the beam will get too high, and the electrons will start to repulse due to

Coloumbic interactions [30]. These issues make high beam-resolution difficult, but electron beams still have a better resolution than optical beams.

Advances in SEM imaging led to the development of field emission electron sources, circumventing the need for beam narrowing altogether and giving the possibility for low voltage SEM applications [36]. In field emission, a high electric field ($> 10^8$ V/cm) excites the electrons from the point of a thin needle by application of a low voltage [30].

This method is not suitable for use in an EBL system, as the cold cathode can absorb contaminants from its surroundings, giving a source of error in the form of current noise and drift [30]. These errors would be unacceptable in lithography, as any unwarranted flicker could result in undesirable resist exposure. Therefore, a thermal field emitter or Schottky emitter is favored for use in EBL systems [36]. In a Schottky emitter, the filament is heated before applying the electric field, removing any surface impurities and providing a stable source for the electron gun. The most common filament is ZrO/W, where the zirconium lowers the tungsten work function.

The electron source typically sits at the top of the optical column, as seen in the schematic in fig. 3.1. After excitation, the electrons are focused through a series of lenses and apertures.

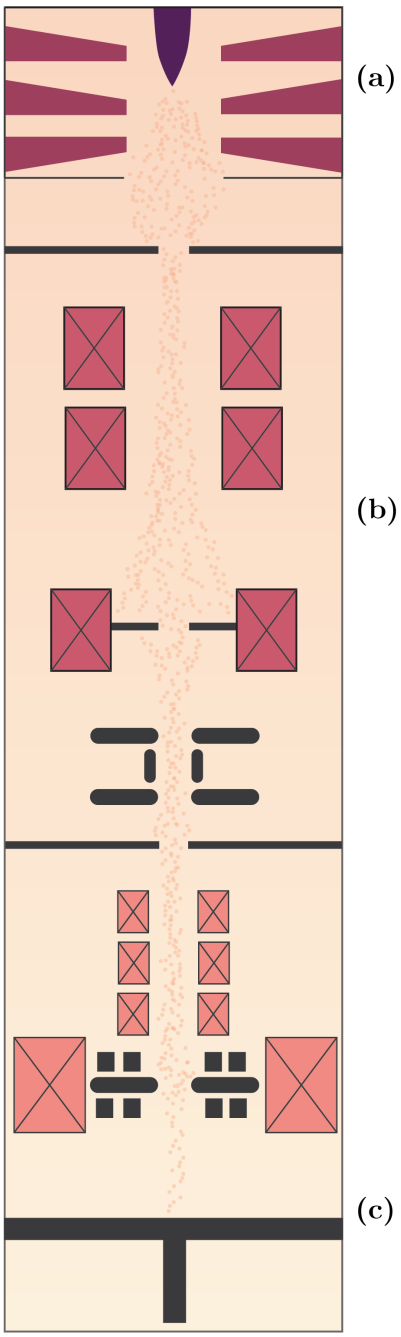

Figure 3.1: Schematic of the electron column in a typical SEM or EBL system. Shows the electron gun (a), lens and aperture systems (b), and the interferomteric stage (c).

3.2 Electron Optics

The wavelength of the electron (λ_e) is dependent on its momentum (p) by the de Broglie relation [37]

$$p = m_e \vec{v} = \frac{h}{\lambda_e} \tag{3.1}$$

where m_e is the electron effective mass, v is the electron velocity, and h is the Planck constant. This equation can be used to derive the

relation between λ_e and the acceleration voltage (V_0) applied inside the electron source. Conservation of energy yields the following formula [37]

$$eV_0 = \frac{p^2}{2m_e} = \frac{h^2}{2m_e\lambda_e^2} \tag{3.2}$$

$$\Rightarrow \lambda_e = \frac{h}{\sqrt{2m_e eV_0}} \tag{3.3}$$

where e is the electron charge. This strong correlation between the applied V_0 and electron energy means that this can be used as a tailoring parameter when specific requirements for different instruments need to be met. A lower V_0 will increase the electron wavelength and subsequently increase the spread of the beam. In addition, the electron energy will lower, and the penetration depth will be smaller. The opposite is true for increasing V_0, so systems using electron beams should consider the trade-offs between high or low acceleration voltage, and which beam characteristics are necessary.

3.2.1 Lenses and Apertures

Due to the strong scattering and absorption of electrons in a typical lens-media, such as glass, other methods must be used to focus the electron beam [38]. These lenses are either magnetic utilizing the Lorentz force [24]

$$\vec{F} = e\vec{v} \times \vec{B} \tag{3.4}$$

where $\vec{B}$ is the applied magnetic field, or electrostatic utilizing the electrostatic charge to move the beam.

Electrostatic and Magnetic Lenses

An electrostatic lens exploits the charged nature of an electron. When a charged particle enters an electric field, it will experience a force. This force can be used to change the direction of the particle. In practice, this is done by a circular conducting electrode, deflecting the electron beam into the center of the device due to the symmetrical nature of the applied field [38]. If the electron beam is subjected to a magnetic field instead of an electric field, the lens is magnetic. Typically electrostatic lenses are used to move the electron beam, and magnetic lenses are used for beam focusing.

The electron column is typically made up of one or two condenser lenses, an objective lens, and a couple of apertures [35]. Apertures are simply holes centered around the optical axis and allow for a form of directional filtering. For more information regarding electron lenses, see chapter 2 of [38].

3.2.2 Aberrations

Getting an electron through a lens is not as simple as letting rays of light through a glass window. Whereas light passing through the air into an optical lens undergoes discontinuous refraction, the refraction of an electron passing through an electromagnetic lens is dependent on a continuous function [30]. Aberrations in an optical system can be fixed by inserting more lenses; the solution in an electron-optics system is not so trivial. Aberrations arising throughout the demagnification process of electron columns cannot be fully fixed, but they can be minimized. The three main types of distortions are spherical and chromatic aberrations and astigmatism, which will be detailed in the following sections.

Spherical Aberration

Spherical aberrations occur due to larger angle deflection of electron rays further from the optical axis [37, 38]. This angle deflection means that the electrons further from the axis are focused closer to the lens than the paraxial rays. This focusing creates beam broadening in the image plane [37], and subsequently a lower resolution. Spherical aberrations can be minimized by using a strong lens with a small focal length and apertures to limit angular deviation of electrons from the optical axis [38].

Chromatic Aberration

Chromatic aberrations refer to the distortions due to wavelength fluctuations, which reduce the resolution as the focal length of the lens depends on it [37]. As the wavelength of an electron is tied to the electron energy, fluctuations from the source or during the path through the column will lead to distortions. Chromatic aberrations can be minimized by the same measures as for spherical aberrations, and by additionally using high acceleration voltages for the electrons [38].

Astigmatism

Astigmatism is an effect that occurs due to asymmetric magnetic fields in the lenses [37]. This difference in the magnetic field will lead to a difference in focusing power. In order to handle this, modern systems are fitted with a stigmator, a weak lens, that an operator may manually adjust. This lens minimizes the effects on the resolution by astigmatism.

3.3 Electron-Sample Interactions

When the electron beam has made it through the optical column, the electrons interact with the specimen mounted on the stage. The electrons that originate from the electron gun and first interact with the sample are called *primary electrons*, whereas the electrons that originate from the primary electron interactions with the substrate atoms are termed *secondary electrons* [39]. Both primary and secondary electrons scatter and may give energy to the specimen via interactions.

3.3.1 Interaction Volume

As the high-energy electrons interact with the sample and penetrate the specimen, the volume reached by the electron energy is termed the *interaction volume*. Figure 3.2 shows a cross-section of the specimen, and the volumes of the specific interactions. The volume varies with electron beam energy, and the broadening occurs mostly due to BSE.

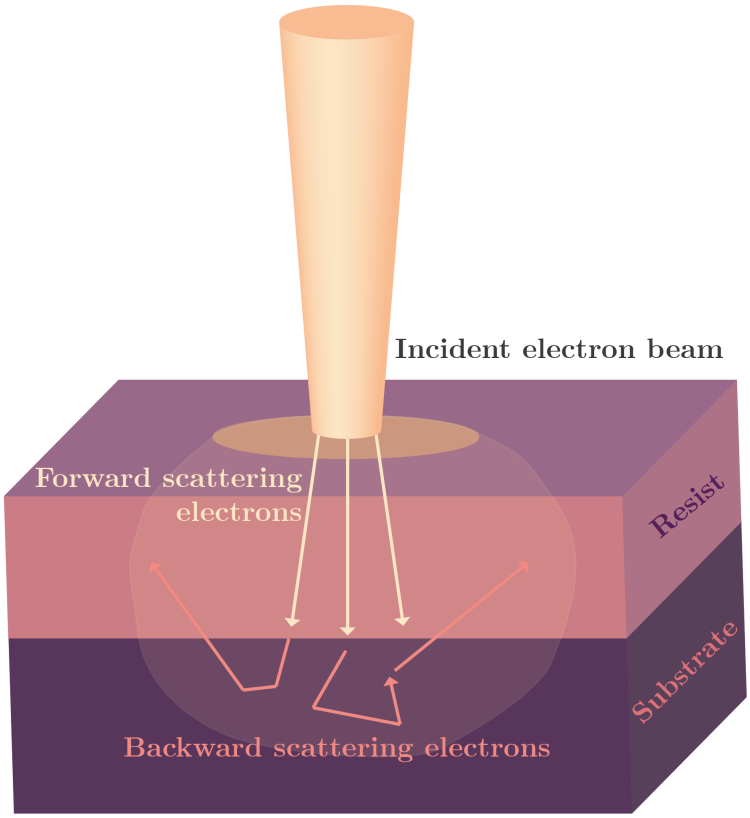

Figure 3.2: The interaction volume when an electron beam hits a resist coated substrate.

3.3.2 Emitted Signals

Secondary electrons arise from the inelastic scattering of primary electrons with specimen atoms. The primary electron loses energy to the atom, which excites an electron. This excitation transfers energy to the specimen and the created secondary electrons can resurface. Backscattered electrons are primary electrons that go through scattering due to elastic collisions with the specimen atoms. These electrons may also resurface. Auger electrons are created by the energy surplus in an atom after the excitation of a secondary electron. This excitation typically releases a low-energy electron from its outer shell. The Auger electron has an energy characteristic to its atomic element and can be used to characterize materials. As the electron energy is typically low, this method only works on the surface of the specimen.

During the creation of secondary electrons, electrons falling to lower shells may produce X-ray radiation, which can be used for material characterization. Some of the electrons pass through the specimen, particularly for ultra thin samples. These are transmitted electrons and can be used to characterize the density and thickness of samples.

3.4 EBL

Using electrons to expose resist is termed electron beam lithography (EBL). An EBL system is quite similar to that of a scanning electron microscope (SEM) and can typically be added to a traditional SEM with a few relatively cheap alterations, while a dedicated EBL system can be rather costly. The EBL system typically comprises of an electron optical column to produce the electron beam, a high precision stage to move the sample, a vacuum system, as well as supportive electronics, control computers, and software [40]. The electron travels through the optical column and hits the specimen at points specified by the digital mask. The desired pattern is achieved by beam deflection and precise stage movements.

3.4.1 Proximity Error Correction

Due to the interaction volume of electrons with the sample specimen, the resist will expose beyond the beam location. Proximity error occurs when secondary and backscattered electrons expose the resist in proximity to the beam shot. This error must be fixed in what is named Proximity Error Correction (PEC). In essence, PEC uses a simulated electron interaction volume based on exposure and resist parameters to determine how much the exposure dose should be adjusted to account for the extra exposure. Typically this involves lowering the dose for the center of large structures or tightly packed patterns while increasing the exposure dose at the perimeters.

3.4.2 Mask Design

The design of the mask should follow from considerations regarding the entire fabrication process. Depending on the resist, functional material, metal deposition process, and pattern transfer, the desired structures may or may not be possible. This knowledge must be taken into account, and often the fabrication process is iterative and contains many rounds of mask design to perfect the result for the specific process. The digital mask for use in EBL is made in CAD-software, often specific to the EBL system. This software can often read in files to convert them to file formats that are readable by the software that drives the EBL system. This file-type contains the geometric properties of the mask and the exposure dosage, PEC-profiles, write field placement, with the possibility of adding many more specific requests. The most basic digital mask creation routine for EBL includes pattern fracturing, PEC, and placement of write fields.

Fracturing

In the mask software, the desired structures are divided into smaller non-overlapping simple shapes, such as rectangles or trapezoids, by fracturing. As the size of the features decreases, the number of rectangles or trapezoids increases to accommodate for feature accuracy. Each rectangle or trapezoid is composed of exposure shots. Shots are single exposure units [41], and the shot size depends on the beam diameter. For high-resolution patterning, the shot pitch and beam diameter must overlap to a certain degree.

Write Fields and Alignment

The system divides larger patterns into *write field*. A write field is an area where the electron beam is moved by beam deflection to write the desired shots before the stage moves to the next field. This method increases the writing speed, as the electron beam movement is one of the more time-consuming processes of doing EBL. The system may support different sizes of write fields. A larger write field will decrease writing time, but at the possible cost of beam aberrations at the field edges due to large-angle deflection. For patterns with small critical feature sizes, a smaller write field is preferred to reduce this effect. Smaller write fields do require more field stitching. As seen in fig. 3.3, the shapes distributed over two fields must be stitched correctly to achieve the correct final shape, also entailing that the write fields are correctly aligned.
Stitching and alignment refer to the process of making the exposed patterns continuous over the write field borders. Choosing a smaller write field will also entail doing more field stitching as the pattern will require more write fields. A trade-off must be made for which size is most suitable for the desired pattern. The writing order of the fields may also be specified, as this impacts field stitching success. When doing multiple exposures, the write fields must

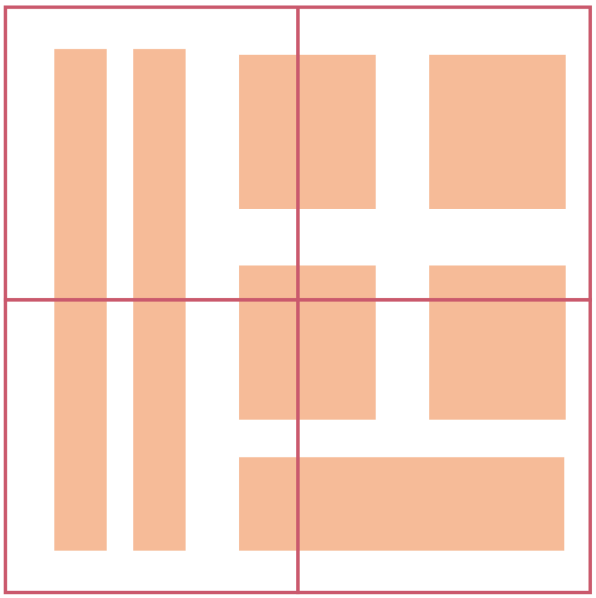

Figure 3.3: The division of pattern into write fields.

also align with the underlying exposures. For small margins of error, this may be difficult, and so the precision and resolution of the EBL system must be kept in mind while creating the mask.

3.4.3 Optimization

The main advantage of using EBL is the superior resolution, allowing for much smaller structures than the average photolithography system. However, the direct-writing method means that the EBL exposes at a much slower rate than the typical photolithography system. This slow writing time makes the system have a very low throughput, a clear disadvantage for mass production or production of large patterned areas. Therefore, measures are taken to lower the writing time without sacrificing resolution power.

Resolution

The acceleration voltage is dictated by the system, as stabilization of the voltage takes a long time. Changeable parameters are the beam current and aperture which determine the beam size, and therefore also dictates the resolution. Higher beam currents give smaller beam diameters. The density of dots per write field also impacts the resolution. A write field of 100 µm with 200000 dots will have higher resolving power than a 500 µm write field with the same number of dots, as the fractures will be divided into smaller shots. Before running

the exposure, the focus of the beam is done manually by focusing on a reference sample. The resolution should be good at around the size of the critical dimensions of the pattern, as an unfocused beam will lead to blurring of pattern and possibly poor contrast in the resist. A modern EBL system is able to deliver a resolution in the subnanometer regime.

Writing Time

The writing time depends on how the beam scans the surface, where a so-called raster scan sweeps the entire write field, and vector scan only sweeps over the desired pattern. For larger areas, raster scanning may be faster than vector scanning, but a vector scan is preferable for smaller structures and patterns, as the beam dose not have to move over surfaces where there is no pattern to be exposed. The hard cap on the writing speed is the system frequency. This is set by [40]

$$f = \frac{I}{DA} \tag{3.5}$$

where I is the beam current D is the exposure dose needed to expose the resist, and A is the exposed area. A 100 MHz system will be able to deliver current for 0.01 µs per dot as the shortest possible exposure. A typical dot size is 2 - 10 nm, and a typical beam current is in the range 0.5 - 20 nA. The dose time per dot is dependent on desired exposure dose, pitch and beam current. All parameters must be optimized for the desired end structure and the overall process. There are several suggestions as to how future EBL systems may improve the writing time. These include multiple-beam exposures [36] and pixel parallelism [40].

3.5 SEM

A SEM system often comprises an electron column, a movable sample stage, detectors, vacuum systems, and the accompanying electronics and software to use the system. Unlike with the EBL system, the goal is not to fabricate anything, and so the operating voltage and currents are more flexible to create the desired resolution. High-velocity electrons could inflict damage on a specimen, and so the system should be used with caution. The sample must be conductive. If not, a charge build-up will occur on the sample, creating image distortion by discharging when the build-up is too high. Typically, non-conductive samples are coated before being imaged. The main advantages of imaging with electrons are the high resolution, magnification range, and the multitude of generated signals [39]. This enables the imaging of sub-micron features such as transistor gate features and nanoscopic particles.

3.5.1 Detectors and Imaging Modes

As discussed in section 3.3.2, electrons hitting a surface generate many different signals that can be used to characterize many aspects of a sample specimen. In order to analyze these signals, powerful detectors for each signal type must be outfitted into the characterizing system. For a SEM, these are most commonly detectors for secondary electrons (SE), backscattered electrons (BSE), cathodoluminescence, and X-rays [39].

Electron Detection

This section is based on the chapter *Scanning Electron Microscopy* by R. Reichelt in *Science of Microscopy* [35]. There are three main methods to detect electrons after electron specimen interaction. The first method is to convert the electrons to a photon by using a special scintillation material and further converting to an electric signal by a photomultiplier. This method can measure both SE and BSE, and is typically called an Everhart-Thornley detector. The second way of detection is to use recombination of electron-hole pairs in semiconductors to incite current when impinged with electrons. This method is used for BSE. A third principle is to convert the electrons to more secondary electrons in a multiplier tube to amplify the signal so that the measurement is proportional to the signal electrons.

Imaging Modes

This section is based on *Scanning Electron Microscopy (SEM) and Transmission Electron Microscopy (TEM) for Materials Characterization* by B. Inkson in *Materials Characterization Using Nondestructive Evaluation (NDE) Methods* [39]. The SEM is a powerful tool in order to image submicron structures and materials with high resolutions. Shape, chemistry, and crystallography can all be characterized in a SEM system. The morphology or topography of a sample specimen is examined with SE that escapes the specimen surface at various angles. The specimen structures form different angles with the incident beam, so a visible contrast is formed in the resulting micrographs. Typically edges and ridges of a structure have increased SE emission and appear brighter, giving the micrographs their 3D-effect. The chemical composition of a material can be analyzed by using BSE or X-rays. These non-destructive methods allow the investigation of the composition of materials, films, and fabricated structures.

3.5.2 The Ideal Image

When evaluating SEM micrographs, it is vital to bear in mind how the micrographs are obtained and that the result is not the same as a photograph. During the imaging process, many parameters could interfere with the analysis,

such as astigmatism and digital image settings, which influence the final micrograph. This result-warping is particularly true when doing precise size analysis on nanoscale structures. More information on the properties of the ideal SEM micrograph is found in chapter 2.1 of [38].

3.6 VSM

While the SEM system can analyze the morphology and chemical characteristics, it does not give any information on a material's magnetic properties. A way of measuring the magnetic response of a magnetic material is a Vibrating Sample Magnetometer (VSM). First suggested by S. Foner in 1959, the VSM uses coils to produce and detect the change in a magnetic field H of a vibrating sample [42]. The sample is vibrated perpendicularly to the applied field, and even small changes (10^{-5}-10^{-6} emu) to the field can be detected [43]. A schematic of the system can be seen in fig. 3.4, where the sample is placed in a sample holder and placed between two coils.

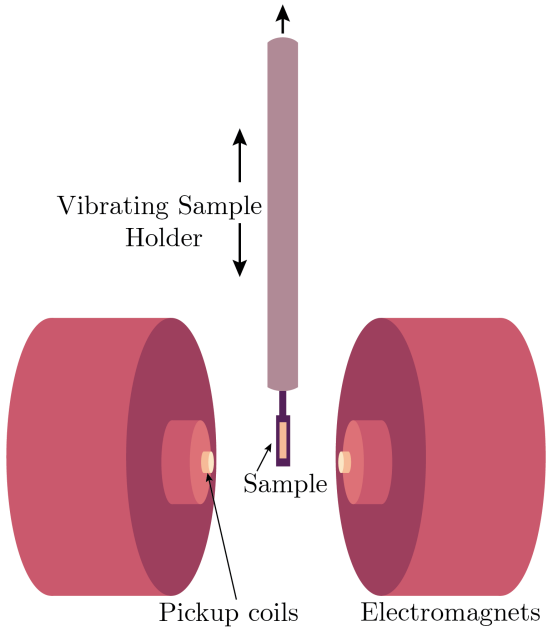

Figure 3.4: Schematic of a simple VSM setup for hysteresis measurements.

When the sample is vibrated, there is an induced current in the coils by the magnetic flux, as in Faraday's law of induction, eq. (1.5). As the magnetic flux is proportional to the magnetic moment in the sample, this current will give an accurate signal. Figure 3.4 shows a simple schematic setup of a typical VSM. The material and shape of the sample holder is important, as it will give a diamagnetic contribution. Most VSM systems offer sample rotation options for anisotropy analysis and temperature control for studying critical magnetic temperatures.

The benefit of using VSM as opposed to other magnetic characterization techniques such as XPEEM or MFM is that the magnetic moment of the entire sample may be measured. The disadvantage is that it includes signals from the sample holder and other possible contaminants.

Chapter 4

Experimental Methods

4.1 The Cleanroom Environment

The particle size of regular dust ranges from 1 - 100 µm [44], whereas the intended structures are of a size 10 by 100 nm. This size difference entails that any particle contamination in a conventional environment could be detrimental to fabrication. Figure 4.1 shows the scale of a 2 µm dust particle compared to a 15 nm thick metal film. Not only could this type of contamination interfere with the fabrication process, but it can also damage the fabricated structures. Therefore, the fabrication process was completed in a *cleanroom*, a filtered environment in which the number of particles in the room is lowered from 10^6 to under 10^4 particles per ft^3 [45]. At NTNU NanoLab, this is done by high-efficiency particulate air (HEPA) filters that remove all particles above 0.3 µm, a vertical laminar airflow, and a slight overpressure [45].

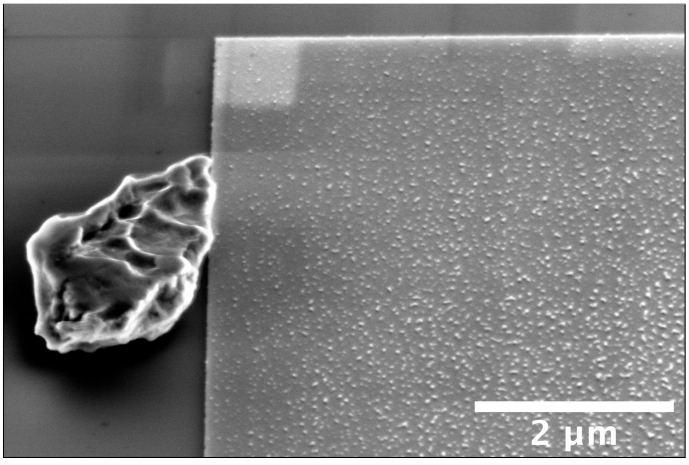

Figure 4.1: Micrograph of a dust particle on top of a metallized exposed area, most likely introduced to the sample by the author.

4.2 Resist and Spin-coating

The first step of the process was to evenly distribute the chosen resist onto a wafer. In this project, a 4 inch [100] silicon wafer was used, hereby referred to as *the wafer*.

CSAR 62

The resist series AR-P 6200 (CSAR 62) are high-contrast, positive resists for e-beam exposure [46]. The high-contrast, in addition to the high sensitivity, make the obtainable resolution about 6 nm according to the manufacturer specifications, which should be sufficient in this work [47]. In order to achieve the desired film thickness, the resist was diluted 2:1 parts anisole solvent by weight. When working with resists, it is essential not to introduce any impurity into the storage container, as this may cause agglomeration of resist and reduce the predictability of exposure properties. Therefore, great care was taken not to introduce contamination while pipetting or otherwise handling the resist container

Wafer Cleaning

Before applying any resist, the wafer was cleaned by the following process. First, the wafer was soaked in a bath of acetone for 5 minutes, taking care to rinse thoroughly with IPA the moment the wafer was removed from the bath to prevent the formation of an acetone film. This rinse was followed by a drying procedure consisting of drying by nitrogen gun and a subsequent dehydration bake on a 100 °C hotplate for 5 minutes. Finally, the wafer was cleaned in a Diener Plasma Cleaner model Femto, for 1 minute at 50% oxygen and 50% generator power.

Spin-coating

In order to coat the wafer with resist, a spin-coating method was used. The cleaned wafer was carefully placed on a vacuum chuck that accommodated the size of the wafer, and was placed in a spin coater. The diluted resist was pipetted onto the center of the wafer, and the spinning process initiated. As the process was repeated for several wafers, several spin speeds were used. In general, the parameters were an acceleration of 1000 rpm/s, a spin speed of 3000 - 4000 rpm, and a total spin time of 60 seconds. After coating, the wafer was baked on a 150 °C hotplate for 2 minutes to promote further evaporation of resist solvents.

Scribing

As the desired area of the pattern is rather small, it is efficient to scribe the wafer into smaller *chips* so that more samples can be made from each wafer. The

crystallographic directions are used to scribe the wafer into square chips of 10 - 20 mm sizes.

4.3 Exposure and Development

4.3.1 Digital Masks

The digital masks were created in *Jupyter Notebook* using the Python package *PHIDL* [48] and visually verified in *Layout Editor* [49]. A generic Python code for this purpose can be read in appendix A.1. For different tests and samples, the mask varied greatly, but in essence, the two exposed patterns are 100 nm circular disks in the hexagonal and square lattices. Figure 4.2 shows a small area of the desired structures. The exposed areas contain more disks in a repeating pattern to fill the desired area. Areas used in this project were 10 by 10 µm, 20 by 20 µm, 50 by 50 µm, and 95 by 95 µm.

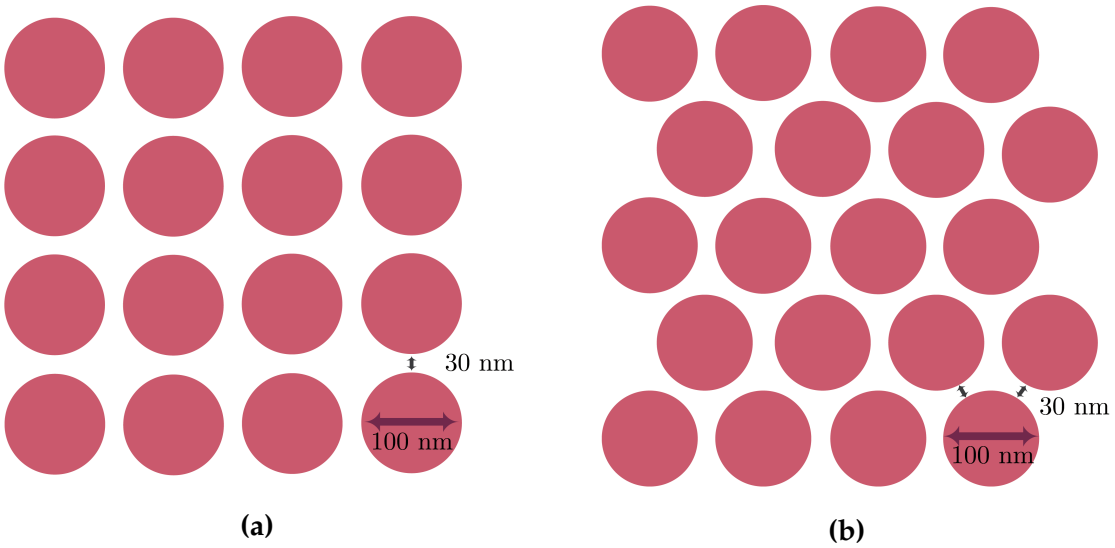

Figure 4.2: Illustration of the desired structure parameters for (a) square lattice and (b) hexagonal lattice.

The GDS-files then require conversion to a file that is readable by the EBL-system. This was done in the GenISys *Beamer* program [50]. First, the mask-file was imported into the software, and the *HEAL* function was used to remove any potential pattern overlap. Then, the *PEC* function was used to apply any necessary corrections for proximity errors. During PEC, the program adjusts for the EBL system parameters, the resist thickness and material parameters, and substrate material. The PEC profile that was used was for 100 nm CSAR 62 on a Si substrate, and a screenshot of the simulated energy distribution can be seen in fig. 4.3. The green areas of the figure denote the long-range exposure due to

scattered electrons. Subsequently, the *EXPORT* function was used to export the file to the desired format. In this project, the function was used to convert the file to a .CON type. During this step, the correct parameters for the exposure as outlined in section 4.3.2 were used as input while converting and saving the file.

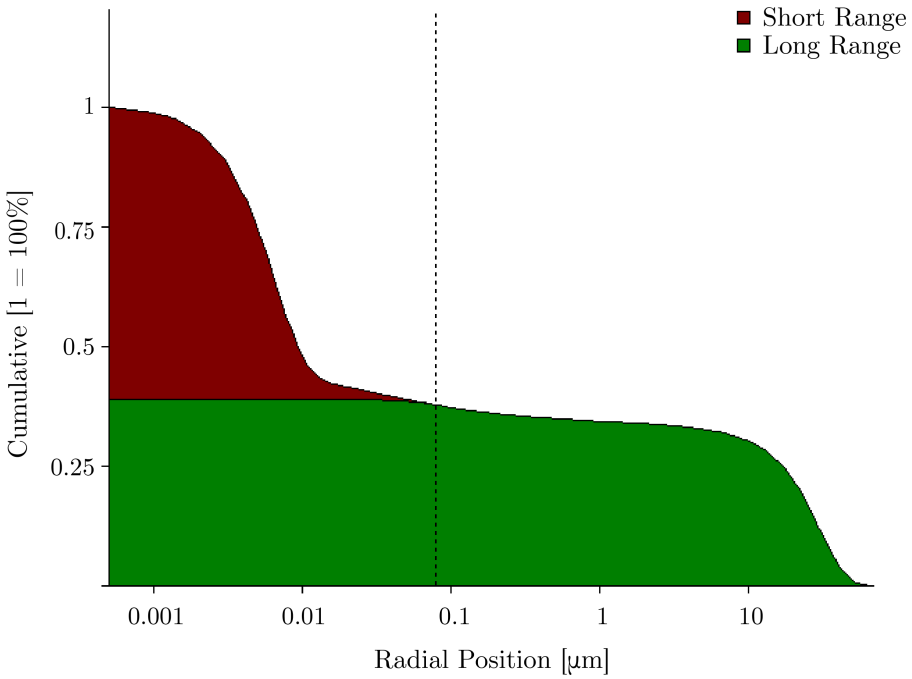

Figure 4.3: PEC profile used for PEC of digital masks

4.3.2 Exposure

The EBL system used in this project was the Elionix ELS-G100 [51]. The .CON file extension is readable by the *WecaS* software that controls the exposure sequence on the EBL system.

System Parameters

The Elionix is a 100 kV system with a patterning speed of 100 MHz. In order to expose the desired pattern, some exposure parameters must be set. The size of the write field was set to 100 µm in order to avoid any distortions at the edge of the write field, which may occur for larger beam deflections in larger write fields. In choosing the beam current, several factors must be evaluated.

The beam current determines the beam diameter and establishes the highest resolution obtainable during exposure. However, the current must also be set to an appropriate amount, and each dot must be exposed for the correct time within the system writing speed, as the total exposure dose is a function of current and exposing time. The appropriate beam current for this project was 500 pA, with the objective lens aperture set to 120 µm. This yields a beam diameter of 2.1 nm, so with a write field size of 100 µm chosen to avoid edge distortions, and the number of dots per write field set to 50000, the resolution of the exposure should be around 2 nm. The exposure doses used in this work were in the range of 140 - 260 $\mu C/cm^2$.

Exposure Setup

The coated substrate chip was loaded into the machine following the system manual. Then, the beam current was measured and adjusted if necessary to achieve 500 pA. Afterward, the beam focus was adjusted in the SEM mode of the system. For the desired resolution, a focused image at a magnification of 100000 was satisfactory. The exposure writing time varied for the desired pattern density and total exposure area. After exposure, the chip was unloaded from the instrument.

4.3.3 Development

For the resist to keep the exposed pattern, the chip must be developed to set the resist. The development is done with the AR-600-546 developer [47]. The chip was lowered into a beaker of 10 mL, or just enough to cover the sample, of AR 600-546 and developed for exactly 60 s. Immediately after lifting out of the developer bath, the chip was thoroughly rinsed with IPA to stop the development process, followed by a 60 s IPA bath. The chip was then dried with a nitrogen gun and was ready for metalization. It is essential that the sample is not left in the developer for too long and that the sample is appropriately rinsed to avoid overdevelopment. Overdevelopment can lead to the developer eating away at the exposed pattern and loss of detail. If kept undeveloped over a longer period of time, the photoactive compound of the resist may begin to break down, and the pattern may also lose its detail.

4.4 Metalization and Lift-off

4.4.1 E-beam Evaporator

The instruments used for metalization in this project were the AJA International Custom ATC-2200V and the Pfeiffer Vacuum Classic 500. The operation of these

two systems is relatively similar. For the Pfeiffer, the pressure inside the chamber was lowered so that the sample could be loaded into the system. The samples were attached to a 10 cm diameter stage with tape, meaning that several samples may be metalized at once. After sample mounting, the pressure was built back up to around 10^{-5} mbar to ensure a straight deposition path. Subsequently, the e-beam was turned on at a constant voltage of 8 kV and an adjustable current. The current was gradually increased until the target was melted, and the desired deposition rate was acquired. Then the shutter covering the sample was removed, the sample stage was set to rotate to even the deposition, and the quartz crystal monitor recorded the thickness of the deposited metal layer. When the layer thickness was at the chosen level, the shutter was moved to cover the sample. Then the electron beam was turned off, and the system pressure lowered to unload the sample. Metals deposited during this project were Al, Au, Ti, and Permalloy.

4.4.2 Permalloy

A common material for supermagnetic metamaterial fabrication is Permalloy (Py) [18, 20, 52, 53]. Py is an alloy of $Ni_{80}Fe_{20}$ and was chosen due to its high magnetic permeability, low coercivity, and low magnetostriction [2]. These parameters are important for the study of supermagnetism, as the desired magnetic ordering should occur due to dipole interactions and not other magnetic contributions to the system. Permalloy turns out to be a somewhat finicky metal to work with when using an evaporation method. The main issues lies in the pellet melting to form the puddle. The pellets are extremely volatile during preliminary heating and are prone to exploding, covering the inside of the chamber with stains of magnetic metal. Great care must be taken during this process, and it is recommended to melt the pellets before loading the sample into the PVD system. This method ensures that the sample is not overheated and that the resist does not heat over the glass temperature. To avoid oxidation at the surface of the Permalloy layer, an Al or Au capping layer of about $2-3$ nm was deposed after the primary metalization process.

4.4.3 Lift-off

The lift-off was performed by submerging the sample into the AR 600-71 remover [54] with the beaker in an ultrasonic bath. Using the ultrasonic bath diminishes the probability of flushing out the resist, as CSAR 62 is a resist that strips quite rapidly. The chip was submerged for 15 minutes in the ultrasonic bath before aggressively rinsing with acetone to remove any stray metal pieced physically. Next, the chip was submerged in an acetone bath for 5 minutes and finally placed in an IPA bath for 5 minutes before it was dried with a nitrogen gun. This step marks the end of the fabrication process.

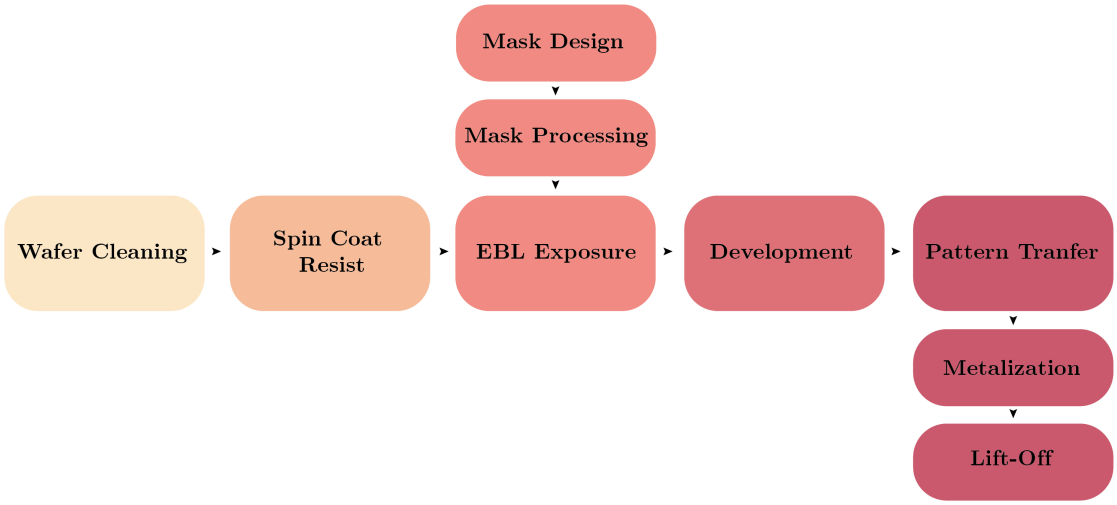

Figure 4.4: Fabrication process flow

4.5 Sample Analysis

Following the fabrication, the chip must be visually inspected for any unwanted impurities before it can be measured in a VSM. The thickness of the spun-on resist was measured in a Filmetrics F20 Reflectometer and the visual inspection of the fabricated samples were done in an FEI SEM APREO.

VSM

The Princeton Vibrating Sample Magnetometer was used to perform magnetic measurements on the samples. First, the sample was mounted with carbon tape to the sample holder, a type of dipstick for this system. The dipstick was then mounted into the instrument, much like the schematic in fig. 3.4. To center the sample to the instrument saddle point, the magnetic signal was maximized while applying a 100 mT field and vibrating the sample then moving the dipstick with micrometer screws to the point where the signal was strongest. The sample was then moved to the coil normals to minimize the signal, signifying the center point between the two coils. After mounting the sample, the measurements were carried out by inputting the necessary parameters for the tests, including field variation, number of measurements per applied field, and length of measurements. Thin film samples were rotated manually by de-mounting the sample, rotating it, and redoing the steps to locate the saddle point, whereas the large patterned sample was mounted horizontally to the system and rotated by a motor attached to the dipstick. This sample was rotated both from 0° to 90° with an increment of 15°, and from 0° to 180° with an increment of 5°. All measurements were carried out at room temperature.

Part II

Results, Discussion and Conclusion

Chapter 5

Results & Discussion

For simplicity and making the project progression easier to follow, the results and discussion are presented jointly. In total, 17 separate samples were fabricated before the large-patterned sample was finalized. Fabricated samples will be referred to in the format *NAME (thickness of metal 1 in nm + thickness of metal 2 in nm)*, for example, SEP20-1 (15Py+2Al) has a 15 nm thick layer of Permalloy and a 2 nm thick capping layer of Al. More information regarding specific samples is provided in table 5.2.

5.1 Resist Investigations

5.1.1 Residual Resist

Following the work of the project thesis written in the spring of 2020, the working theory was that the longer a resist has aged, the higher the risk of precipitation of the PAC [55, 56]. Dilution of resist with solvent is also known to increase the risk of particle agglomeration [57]. The effects of this are seen in fig. 5.1, which shows an exposed area where the underlying particles lead to a textured and uneven metal surface.

5.1.2 Resist Aging

The agglomerated particles in the resist could lead to residual resist particles on the substrate, which will interfere with the metalized pattern during the lift-off process by removing metal from exposed areas. So, samples with different resist dilutions and dilution dates were prepared. Samples SEP20-1 (15Py+2Al) and SEP20-2 (15Py+2Al) were both exposed and metalized simultaneously to minimize error contributions from other steps in the process. Due to different dilutions, the resist used on SEP20-1 had a higher viscosity resulting in a higher resist thickness after spin coating. The resist on the SEP20-1 sample was diluted to 8.5 : 6 (CSAR:Anisole per wt) in December 2019, and the SEP20-2 resist was

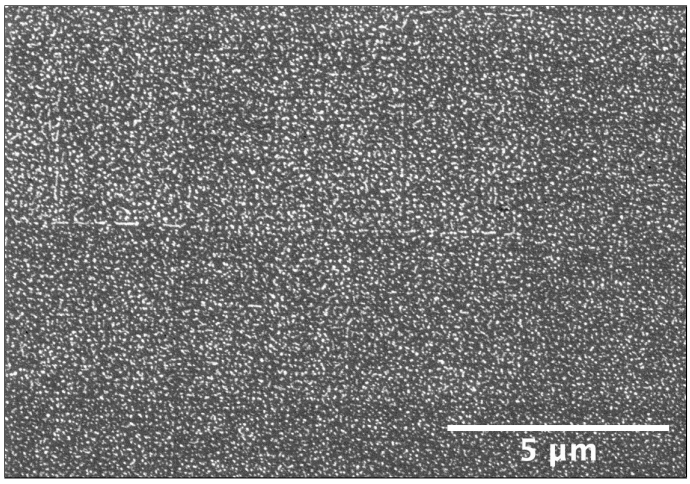

Figure 5.1: Micrograph showing textured and rough surface of a large exposed area. This area should be completely smooth, and the PEC borders should not be visible.

diluted 1.2 : 2.5 in September 2020. The thickness of the resists were 164 nm and 88 nm respectively. Due to the different resist thicknesses, different PEC profiles had to be used during mask processing.

Micrographs of the samples are seen in fig. 5.2. Both samples displayed signs of incomplete lift-off, though it is only visible in the micrograph of SEP20-1. The micrographs show that the SEP20-1 (fig. 5.2a) has more defined circular disks, compared to the more jagged edges of the disks in SEP20-2 (fig. 5.2b). The micrograph of SEP20-2 is taken at an area exposed to a higher exposure dose than that of the SEP20-1. However, the disks in fig. 5.2b still bear signs of being either underexposed or overdeveloped compared to that of fig. 5.2a, due to the uneven disk edges. This error might be a consequence of the different resist thickness, which will interfere with the resist contrast, as discussed in

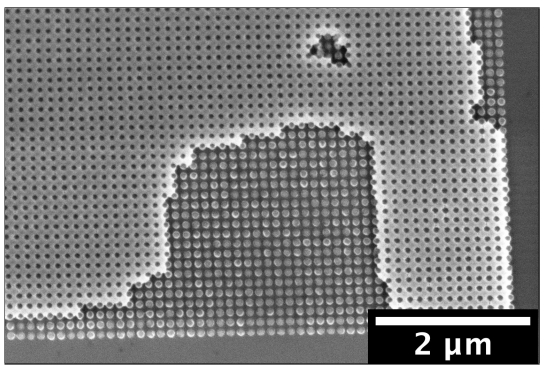

(a) SEP20-1, Dose = 200 µC/cm²

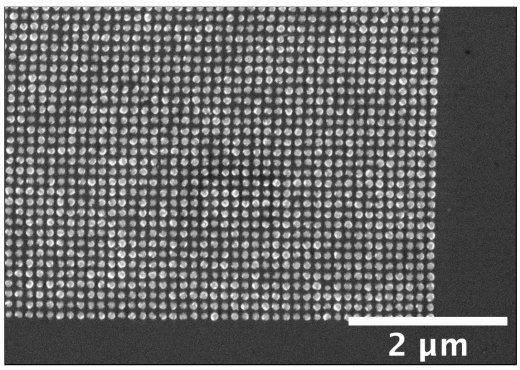

(b) SEP20-2, Dose = 220 µC/cm²

Figure 5.2: Micrograph of patterned structures to compare resist qualities. The layer covering the disks in (a) is metal that has not been removed during lift-off.

section 2.1.2. A thicker resist might also mean that the lift-off process more cleanly removes the top layer of metal.

One theory is that when parts of the PAC in a resist have precipitated, the PAC ratio in the resist that is pipetted out of the container is lower. Less PAC means that more exposure, or a higher exposure dose, is needed to clear the resist. This theory could explain the underexposure of sample SEP20-2. These results go against the working hypothesis that aging of a resist accelerates the agglomeration process, as the resist used for SEP20-1 was diluted ten months before the resist for SEP20-2. However, it does suggest that resists with higher dilution ratios may display higher PAC agglomeration levels, regardless of dilution date.

5.1.3 Agglomeration by Phase-Transition

It is possible that residual resist particles seen in fig. 5.1 are not PAC particles that have precipitated during storage. Some suggest that this residue can occur by polymer phase separation during the post-development process [31]. A typical process includes thoroughly rinsing the substrate with a development stopper or solvent to abruptly stop the development process. Investigations by Yasin and Hasko show that it is possible to reduce PMMA resist residue due to phase separation by rinsing with something other than IPA [58, 59]. When the developed sample is rinsed with IPA, some of the developer may be diluted rather than rinsed away. In the affected areas, the dissolved polymer may begin to re-link. This recombination increases the viscosity due to entanglement and makes it challenging to flush the polymers away from the substrate, leading to resist redeposition.

As CSAR62 is rather similar to PMMA, a similar test was conducted on sample OCT20-2 (10Py+2Au), divided into sub-samples A and B. Sample OCT20-2A has been developed using the regular IPA rinse-and-soak process, whereas sample OCT20-2B was not rinsed at all, only dried aggressively with a nitrogen gun after development. Both samples were resist-coated, exposed, and metalized simultaneously. Figure 5.3 shows the exposed areas of the sample, and both fig. 5.3a and fig. 5.3b look fairly similar to each other, and previous investigations.

The micrographs from fig. 5.3 were analyzed and show that particles from OCT20-2A have an average size of $0.0045\,\mu m^2$ and a particle density of around 22.6%, whereas particles in OCT20-2B, which was not rinsed in IPA had an average particle size of $0.0049\,\mu m^2$ and a particle density of 25.4%. Particle outlines from the analysis can be seen in appendix B. As these results are very similar, it shows that there is not enough evidence to conclude that rinsing with IPA after the development lowers the number or size of agglomerated resist particles for this fabrication process. It is deemed more likely that the residual resist particles are in fact due to polymer phase separation than pre-processing precipitates due

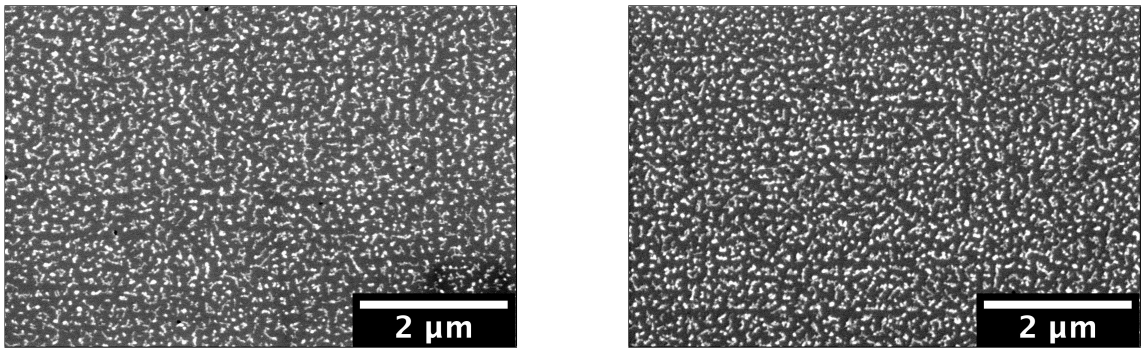

(a) OCT20-2A, IPA **(b)** OCT20-2B, No IPA

Figure 5.3: Micrographs of IPA testing for reducing agglomerate particles.

to the particle size. This conclusion does not mean that pre-processing precipitates may not effect the final result, as discussed in section 5.1.2.

The danger of not rinsing the substrate after development is the possibility of residual developer. If combined with a delayed pattern transfer process, this may have detrimental effects on the resulting structures. The residual developer may, over time, keep developing the resist, and so the structures will become overdeveloped. More information is needed before further pursuing this fabrication method, as the possibility of overdevelopment has not been investigated enough to conclude that it is worth the risk.

5.1.4 Proximity Error Correction

There seems to be a thin residual layer of resist covering all features in addition to the redeposited polymer particles. This is known as *scumming* [29]. An unexpected result of the scumming is the visibility of the effects of PEC (section 3.4.1), as seen in fig. 5.4. The difference in height of the plateaus are due to the difference in exposure dose awarded by the PEC. Micrographs during the previous project showed that resist particle sizes also changed according to the exposure coefficient due to PEC [55].

5.1.5 Resist Residue Removal

Regardless of their origin, the issues regarding redeposited resist polymers could be solved using a descumming process after the development step. Descumming removes any unwanted residual resist on the substrate while leaving the desired structures. The process is typically done by a short oxygen plasma clean [30]. Care must be taken that the descumming does not affect the patterned structure of the resist, the temperature must not be higher than the glass transition temperature of the resist, and the process must not be so long as to start degenerating the cross-linked resist. To establish a descumming procedure befitting

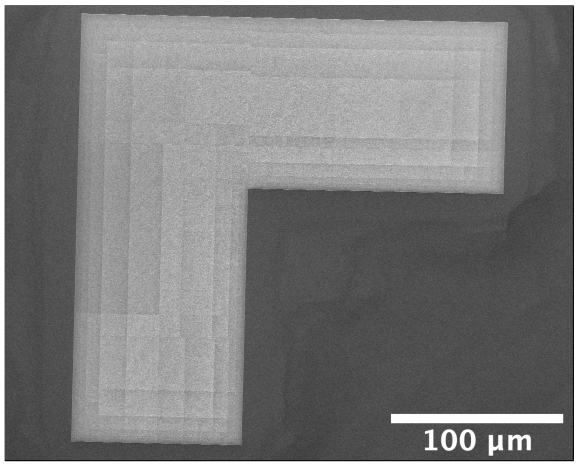

Figure 5.4: Micrograph of visible PEC fields on a pattern marker

the process parameters, a descum-and-inspect process should be repeated for different plasma clean parameters and cleaning lengths. The inspection could either be done by coating with metal and inspecting in a SEM, or by atomic force microscopy.

5.1.6 Post-exposure Breakdown

It is not only resist-aging while in storage that can deteriorate the integrity of the resist. If the resist is allowed to age after the exposure process, the PAC may begin to deteriorate. This leads to poor-contrast structures as seen in sample NOV20-1 (2Ti+15Au) in fig. 5.5b compared to the structures in fig. 5.5a. The time between exposure and development should be minimized in order to avoid this effect. This effect was only visible for the lowest exposure dose (180 µC/cm²).

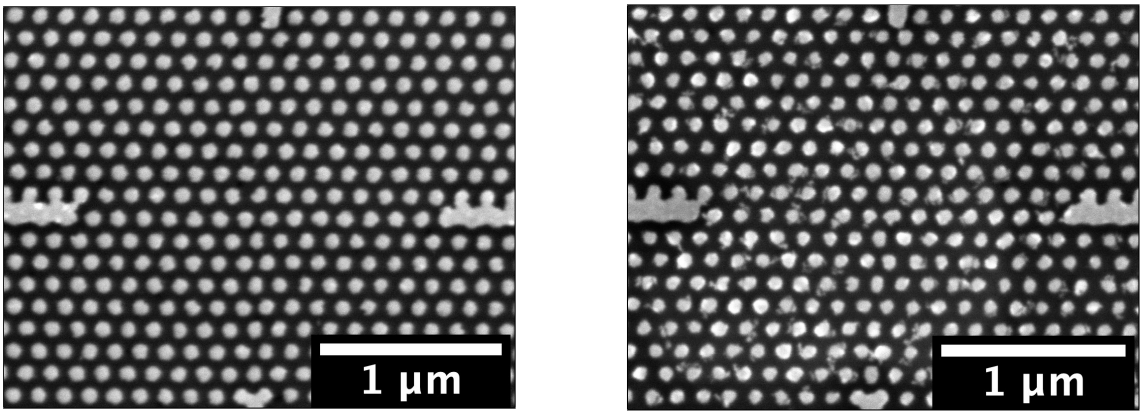

(a) NOV20-2 **(b)** NOV20-1

Figure 5.5: Micrographs displaying post-exposure breakdown of PAC visible as uneven disks and resist residue in (b).

5.2 EBL Parameters

5.2.1 Exposure Dose

The comparison of the exposure doses is made on the same pattern to maintain consistency, exposed and processed on a single wafer. The hexagonal pattern on the sample DEC20-1A (20Py+2.5Al) was examined for three different exposure doses (200 - 240 µC/cm²), which is around the dose used for previous projects [19, 55].

The analysis locations contained an adequately high number of disks, and the micrograph and corresponding outlines used for analysis for the first dose are seen in the figure fig. 5.6. The micrographs and outlines for the other doses can be viewed in the appendix B, whereas the code running the analysis is in appendix A.2. The area was chosen as a measure of size because it offered the most feasible solution for processing many disks simultaneously. Other parameters examined include the minimum and maximum diameters and the angle these formed. This examination allows for analysis of the ellipticity of the disks as well. The ideal disk area for a disk of radius 50 nm is 0.00785 µm^2, which comparing to table 5.1 corresponds best with an exposure dose of 240 µC/cm².

Table 5.1: Analyzed average disk areas of sample DEC20-1A

Dose [µC/cm²]	**Avg. size** [µm²]
200	0.00694
220	0.00746
240	0.00783

The error-margin for these calculations is not negligible. The SEM micrographs are not necessarily an accurate depiction of the topological landscape on the sample. What appears to be a residual metal on top of the disk may warp the

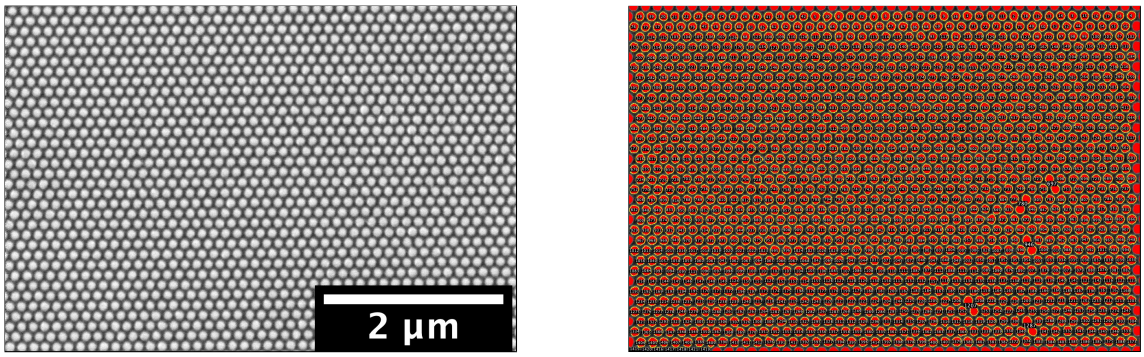

(a) **(b)**

Figure 5.6: (a) Micrograph, and (b) threshold outlines for dose 200 µC/cm² used for size analysis.

image to make the disks appear larger than they indeed are. Specifications during the imaging and analysis process such as resolution, focus, brightness and contrast, and image threshold may also lead to distortions in the micrograph, making the measurements inaccurate.

5.2.2 Stitching

The electron gun was scheduled to be re-calibrated in a maintenance done during the experimental work. Two samples were created to compare the possibility of stitching errors before and after recalibration of the sensors. Sample NOV20-1 (2Ti+15Au) was exposed before the gun change, and sample NOV20-2 (2Ti+15Au) was exposed after, in order to compare the stitching capabilities.

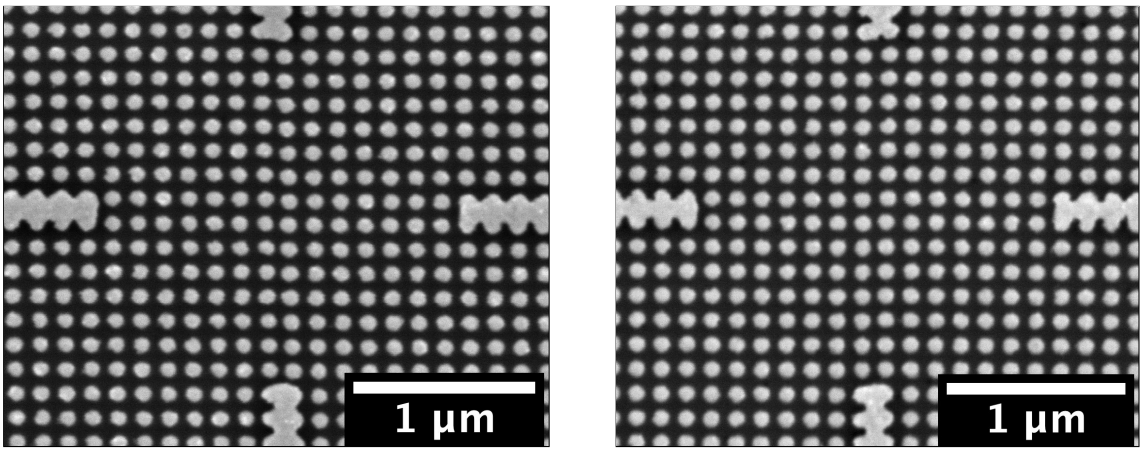

(a) Older Sample **(b)** Newer Sample

Figure 5.7: Micrographs of stitching

The micrograph shows the point at which four write fields connect, indicated by the cross marker. These markers allow measuring the average $\hat{x}$ and $\hat{y}$ displacements over a short distance. Note that a small displacement over a short distance may result in a larger displacement over a longer distance, and so this investigation does not exclude the possibility for long-range stitching errors.

Sample NOV20-1 displays an average $\hat{x}$ displacement of 32 nm and an average $\hat{y}$ displacement of 39 nm, with standard deviations of 4 nm for both cases. NOV20-2 displays displacements of 40 nm and 34 nm, with standard deviations of 5 nm and 4 nm respectively. This finding is coherent with the visual inspections, showing very little stitching errors on the border of the write fields. However, the stitching on other structures on the same wafer was not necessarily consistent with these results, as each field stitching may lead to irregular errors rather than as a main rule. Compared to the resolution of the system and the size of the structures, the results are as expected. In conclusion, the stitching

between write fields was satisfactory both before and after the re-calibration of the electron gun.

Displacement Effects

Although satisfactory to the current procedure, having stitching errors in larger arrays of patterned magnets could lead to unfavorable effects in the overall magnetic response. The dipolar coupling of the magnets is primarily linked to the distance and angle between two neighboring disks [16]. So a displacement could lead to the formation of areas with different supermagnetic ordering than intended, or more severely, become a nucleation site for further propagating other supermagnetic orders. As the goal is to observe the long-range effects of the SFM and SAFM states, respectively, the decision was made to pattern 95% of each write field, leaving gaps at the field edges to make advanced field-stitching superfluous. Patterning many write fields should still provide enough magnetic material to provide a signal in the VSM. However, this will exclude any long-range effects of an order longer than the write field, and the results will characterize the average magnetic response of an area the size of the write field.

5.2.3 Electron Gun Jumping

A curious effect appeared on the tail-end of 2020. Sample NOV20-2 (2Ti+15Au) was also exposed with a test-array of the square pattern to check that the exposure dose and dose coefficient were sufficient. This exposure led to the discovery of what appeared to be in-field stitching errors.

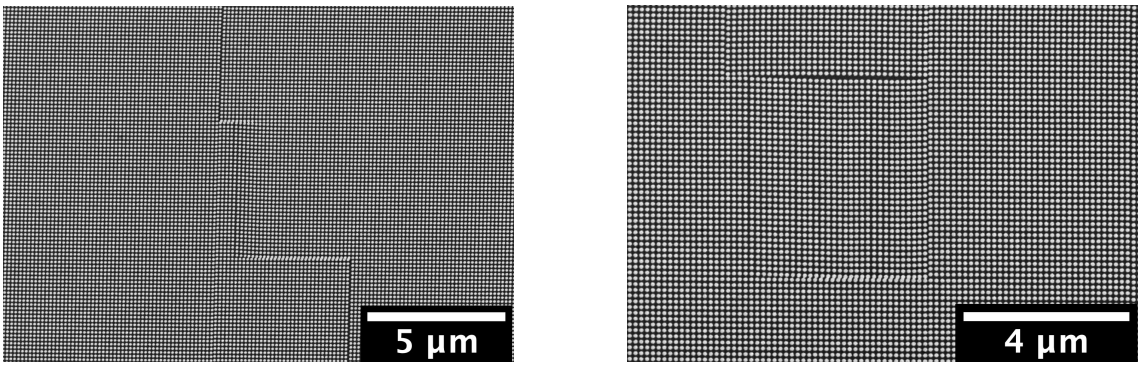

(a) **(b)**

Figure 5.8: Micrographs of sample NOV20-2 show pattern gaps as a result of beam jumping during exposure

The micrograph shows glitches in the pattern, but unlike stitching error effects, the pattern realigns itself again over a short distance. With the incredible speed with which each disk is exposed, these glitches occur and fix themselves over

a time-span of around 0.3 µs. After a full gun change to the system, the problem still persevered, and further investigation concludes that there was contamination present in the electron column. This contamination would charge up while the beam was writing and subsequently discharge, creating electromagnetic fields that moved the beam.

Aliasing - A New Method of Characterization?

An unexpected effect of the contamination in the EBL system is the discovery of a new method to characterize displacements in large areas of pattern. One of the most difficult aspects of large-area patterning is that it is not feasible to characterize every single structure, or every write field for that matter. This is a result of the sheer number of structures, as well as the micrograph resolution inability to discern every disk at a magnification that displays larger areas. Investigating these glitches in a SEM system does give rise to the possibility of discerning minuscule pattern shifts by *aliasing*.

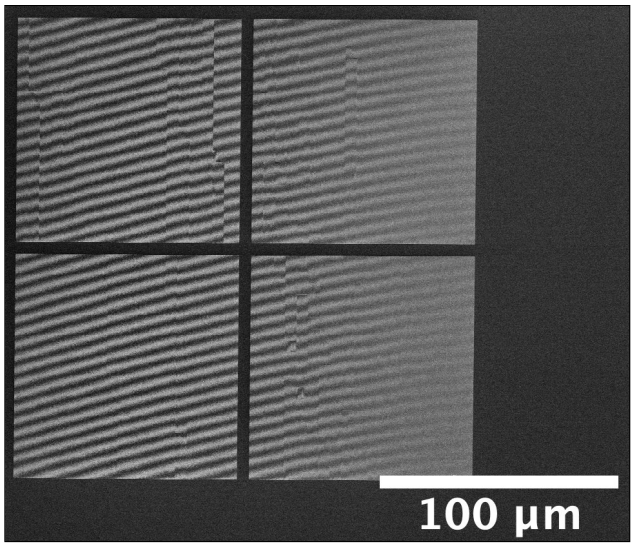

Figure 5.9: Micrograph of sample NOV20-2 with aliasing effect on arrays

Aliasing is defined as *"An error or distortion created in a digital image that usually appears as a jagged outline"* [60]. This phenomenon typically occurs when the magnification is not decent enough to resolve the spatially separate features. The resulting image displays moiré fringes, as seen in fig. 5.9, and for this case, reveals the location of pattern inconsistency due to dislocation in the fringes. Moiré fringes are highly geometrical, and further studies into the dislocation length and fringe width might make it possible to use aliasing as a new characterization method for small structures imaged at low magnification. This would enable characterization of larger areas than have been possible up until this point.

5.3 Metalization

5.3.1 Side-wall Deposition

To metalize as even a metal layer as possible, the wafer is rotated inside the e-beam evaporation systems. This rotation should ensure that even if the wafer is not mounted completely flat, the Si-surface in the holes of the resist still receives the same amount of metal. However, this is not always the case.

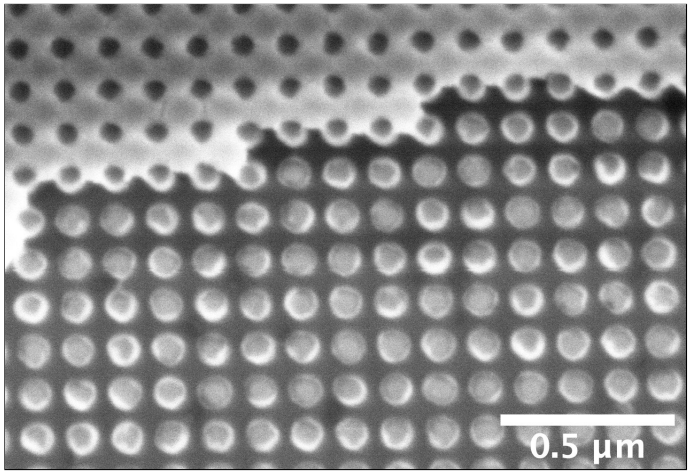

Figure 5.10: Micrograph of sample SEP20-1 displaying side wall deposition.

Sample SEP20-1 (15Py+2Al) shows clear signs of what is known as side-wall deposition, visible as a brighter ring around the patterned disks. The brightness shows that this ring is topographically higher than the rest of the disk. Along with the side-wall deposition, the micrograph shows metal remnants due to incomplete lift-off. These metal remains can result from the side-wall deposition, as it becomes more challenging for the resist stripper to "latch" onto the resist and lift-off the metal. Side-wall deposition was seen on all samples metalized in the Pfeiffer system.

5.3.2 Comparison of PVD systems

The PVD systems were compared to determine which system gave less side-wall deposition and subsequent better lift-off results. Sample DEC20-1A (20Py+2.5Al) was metalized in the AJA system, and DEC20-1B (20Py+2.5Al) was metalized in the Pfieffer system.

The micrographs in fig. 5.11 are taken at a 40° tilt, and so the height of the wall cannot be accurately measured. Also, the resist residue has led to an uneven and jagged lift-off edge. Sample DEC20-1A has an average measured skirt height of 34 nm, and sample DEC20-1B has an average measured skirt height of 66 nm. As the micrographs have been taken at the same angle and beam working

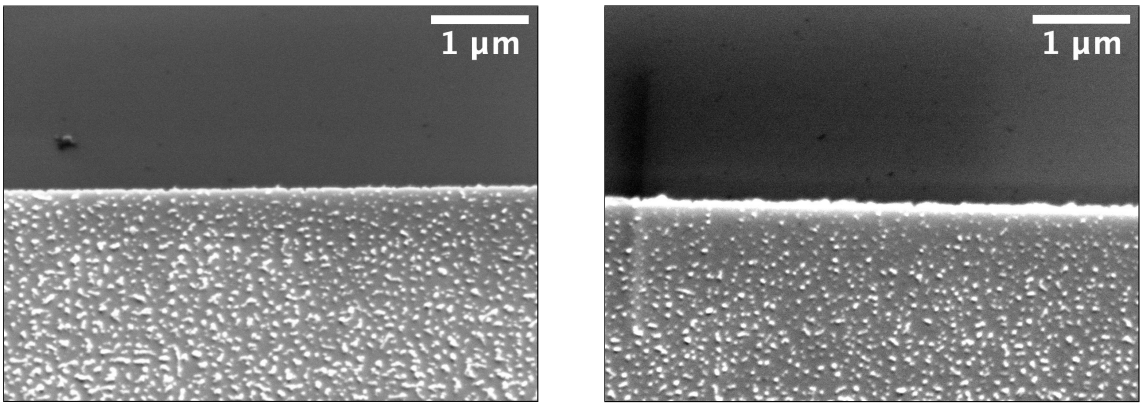

(a) DEC20-1A **(b)** DEC20-1B

Figure 5.11: Micrographs showing the metal skirts on exposed markers.

distance, the measured skirt heights are comparable. These results imply that the Pfeiffer system could be delivering almost double the amount of side-wall deposition compared to the AJA system. To a certain degree, this result is supported by the lift-off issues associated with the Pfeiffer system, see section 5.3.3.

Size comparisons

As supermagnetic ordering requires specific magnet parameters to ensure monodomain states, the fabrication process must produce the intended results. The disk sizes of samples DEC20-1A/B were compared to verify which process gave size results most consistent with the goal size. Section 5.2.1 presents the size analysis of hexagonal disks in the AJA system regarding exposure dosage. As it is quite challenging to do size analysis of disks that have surrounding metal that was not lifted off, the comparison is made only for the lowest exposure dose and square pattern. This choice is due to sample DEC20-1B only having disks available for analysis in this regime. Figure 5.12 shows the micrographs used in the analysis of the disk size.

The analysis outlines can be found in appendix B. The average area of the disks on DEC20-1A was found to be 0.00727 μm^2, while the average area of the disks for DEC20-1B was 0.00853 μm^2. As the analysis was made for the lowest exposure dose, one would expect the size of the disks to be smaller than the target area. For disks metalized in the Pfeiffer, the disks were larger than the target, so a process using this system would need to consider this disk bloating to achieve disks of the desired size. This issue might lead to re-evaluating the steps ranging back to the making of the digital masks, and so in this regard, it is more desirable to continue with metalization in the AJA system, as the produced disks have a more predictable size.

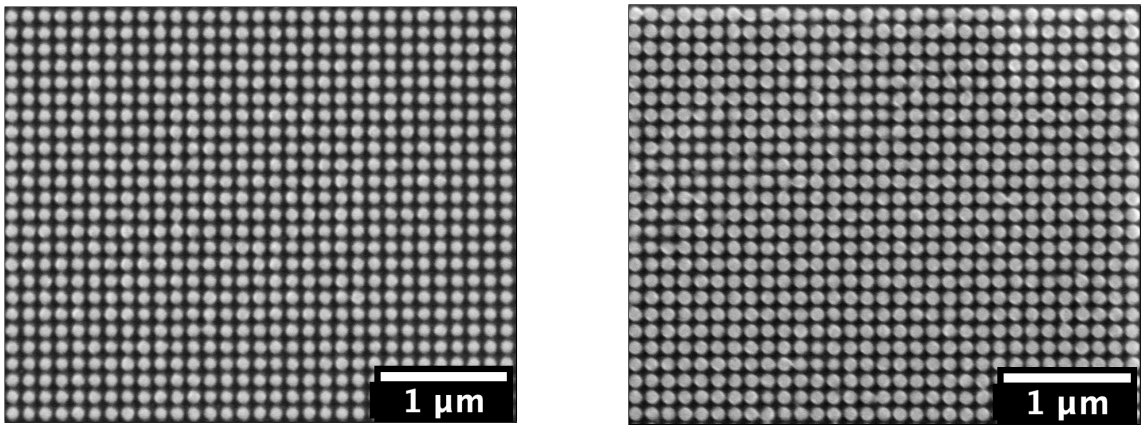

(a) DEC20-1A **(b)** DEC20-1B

Figure 5.12: Micrographs of disks used in size analysis for PVD system comparison.

VSM of Thin Films

The two metal deposition systems may deliver thin films of different magnetic qualities, so it is preferable to measure which system delivers the best quality film. The VSM system must also receive a strong enough signal from a relatively small amount of magnetic material, so the thin film measurements were also carried out for different film thicknesses and sample sizes.

Figure 5.13 shows the magnetic response of eight different samples, where four were metalized in the AJA system, and the other four were metalized in the Pfeiffer system. The samples varied in size (2 by 2 mm and 10 by 10 mm) and film thickness (5 nm and 20 nm). As the samples were scribed by hand, the sample sizes were measured by obtaining microscope images and calculating the exact areas in Fiji image analysis software. The thickness of the thin films was only verified by the comparative systems deposition measurement instruments and so could vary from the stated thicknesses. In fig. 5.13a for the 5 nm thin films, all samples display the same coercive field, while the AJA samples show a slightly higher saturation moment. The 2 mm samples produce a lower signal with more noise, as expected when there is less magnetic material on these samples. Figure 5.13b for the 20 nm thin films show the same findings but with comparatively better signal strength. As all curves show that the AJA system produces a higher signal than the Pfeiffer system, it is possible that the two systems have delivered a different film thickness than desired or that the deposition process in the Pfeiffer leads to a higher degree of oxidation of Py. This result can be explained by the introduction of air to the target at every sample loading, whereas the target in the AJA system will always be in ultra high vacuum conditions.

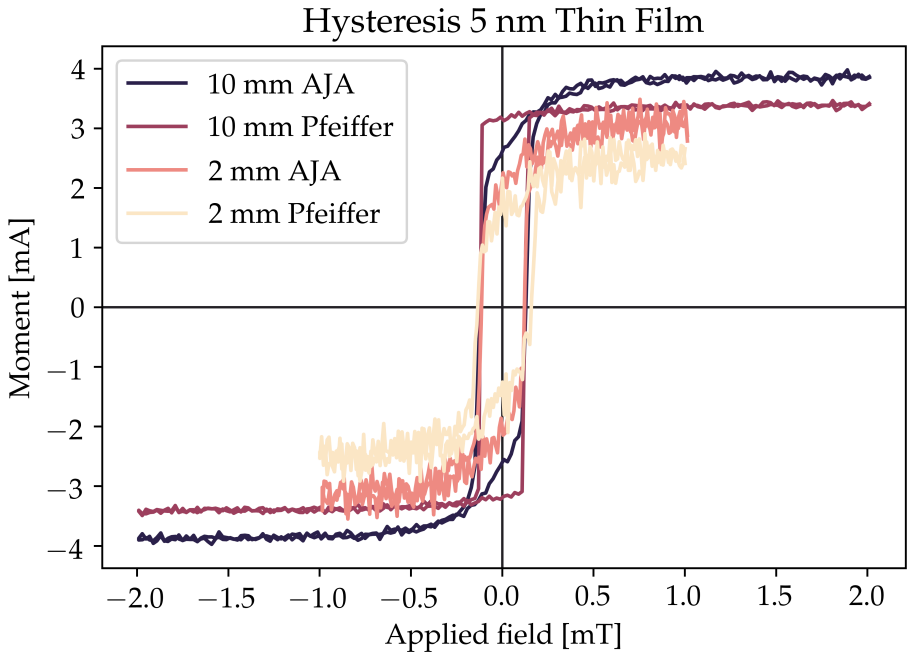

(a) 5 nm film thickness

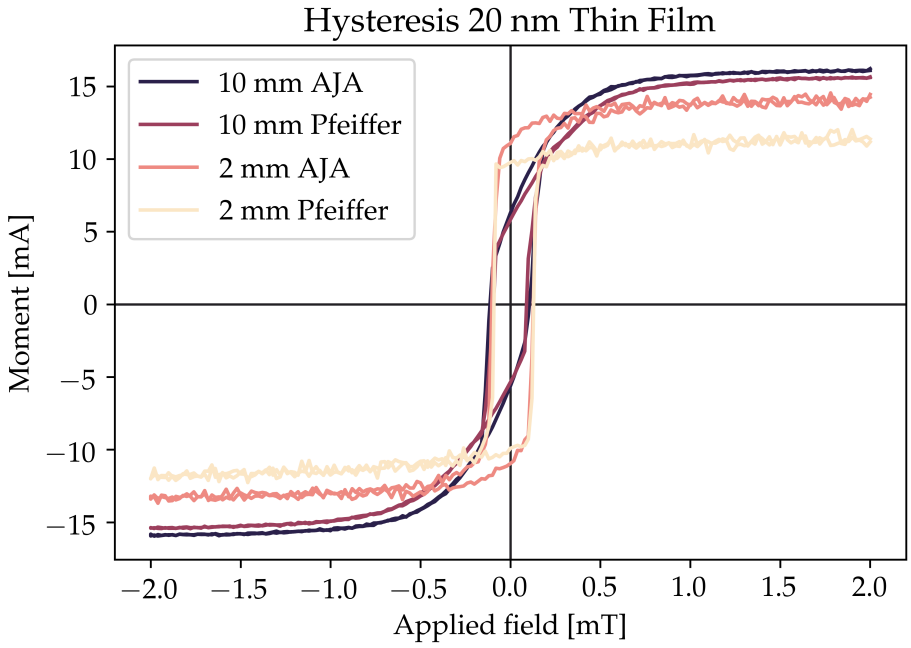

(b) 20 nm film thickness

Figure 5.13: Hysteresis of thin films deposited in the AJA and Pfeiffer system at different thicknesses and sample sizes. The curves have been normalized to the area of deposited Py.

An interesting note is that the hysteresis curves all show a tendency of shape anisotropy. Both the 10 mm Pfeiffer sample in fig. 5.13a and the 2 mm Pfeiffer sample in fig. 5.13b have a square shape, and so indicate a 180° anisotropy, the 2 mm AJA sample in fig. 5.13b displays no anisotropy, and the rest of the samples display a slight anisotropy due to the s-shape of the curve. This result can most likely be attributed to the imperfect shapes of the samples or the mounted sample orientation, as there does not seem to be a consistent pattern of anisotropy across the parameters.

The results from these measurements show that a 20 nm film gives a better signal than a thinner film and also gives a better signal-to-noise ratio, especially for the 2 mm samples which are closer to the areas that are possible to expose for the fabrication of patterned arrays. Therefore, the large patterned arrays discussed in section 5.5 were metalized with a 20 nm layer of Py in the AJA system.

5.3.3 Lift-off

The issues regarding metal lift-off were solved by using the AJA system as opposed to the Pfeiffer system. However, there is still a possibility of redeposition of metal due to flushing of resist during the lift-off process.

If the wafer is not immediately agitated when lowered into the stripper, the stripper agent may flush away the resist while the metal stays in place. After the resist is flushed away, the metal redeposits onto the substrate and is almost impossible to remove. Pre-soaking the sample before the ultrasonic bath is not recommended, while it is recommended to turn on the ultrasonic bath before the sample is lowered into the stripper.

5.4 Disk Shape Analysis

5.4.1 Examining Ellipticity

Earlier fabrications using the same process and instruments suggest that the Py disks display a considerable amount of ellipticity [19]. In this work, ellipticity is defined as $\epsilon = a/b$, where a and b are the longest and shortest axis, as seen in fig. 5.14. Note that an ellipse might not be the best shape descriptor for the disks, as the Fiji software adjust the fit of an ellipse to do this analysis.

Fabricated samples with elliptical disks might not produce the desired result, as the ellipticity introduces a shape anisotropy along the elliptic direction. An analysis of DEC20-1A using the same data as in fig. 5.12a reveals that the system does create elliptic disks as seen in fig. 5.15. For this sample, the disks are elliptical along the approximate 100° angle to the lattice. With an average ellipticity

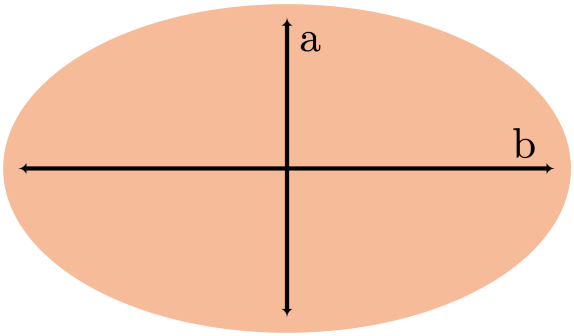

Figure 5.14: Illustration of ellipse parameters a and b.

of 1.08, amounting to about 8%. This disk deformation is significant, and must be discussed when doing magnetic measurements.

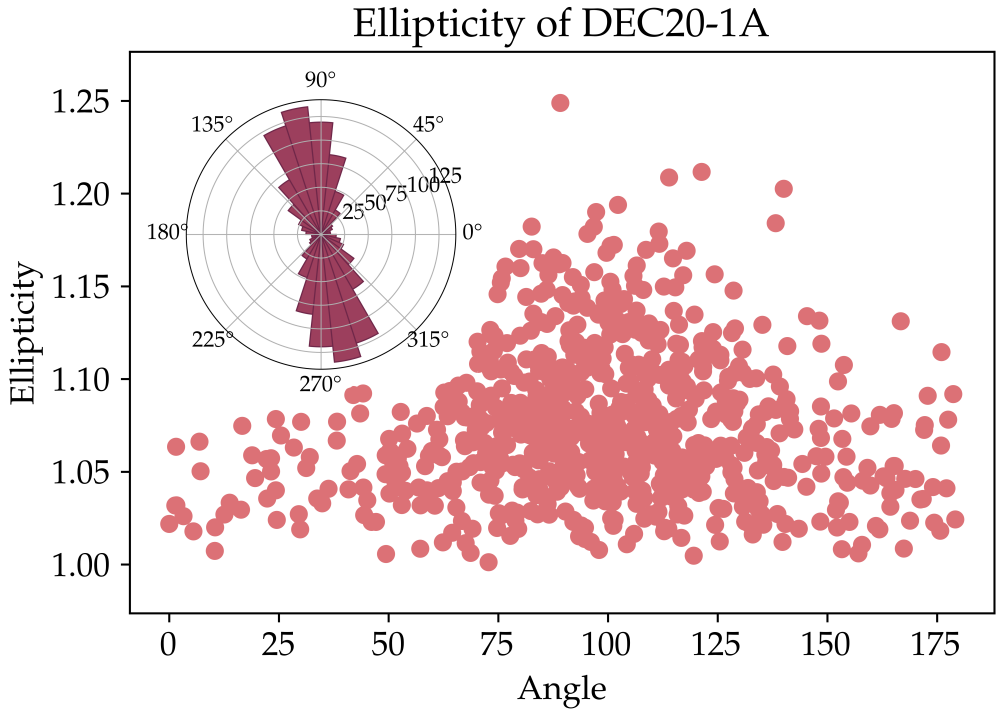

Figure 5.15: Ellipticity of sample DEC20-1A over the elliptic angle. The inset shows same results in a polar bar chart

5.5 Final Sample

This thesis work all culminates in one final sample, DEC20-2 (20Py + 2.5Al). The final sample was exposed over 22.5 hours and contained 23 by 20 exposed write fields, where each write field was filled with a 95 by 95 µm square pattern with a 140 nm disk pitch. This exposure amounts to an area of 2.3 by 2 mm, with a total metalized area equal to a 1.66 mm^2 thin film. The sample was metalized in the AJA system.

5.5.1 PEC

When creating larger arrays, it is inconvenient to create one large file for the digital mask, as the file size would be too big. Instead, one array is repeated over the desired area using the WeCas software. This choice will interfere with the PEC. As seen in fig. 5.16, the PEC doses will differ depending on the number of neighboring arrays. As the file will not contain all arrays, this poses the question of how to obtain the correct exposure dose. From the differences in fig. 5.16a and fig. 5.16b, an assumption of how the PEC would look for larger systems can be extrapolated. The total area is large enough to be approximated as a continuous pattern, meaning that all individual disks will see approximately the same amount of proximity exposure. From the blue middle-regions of fig. 5.16, the approximate correction value from PEC is a dose coefficient of 1.3. This method was used to adjust for the proximity error without running the correction program, saving file size and mask processing time. The dose coefficient adjusted the exposure dose to 286 µC/cm^2.

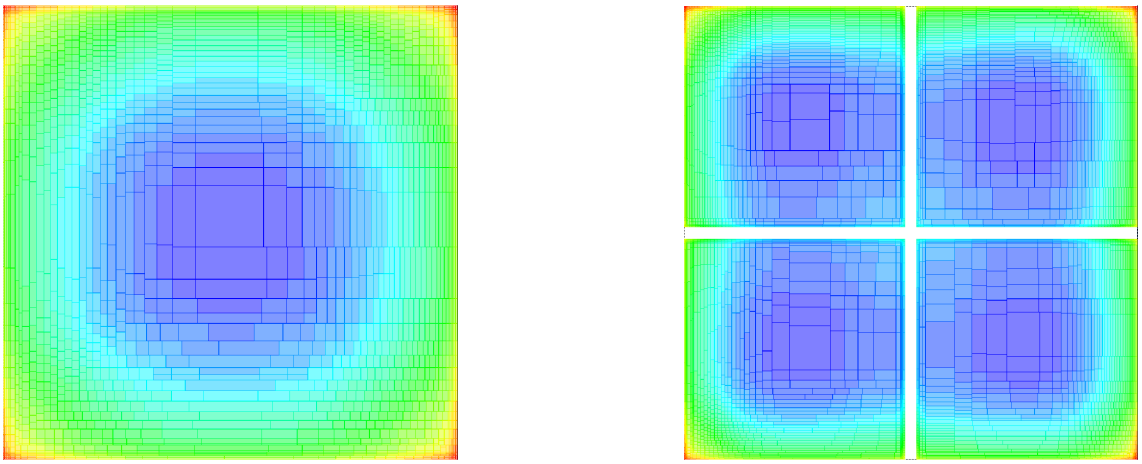

(a) One array **(b)** Four arrays

Figure 5.16: Dose map after PEC for one and four arrays from screen capture in Beamer. The colors correspond to the same dose coefficient for both maps.

5.5.2 Disk Size and Shape

To characterize the size and shape of the disks, micrographs were taken from arrays on different locations of the sample. Locations were in the middle, as well as along each of the four edges. The micrograph from the eastern edge in fig. 5.17 shows the disks at high magnification. The disks are not perfectly circular, and many display jagged edges, which may result from residual resist under the metal. The resulting micrographs from different sample areas were combined to find the average area and ellipticity of the disks.

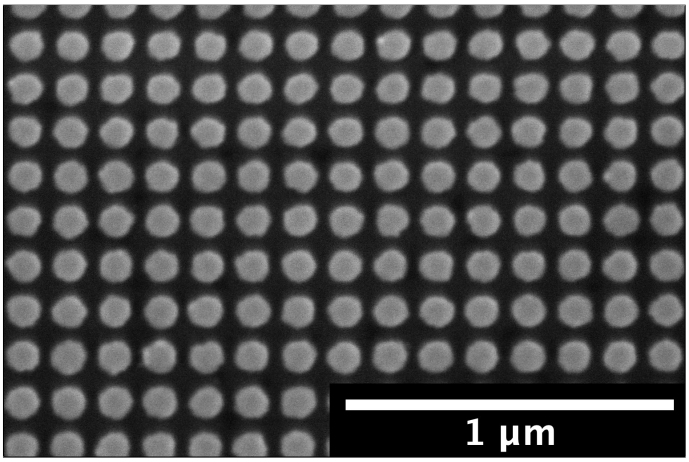

Figure 5.17: Micrograph of a small area of a large array at 100000x magnification.

The average size of the disks was found to be $0.0084\,\mu m^2$, with an average ellipticity of $\epsilon = 11\%$ at an elliptic angle of approximately 45°, as seen in fig. 5.18. Micrographs, outlines and Python code used in the analysis can be found in appendix B. Although this is larger than the expected $0.00746\ \mu m^2$ for an exposure dose of $220\,\mu C/cm^2$, it is still within an acceptable range.

5.5.3 VSM Measurements

VSM measurements were done on the sample to measure the magnetic response of the patterned arrays. The Python script written to analyze the results can be found in appendix A.3.

Diamagnetic Contributions

There was a significant diamagnetic contribution to the signal. Figure 5.19 shows the response of an empty sample holder at 0° and 90° rotation. The diamagnetic contribution to the signal from the sample holder is filtered away by subtracting the magnetic response obtained by these measurements. As the measurements for both rotations are similar, it is fair to assume there is little to no anisotropy

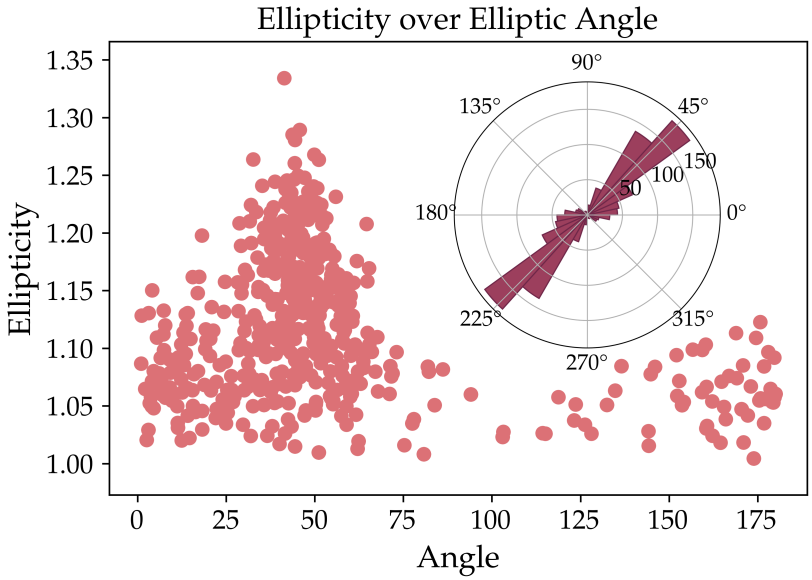

Figure 5.18: Ellipticity over angle, the inset shows the polar bar chart of the same results. For sample DEC20-2.

in the sample holder, and so the average of the measurements can be used to remove the diamagnetic signal from all of the rotations.

There should also be a small diamagnetic contribution from the silicon wafer. This addition is filtered away by rotating the obtained hysteresis loops so that the saturation plateaus are horizontal and parallel to the x-axis. This form of data processing somewhat warps the data, but it was deemed an acceptable operation for this small diamagnetic signal.

Normalization of Curves

The sample was rotated from 0° to 180° at increments of 5° to examine the sample anisotropy. While the sample rotated, it moved slightly away from the VSM saddle point for each iteration, making the last measurements display lower signal strength than the first measurement, for which the setup was optimized. Figure 5.20 shows the non-normalized measurements of 0° and 180°.

The curves were normalized by using the saturation moment from the 0° measurement as a standard. This data processing is valid as the amount of magnetic material does not change over the measurements, and it is expected that the saturation moment should be the same for all measurements. The obtained saturation magnetization for this measurement was found to be 912 A/mm, compared to the standard 860 A/mm for Py. This result may be due to the filtering step described in the previous section, as it may lead to an over-adjustment of the graph at the more extreme field strengths. Although above the standard saturation magnetization, the result is within an acceptable range.

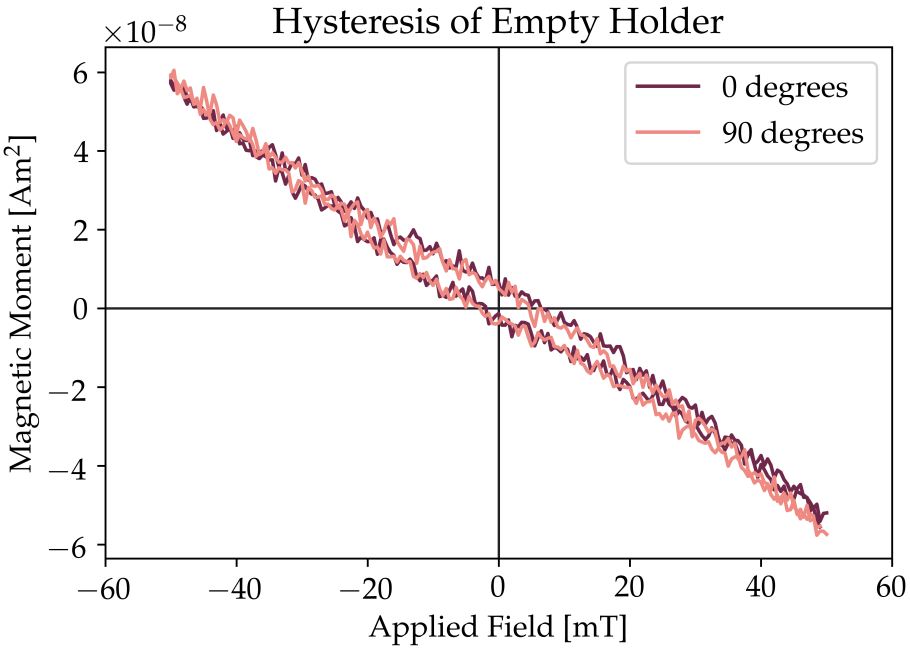

Figure 5.19: Magnetic response of the empty sample holder of the VSM system.

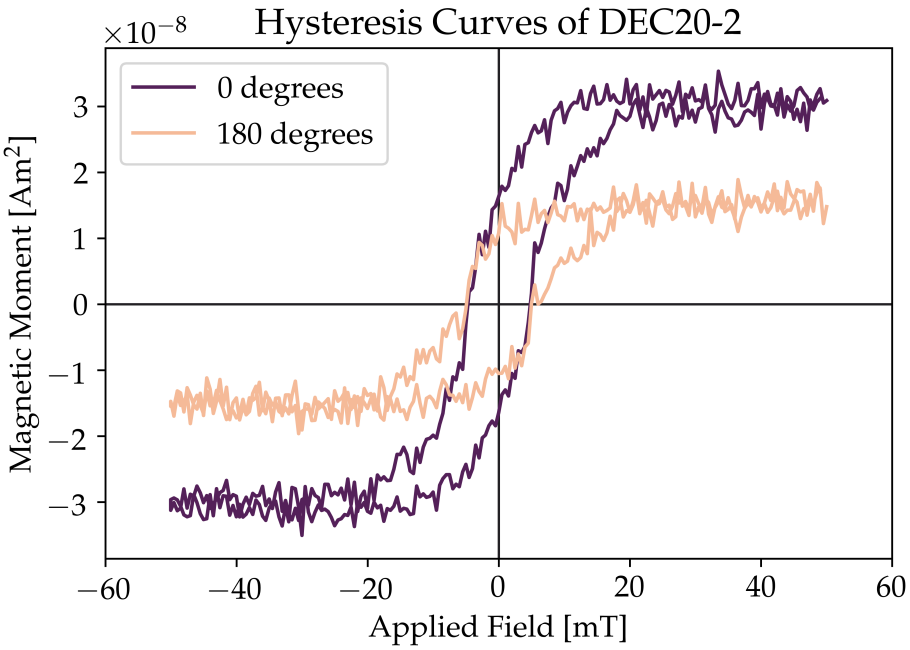

Figure 5.20: Magnetic response of sample at 0° and 180° rotations after removing diamagnetic contributions. The difference in signal strength can be attributed to the sample shifting relative to the VSM saddle point.

Central Findings

The rotations of the sample were conducted to analyze the anisotropy of the sample. Care was taken such that the first measurement was aligned with the array grids. From comparing the hysteresis curves over rotations, three are important to the discussion. The measurements of 0°, 90°, and 180° rotations (fig. 5.21), indicate a clear trend. Firstly, none of the measurements had the characteristic SAFM hysteresis that was expected for a square array. This hysteresis curve would have had a plateau around zero applied field due to the moments largely canceling for the SAFM ordering. What is seen in the results indicates a ferromagnetic ordering. However, the results show a signal response, which means that the fabricated magnets are, in fact, in the monodomain state. For a vortex state, the moments would cancel, and the response would appear paramagnetic.

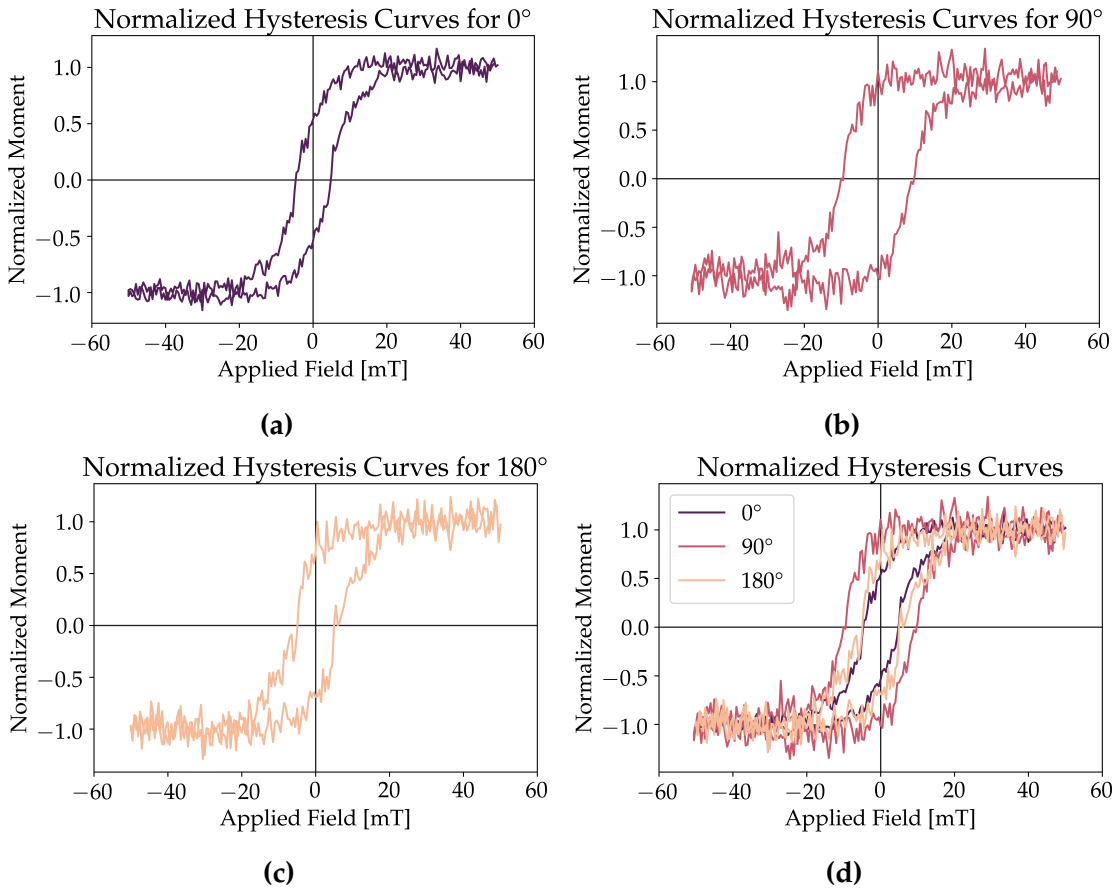

Figure 5.21: Hysteresis curves over the rotation measurements.

The curves for rotations closer to 90° show a more steep switching, indicating that the moments switch instantaneously at the coercive field. The 90° curve also shows a higher magnetic remanence. The 0° and 180° curves have more of an s-shape, implying a more gradual rotation of the moments before a required field

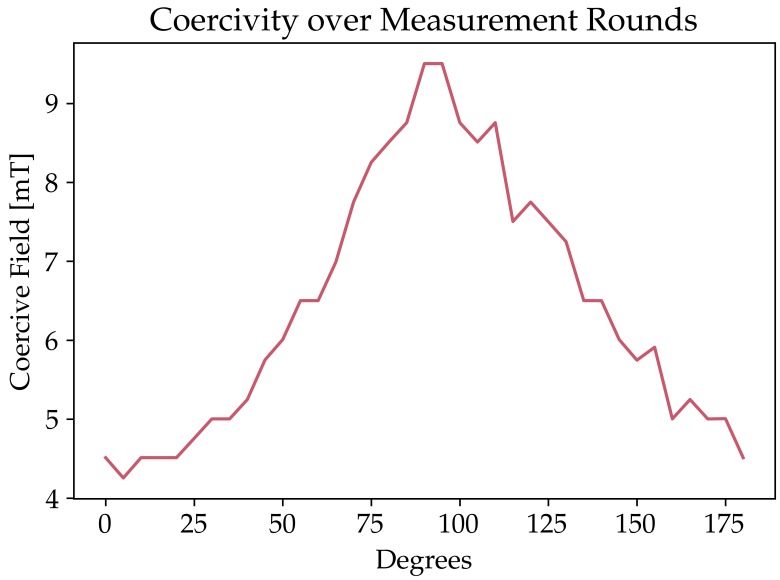

Figure 5.22: The coercive field as a function of the rotation angle.

that switches all magnets to align with the field. These findings indicate that the sample may fit the Stoner Wohlfarth (SW) model. However, the periodicity of the energy landscape is 180° rather than 90°. This finding suggests that there could be a coupling between the magnets, as individual magnets would have experienced a 90° periodicity as according to the SW model. Figure 5.22 shows how coercive field varies over the rotation angle. The coercive field is found to peak at 90°, indicating an anisotropy in the system. The disks were found to be elliptical at an average angle of 45°, which in the SW model entails easy switching at 0° and 90°. However, the SW model does not account for inter-magnet interactions.

So far, the results are not in line with what was expected. There are several possible reasons for the results. One working theory is that the shape anisotropy from the elliptical magnets and the anisotropy of the lattice are interfering with each other and that this new total anisotropy is periodic over 180°, with an easy axis along the 90° angle. This periodicity is curious, as the square lattice should remain identical when rotated 90°, and the coercive field should show a periodicity over this rotation. Therefore, it is pertinent to assume that the shape anisotropy of the magnets interact with the lattice anisotropy in such a way that the anisotropic energies cancel and create new axes of symmetry and anisotropy. It is also possible that the 90° rotation of the disks does not align with that of the lattice, and so one of the lattice directions will break symmetry, creating a 180° anisotropy.

Another option is that the disk ellipticity has distorted the lattice by decreasing the diagonal inter-disk spacing. If two diagonal disk both have 11% ellipticity in the 45° direction, in the most severe case, the inter-disk spacing may have dropped from 56 nm to 36 nm, making the diagonal lattice distance shorter than the in-line neighbors. This lattice modification has not been accounted for in previous simulations, and so further investigations are required before making a definitive conclusion.

5.5.4 Sources of Error

During the fabrication and characterization process, there are many opportunities to introduce sources of error into the analysis. Possible sources of error are be detailed below.

Mask Choices

After issues regarding lift-off, the decision was made to increase the disk pitch from 130 to 140 nm, to ensure good lift-off. The decision was based on data that shows it is still possible to achieve supermagnetic ordering at this new inter-disk spacing [20]. However, this is without accounting for the possibility of side-oxidation of the Permalloy, which may further increase the distance between disks while decreasing the radius of the effective magnetic material of the disk and followingly decrease the dipole interaction energy. This reduction may interfere with the magnetic response in the VSM.

Electron Beam Glitches

The effects of the beam jumping mid-exposure can be seen on virtually all exposed arrays. Thanks to the aliasing images, these can be viewed in micrographs without very high magnification. An interesting note is that the number of glitches per write field is not consistent or predictable. Some arrays have many, and their neighbor may have almost none, as seen in fig. 5.23. Apart from changing the inter-disk distance at the glitch location and sometimes creating adjoining disks, just as in stitching errors, the glitches did no considerable changes to the arrays.

As using aliasing for imaging pattern disruptions is a relatively new technique, no other information can be read from the micrographs other than that there is a pattern defect at the location of the discontinuities.

Oxidation of Permalloy

When the decision to use a 20 nm thickness of Py was made, the main concern was to increase the signal strength. However, in increasing the height of each disk, the exposed side areas were also doubled. As the disk walls were not

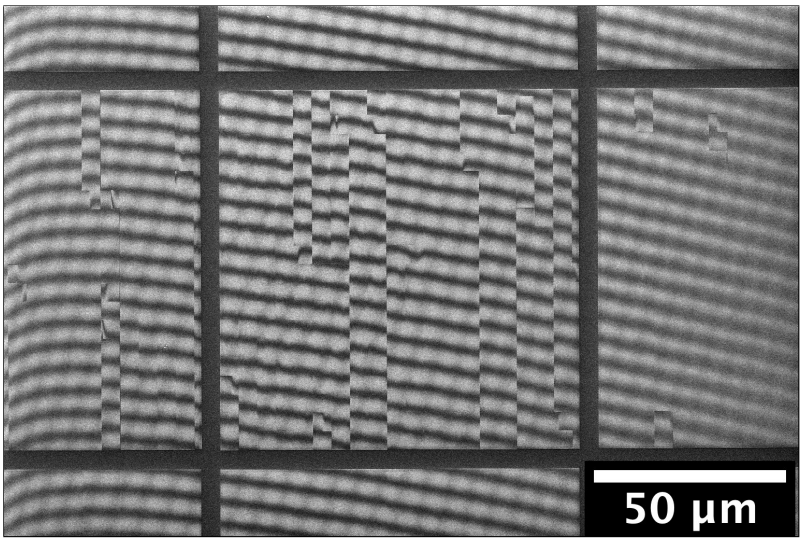

Figure 5.23: Aliasing in micrograph of DEC20-2 shows pattern disruptions after electron beam jumping during EBL exposure.

capped with Al, these areas run the risk of oxidation. In doubling the height of these areas, the effective percentage of exposed Py per disk also doubled. The main issue with this possible oxidation is that it is unknown how much of each disk has oxidated. It is possible that this oxidation allowed the disk to be single-domain by lowering the effective radius. The oxidation of Permalloy may also weaken the magnetic signal so that the signal strength may have been as strong for a 10 nm disk height. The case for disks is different from the comparisons done in section 5.3.2, as these films can be approximated as infinitely larger in surface than in height.

Pattern Scratch

A long scratch is found on the north-east side of the sample as seen in fig. 5.24, most likely obtained during handling. This scratch causes a pattern disruption, but as the defect does not apply to all arrays, its effects should be small compared to the signal of the entire sample.

Sample Contamination

Residual resists under the patterned metal may have distorted the disk edges and subsequently added a new shape anisotropy to each disk. As the residue should be random but evenly dispersed throughout the sample, this erroneous anisotropy should be averaged out over an array.

The VSM measurements were carried out in a non-cleanroom environment in the presence of other magnetic samples. These polluted conditions make the possibility of magnetic contaminants polluting the sample much higher. The

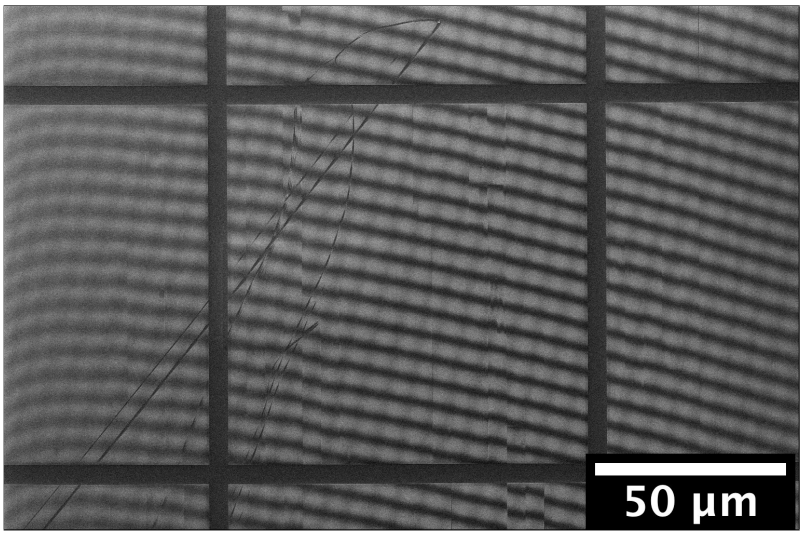

Figure 5.24: Micrograph of scratch found north-east on the sample.

sample holder was also sanded down to better fit the sample, with sandpaper that had previously been used to sand down magnetic geological samples. This sanding makes it highly likely that contamination exists on the sample holder and possibly the sample itself.

VSM Measurements

When the measurements were done, the rotation of the sample holder moved the sample out of the VSM saddle point. This dislocation led to lower signal strength and more noise for measurements, markedly from around a 40° rotation and out. These measurements have a higher degree of uncertainty than measurements obtained closer to the saddle point, which must be considered when analyzing the saturation moment. For these samples, as all hysteresis curves were normalized to curve of the first rotation, this error is most noticeable as an increase in signal noise. As the alignment of the sample at the first 0° orientation was aided by eyesight as the noise made it difficult to align to maximum signal strength, the alignment of the lattice and the field might not be accurate. This error would mostly affect the magnetic measurements.

Data Analysis

After obtaining the micrographs and VSM measurements, the data was processed. While processing micrographs in Fiji, it is difficult to get the correct threshold boundaries for the disks, as the pixel precision will vary with both brightness and contrast. To combat this effect, micrographs that are to be compared are imaged at the same system settings with as few as possible changes between the imaging. The brightness and contrast are also equalized between

the images. The VSM measurements were to a certain degree manipulated during the analysis, as the graphs were rotated to a flat saturation plateau to filter a diamagnetic contribution from the Si substrate and contamination. In this rotation, the values for high field measurements may be over-adjusted, which may lead to an abnormally high saturation moment.

Table 5.2: Index Table of Fabricated Samples

Name	**Dil. / Th.**	**Doses**	**Metalization**	**System**
SEP20-1	8.5:6 / 164 nm	180 - 240 µC/cm²	15 nm Py + 2 nm Al	Pfeiffer
SEP20-2	2:1 / 88 nm	180 - 240 µC/cm²	15 nm Py + 2 nm Al	Pfeiffer
OCT20-3	8.5:6 / 164 nm	200 µC/cm²	10 nm Py + 2 nm Au	Pfeiffer
NOV20-1	2:1 / 110 nm	180 - 220 µC/cm²	2 nm Ti + 15 nm Au	Pfeiffer
NOV20-2	2:1 / 110 nm	180 - 220 µC/cm²	2 nm Ti + 15 nm Au	Pfeiffer
DEC20-1A	2:1 / 110 nm	180 - 220 µC/cm²	20 nm Py + 2.5 nm Al	AJA
DEC20-1B	2:1 / 110 nm	180 - 220 µC/cm²	20 nm Py + 2.5 nm Al	Pfeiffer
DEC20-2	2:1 / 110 nm	220 µC/cm²	20 nm Py + 2.5 nm Al	AJA

Chapter 6

Conclusion

6.1 Iteration of Fabrication Process

After running the fabrication process several times, only incremental improvements are suggested to the existing steps.

Wafer Cleaning and Resist Deposition

The Si wafer is soaked in an acetone bath for 5 minutes before being thoroughly rinsed with IPA and dehydration baked on a hot plate at 100 °C for 5 minutes. CSAR62 is then deposited by spin-coating with an acceleration of 1000 rotations per second, a final spin speed of 4000 rpm for 60 seconds. After spin-coating the wafer is soft-baked at 150 °C for 1 minute. This process remains largely the same as for previous projects.

Exposure

When fabricating new samples, the EBL system should be free from contamination when creating larger arrays. A base exposure dose of 220 µC/cm² for a 500 pA beam current and 120 µm aperture was found to be sufficient for the patterns in question. It is also important that the digital mask has the same resolution as the EBL system in creating small structures. It was found acceptable for larger arrays not to apply PEC but rather use one dose coefficient for the entire pattern. For a 95 by 95 µm array with a square lattice, the suitable dose coefficient was found to be 1.3.

Development

The development should be done the same way as previous projects, by submerging the sample in AR-600-546 developer for 1 minute, followed by a thorough rinse and 1 minute bath in IPA before the sample is dried with a nitrogen gun. It is not recommended to skip the IPA step. To avoid redeposited resist

particles after the development stage, a new step in the fabrication process is suggested. A descumming step can be done by plasma cleaning the wafer for around 30 seconds and should remove any unwanted residue. The exact instrument parameters and process time should be further investigated and verified to fine-tune this fabrication process step.

Metalization and Lift-off

The recommended metalization system for this process is the AJA International Custom ATC-2200V. For this system, it is possible to achieve lift-off for deposition thicknesses at least up to 20 nm. The preferred capping layer metal is Al.

The lift-off process should be ultrasonically assisted in AR600-71 remover for at least 10 minutes, possibly more depending on Py thickness. The sample should only be lowered into the remover while the beaker is subject to ultrasonic vibrations or other agitation, as the resist CSAR 62 flushes away quite quickly, and there is a risk of metal redepositing on the substrate. After lift-off, the sample should be rinsed and bathed first in acetone and subsequently IPA before being dried with a nitrogen gun.

6.1.1 Wafer Scribing

The sample is mostly handled with a carbon tweezer to avoid the metal tweezers, which may deposit iron particles onto the sample. These particles will be a great source of error. The only part of the process where the sample was handled with metal tweezers was during scribing because the carbon tweezers are too flexible to break the Si wafer. To circumvent this use of metal tweezers, a new method of scribing is suggested. In this method, tape is used in place of metal to create enough friction and force to break the sample after the initial scribe. Tape should be attached to a sturdy stick and the backside of the wafer, and then the breaking is done by firmly rotating the stick outward while holding the piece to be scribed off with a tweezer. Although this scribing process might be unprecise, it is not advised to use more advanced scribing instruments, as these typically require water flow, which may contaminate the sample or wash away any deposited resist.

6.2 Supermagnetic Arrays

A sample with a patterned area of 1.66 mm^2 was produced. While the pattern is not continuous, this is still in line with the directive of this work. The VSM results indicate that the created disks are single-domain but that the magnetic ordering is not in the predicted superantiferromagnetic state. This result could

not be exclusively due to the ellipticity of the disks, as this would produce a response periodicity of 90° as in the Stoner Wohlfarth model. Instead, the theory is that the lattice anisotropy and shape anisotropy interact to introduce a new energetically favorable easy axis to the system, which produces a response periodicity of 180°. This result might be a useful finding, as square patterns are less dense than the hexagonal patterns that typically produce the superferromagnetic state and have a shorter fabrication time. The origin of the obtained magnetic ordering and anisotropy is still unknown and should be subject to further investigation. Suggestions for further work on this can be read in section 7.1.

In summary, the created sample displays a novel way of producing room-temperature superferromagnetic materials with a 180° periodicity while displaying a 45° disk ellipticity angle with the direction of the lattice.

6.3 In Conclusion

Much like with the paradigm of the transistor, it is impossible to know just what lies ahead with the new era of magnet-based computation and technology. Novel ways to produce and fabricate magnetic materials such as the one presented in this work may be the key to unlocking the full potential of these technologies and going beyond Moore's law. This work is just a step along the way to large-scale implementation of the fabrication of supermagnetic metamaterials.

Chapter 7

Further Work

7.1 Further Characterization of DEC20-2

Further investigations regarding the fabricated DEC20-2 sample, to understand the mechanisms behind the displayed magnetic response entirely, are in order. A first step would be to do VSM measurements over a full 360° rotation in order to determine if any other weird anisotropies are present. Another relevant VSM measurement is to vary the temperature for each measurement to see how the magnetic response evolves with temperature. Then, investigations using a MFM, XPEEM or SQUID may be used to verify the supermagnetic state on a magnet-to-magnet basis, and provide more information on the easy axis of the individual disk and the total lattice system. Once the EBL system is back to regular operation, it is possible to remake the larger arrays, both with 130 and 140 nm lattice pitch in order to compare and see if the 30 nm disk spacing changes the supermagnetic ordering. Samples with different disk heights, as well as continuous patterns, could be interesting to investigate. Also, making arrays with magnets that are decidedly uncoupled would give results that could be compared to a coupled magnet system.

An examination of the side oxidation of the disks could also provide valuable information to the field of nanomagnet fabrication with Py in general. A different solution is to run simulations of a system that displays the same lattice and disk parameters that have been fabricated. This simulation could, for example, be done in MuMax3 [61]. These simulations can simulate the magnetic response for different temperatures and field angles and provide valuable insight into results obtained in this work. It is also possible that the simulated "perfect" system gives a different response than the one recorded in the real world, in which case the observed results could be due to sample contamination, the EBL-induced errors, or other unknown circumstances.

7.2 Tailored Anisotropy and Patterns

Beyond the investigations into the samples from this work, there are many other tangential areas of interest for the study of supermagnetic metamaterials. A natural next step would be to create larger arrays of the disks in the hexagonal lattice. Further, the honeycomb lattice structure could also be fabricated, and the magnetic responses could be compared to both the results obtained in this work, and other magnetic measurements.

As an area of interest is to tailor magnetic materials to the desired magnetic qualities, introduction of pattern defects such as magnet distortions could be introduced to well-characterized patterns. Defects that can be investigated include different degrees and angles of disk ellipticity in relation to the lattice. Also, different lattice defects might be yield fruitful results, such as changing lattice pitches and using different lattice pitches in the $\hat{x}$ and $\hat{y}$ directions.

Bibliography

[1] J. M. D. Coey. *Magnetism and Magnetic Materials.* Cambridge University Press, 2010. ISBN: 9780521816144. DOI: 10.1017/CBO9780511845000.

[2] C.-G. Stefanita. "Traditional Magnetism". In: *Magnetism: Basics and Applications*. Berlin, Heidelberg: Springer Berlin Heidelberg, 2012, pp. 1–38. ISBN: 978-3-642-22977-0. DOI: 10.1007/978-3-642-22977-0_1.

[3] J.-P. Wang. "Tilting for the Top". In: *Nature Materials* 4.3 (Mar. 2005), pp. 191–192. DOI: 10.1038/nmat1344.

[4] G. O'Regan. "Early Commercial Computers and the Invention of the Transistor". In: *Introduction to the History of Computing: A Computing History Primer*. Cham: Springer International Publishing, 2016, pp. 83–91. ISBN: 978-3-319-33138-6. DOI: 10.1007/978-3-319-33138-6_6.

[5] G. E. Moore. "Cramming More Components onto Integrated Circuits". In: *Electronics* 38.8 (Jan. 1998), pp. 114–117. ISSN: 00189219. DOI: 10.1109/JPROC.1998.658762.

[6] M. L. Hammond. "Moore's Law: The First 70 Years". English. In: *Semiconductor International* 27.4 (Apr. 2004), pp. 51–52.

[7] M. Lundstrom. "Moore's Law Forever?" In: *Science* 299.5604 (Jan. 2003), pp. 210–1. DOI: 10.1126/science.1079567.

[8] M. Y. Li et al. "How 2D Semiconductors Could Extend Moore's Law". In: *Nature Mater* 567.7747 (Mar. 2019), pp. 169–170. ISSN: 14764687. DOI: 10.1038/d41586-019-00793-8.

[9] V. K. Khanna. "Trigate FETs and FINFETs". In: *Integrated Nanoelectronics: Nanoscale CMOS, Post-CMOS and Allied Nanotechnologies*. New Delhi: Springer India, 2016, pp. 109–127. ISBN: 978-81-322-3625-2. DOI: 10.1007/978-81-322-3625-2_7.

[10] C. Sealy. "CNT Transistors push Towards the Ultimate Limit". In: *Nano Today* 13 (Apr. 2017), pp. 1–2. ISSN: 1748-0132. DOI: 10.1016/j.nantod.2017.02.004.

[11] Anderson, N. G. and Bhanja, S. *Field-Coupled Nanocomputing State-of-the-Art*. Tech. rep. 2014. DOI: 10.1007/978-3-662-43722-3.

[12] R. P. Cowburn et al. "Single-Domain Circular Nanomagnets". In: 83.5 (Aug. 1999), pp. 1042–1045. DOI: 10.1103/physrevlett.83.1042.

[13] S. D. Slöetjes et al. "Tailoring the Magnetic Order in a Supermagnetic Metamaterial". In: *AIP Advances* 7.5 (May 2017), p. 056325. ISSN: 2158-3226. DOI: 10.1063/1.4978319.

[14] J. Legendre and K. Le Hur. "Magnetic Topological Kagome Systems". In: *Physical Review Research* 2.2 (May 2020). ISSN: 2643-1564. DOI: 10.1103/physrevresearch.2.022043.

[15] S. H. Skjærvø et al. "Advances in Artificial Spin Ice". In: *Nature Reviews Physics* 2.1 (Nov. 2020), pp. 13–28. DOI: 10.1038/s42254-019-0118-3.

[16] N. Leo et al. "Collective Magnetism in an Artificial 2D XY Spin System". In: *Nature Communications* 9.1 (Dec. 2018), p. 2850. ISSN: 2041-1723. DOI: 10.1038/s41467-018-05216-2.

[17] M. Varón et al. "Dipolar Magnetism in Ordered and Disordered Low-Dimensional Nanoparticle Assemblies". In: (Feb. 2013). DOI: 10.1038/srep01234.

[18] S. Bedanta et al. "Magnetic Nanoparticles: A Subject for Both Fundamental Research and Applications". In: *Journal of Nanomaterials* (Dec. 2013), p. 22. DOI: 10.1155/2013/952540.

[19] E. Digernes et al. "Direct Imaging of Long-Range Ferromagnetic and Antiferromagnetic Order in a Dipolar Metamaterial". In: *Physical Review Research* 2 (Feb. 2020). DOI: 10.1103/PhysRevResearch.2.013222.

[20] R. Streubel et al. "Spatial and Temporal Correlations of XY Macro Spins". In: *Nano Letters* 18.12 (Sept. 2018), pp. 7428–7434. DOI: 10.1021/acs.nanolett.8b01789.

[21] J. W. Lau and J. M. Shaw. *Magnetic Nanostructures for Advanced Technologies: Fabrication, Metrology and Challenges*. Aug. 2011. DOI: 10.1088/0022-3727/44/30/303001.

[22] B. D. Cullity and C. D. Graham. *Introduction to Magnetic Materials*. Hoboken, USA: John Wiley & Sons, Inc., Nov. 2008. ISBN: 9780470386323. DOI: 10.1002/9780470386323.

[23] S. Blundell. *Magnetism in Condensed Matter*. Oxford Master Series in Condensed Matter Physics. OUP Oxford, 2001. ISBN: 9780198505921. DOI: 10.1119/1.1522704.

[24] A. Zangwill. *Modern Electrodynamics*. Cambridge University Press, 2012. ISBN: 9781139034777. DOI: 10.1017/cbo9781139034777.

[25] S. Bedanta and W. Kleemann. "Supermagnetism". In: *Journal of Physics D: Applied Physics* 42.1 (Dec. 2009), p. 13001. DOI: 10.1088/0022-3727/42/1/013001.

[26] E. C. Stoner and E. P. Wohlfarth. "A Mechanism of Magnetic Hysteresis in Heterogeneous Alloys". In: *Philosophical Transactions of the Royal Society of London. Series A, Mathematical and Physical Sciences* 240.826 (May 1948), pp. 599–642. ISSN: 0080-4614. DOI: 10.1098/rsta.1948.0007.

[27] A. Gowan, P. Meggs, and C. Ashwin. "A History of Graphic Design". In: *Design Issues* (Mar. 1984). ISSN: 1531-4790. DOI: 10.2307/1511549.

[28] C. Mack. *Fundamental Principles of Optical Lithography : The Science of Microfabrication.* Wiley-Interscience, 2007. ISBN: 9780470727300.

[29] M. Quirk and J. Serda. *Semiconductor Manufacturing Technology*. 1st. Pearson, 2000, p. 666. ISBN: 0130815209.

[30] Z. Cui. *Nanofabrication: Principles, Capabilities and Limits: Second Edition*. Springer International Publishing, Jan. 2017, pp. 1–432. ISBN: 9783319393612. DOI: 10.1007/978-3-319-39361-2.

[31] M. Stepanova and S. Dew. *Nanofabrication: Techniques and principles*. 2014. ISBN: 9783709104248. DOI: 10.1007/978-3-7091-0424-8.

[32] K. M. Gupta and N. Gupta. "Semiconductor Growth Techniques and Device Fabrication". In: Springer, Cham, 2016, pp. 445–473. DOI: 10.1007/978-3-319-19758-6_13.

[33] D. Rogers. "Nanolithography". In: Springer, Berlin, Heidelberg, 2007, pp. 65–97. DOI: 10.1007/978-3-540-37578-4_2.

[34] K. A. Reinhardt and W. Kern. *Handbook of Silicon Wafer Cleaning Technology*. Elsevier Inc., Mar. 2018, pp. 1–760. ISBN: 9780323510851. DOI: 10.1016/C2016-0-01001-X.

[35] R. Reichelt. "Scanning Electron Microscopy". In: *Science of Microscopy*. Ed. by P. W. Hawkes and J. C. H. Spence. New York, NY: Springer New York, 2007, pp. 133–272. ISBN: 978-0-387-49762-4. DOI: 10.1007/978-0-387-49762-4_3.

[36] D. M. Tennant and A. R. Bleier. "Electron Beam Lithography of Nanostructures". In: *Comprehensive Nanoscience and Technology* 4 (Nov. 2011), pp. 35–62. DOI: 10.1016/B978-0-12-374396-1.00120-3.

[37] J. C. H. Spence. *High-Resolution Electron Microscopy*. Fourth ed. Vol. 9780199552. Oxford: OUP Oxford, 2013, pp. 1–424. ISBN: 9780191708664. DOI: 10.1093/acprof:oso/9780199552757.001.0001.

[38] R. F. Egerton. "Electron Optics". In: *Physical Principles of Electron Microscopy*. Boston, MA: Springer US, 2005, pp. 27–55. DOI: 10.1007/0-387-26016-1_2.

[39] B. J. Inkson. "Scanning Electron Microscopy (SEM) and Transmission Electron Microscopy (TEM) for Materials Characterization". In: *Materials Characterization Using Nondestructive Evaluation (NDE) Methods*. Elsevier Inc., Apr. 2016, pp. 17–43. ISBN: 9780081000571. DOI: 10.1016/B978-0-08-100040-3.00002-X.

[40] T. R. Groves. "Electron Beam Lithography". In: Elsevier, 2014, pp. 80–115. DOI: 10.1533/9780857098757.80. URL: https://dx.doi.org/10.1533/9780857098757.80.

[41] A. M. Kahng. "Yield- and Cost-Driven Fracturing for Variable Shaped-Beam Mask Writing". In: *24th Annual BACUS Symposium on Photomask Technology*. Ed. by W. Staud and J. T. Weed. Vol. 5567. 6. SPIE, Dec. 2004, p. 360. DOI: 10.1117/12.568526.

[42] S. Foner. "Versatile and Sensitive Vibrating Sample Magnetometer". In: *Review of Scientific Instruments* 30.7 (Dec. 1959), pp. 548–557. DOI: 10.1063/1.1716679. URL: https://dx.doi.org/10.1063/1.1716679.

[43] A. O. Adeyeye and G. Shimon. "Growth and Characterization of Magnetic Thin Film and Nanostructures". In: *Handbook of Surface Science*. Vol. 5. Elsevier B.V., Jan. 2015, pp. 1–41. ISBN: 9780444626349. DOI: 10.1016/B978-0-444-62634-9.00001-1.

[44] Occupational and Environmental Health Team. *Hazard Prevention and Control in the Work Environment: Airborne Dust Chapter 1-Dust: Definitions and Concepts*. Tech. rep. 1999, Chapter 1.

[45] NTNU NanoLab. *The Cleanroom Booklet 2.ed*. Tech. rep. 2018.

[46] *Positive E-Beam Resists AR-P 6200 (CSAR 62) Datasheet*. https://www.allresist.com/wp-content/uploads/sites/2/2020/03/AR-P6200_CSAR62english_Allresist_product-information.pdf. (Visited on 03/01/2020).

[47] *AR-600-546 Developer*. Tech. rep. URL: https://www.allresist.com/wp-content/uploads/sites/2/2020/03/AR600-50-51-55-56-546-548-549_english_Allresist_product_information.pdf (visited on 01/13/2021).

[48] A. N. McCaughan. *Welcome to Phidl's documentation! A PHIDL documentation*. URL: https://phidl.readthedocs.io/en/latest/.

[49] *LayoutEditor — LayoutEditor Documentation*. URL: https://www.layouteditor.org/ (visited on 01/12/2021).

[50] *BEAMER - GenISys GmbH*. URL: https://www.genisys-gmbh.com/beamer.html (visited on 01/12/2021).

[51] *Elionix ELS-G100 System*. URL: https://www.sts-elionix.com/product/els-g100/ (visited on 01/12/2021).

[52] J. Li et al. "Comparing Artificial Frustrated Magnets by Tuning the Symmetry of Nanoscale Permalloy Arrays". In: *Physical Review B* (Mar. 2010). DOI: 10.1103/PhysRevB.81.092406.

[53] X. Zhou et al. "Large Area Artificial Spin Ice and Anti-Spin Ice Ni 80 Fe 20 Structures: Static and Dynamic Behavior". In: *Advanced Functional Materials* (Jan. 2016). ISSN: 1616-3028. DOI: 10.1002/adfm.201505165.

[54] *Remover AR 600-71 - Allresist EN*. URL: https://www.allresist.com/portfolio-item/remover-ar-600-71/ (visited on 01/13/2021).

[55] S. Rosvoll. "Modelling and Nanofabrication of Magnetic Metamaterials". 2020.

[56] Allresist GmbH. *Storage and Aging*. http://www.allresist.com/general-process-information-storage-ageing/. Accessed: 2021-02-19.

[57] MicroChemicals GmbH. *Resist Troubleshooting*. 2012.

[58] S. Yasin, D. G. Hasko, and H. Ahmed. "Fabrication of 5 nm Width Lines in Poly(methylmethacrylate) Resist Using a Water:Isopropyl Alcohol Developer and Ultrasonically-Assisted Development". In: *Applied Physics Letters* 78.18 (Apr. 2001), pp. 2760–2762. ISSN: 00036951. DOI: 10.1063/1.1369615.

[59] S. Yasin, M. N. Khalid, and D. G. Hasko. "Reduction in Roughness of Resist Features in PMMA due to the Absence of a Rinse". In: *Japanese Journal of Applied Physics, Part 1: Regular Papers and Short Notes and Review Papers* 43.10 (Oct. 2004), pp. 6984–6987. ISSN: 00214922. DOI: 10.1143/JJAP.43.6984.

[60] *Aliasing — Definition of Aliasing by Merriam-Webster*. URL: https://www.merriam-webster.com/dictionary/aliasing (visited on 02/22/2021).

[61] A. Vansteenkiste et al. "The Design and Verification of MuMax3". In: *AIP Advances* 4.10 (Oct. 2014), p. 107133. ISSN: 21583226. DOI: 10.1063/1.4899186.

Appendix A

Python Code

A.1 Digital Mask

```
from __future__ import division, print_function, absolute_import
import numpy as np
import math

from phidl import Device, Layer, LayerSet, make_device
from phidl import quickplot as qp # Rename "quickplot()" to the
    easier "qp()"
import phidl.geometry as pg
import phidl.routing as pr
import phidl.utilities as pu

""" Imports for text rendering """
from matplotlib.font_manager import FontProperties
from matplotlib.textpath import TextPath
import gdspy

#Function that calculates stepsize
def st(radius,width):
    st = 2*radius + width #calculates stepsize
    return st

#Function that calculates the half-width of the hexagon
def hw(stepsize):
    hw = np.sqrt(stepsize**2-(stepsize/2)**2) #hexagonal half-width
    return hw


#Funtions to determine how many rows and columns should be used
def numDotsX(stepsizeX,arraysizeX):
    N = math.ceil(arraysizeX/stepsizeX)
    return N

def numDotsYHex(hexhalfwidth,arraysizeY):
```

```
    N = math.ceil(arraysizeY/hexhalfwidth)
    return N


#Functions to create arrays
def square(radius,width,arraysizeX,arraysizeY):
    st = 2*radius + width #calculates stepsize
    NX = math.ceil(arraysizeX/st)-1 #disks in X
    NY = math.ceil(arraysizeY/st)-1 #disks in Y
    print(NX,NY)
    Dsq = Device('SquareArray')
    circ = pg.circle(radius)
    sq = Dsq.add_array(circ, columns = NX, rows = NY, spacing = (st
    ,st))
    return Dsq


def hexagon(radius,width,arraysizeX,arraysizeY):
    st = 2*radius + width #calculates stepsize
    hw = hw = np.sqrt(st**2-(st/2)**2) #hexagonal half-width

    NX = math.ceil(arraysizeX/st)-1 #disks in X
    NY = math.ceil(arraysizeY/(2*hw))-1 #disks in Y
    print(NX,NY)

    Dhx = Device('HexagonalArray')
    circ = pg.circle(radius)
    hx1 = Dhx.add_array(circ,columns = NX, rows = NY, spacing = (st
    ,2*hw))
    hx2 = Dhx.add_array(circ,columns = NX, rows = NY, spacing = (st
    ,2*hw)).move([st/2,hw])
    return Dhx

radius = 0.05 #radius of disks

arrX = 95 #size of array in X
arrY = 95 #size of array in Y

width = 0.04 #minimum space between each disk

Square = square(radius,width,arrX,arrY)
Hexagonal = hexagon(radius,width,arrX,arrY)

Square.write_gds('40square95um.gds',precision=1e-12)
Hexagonal.write_gds('40hexagonal95um.gds',precision=1e-12)
```

A.2 Disk Analysis

The code used for disk analysis is presented below.

```
import numpy as np
import matplotlib.pyplot as plt
from matplotlib import rc
rc('font',**{'family':'serif','serif':['Palatino'],'size': 14})
rc('text', usetex=True)

def dataReader(textfile):
    #Returns a list of data from .txt file
    data = np.genfromtxt(textfile,delimiter='\t')


    major, minor, area, angle, listy = (np.zeros(len(data)) for i
   in range(5))

    for i in range(len(data)-1):
        major[i] = data[i+1][7]
        minor[i] = data[i+1][8]
        area[i] = data[i+1][1]
        angle[i] = data[i+1][9]
        listy[i] = i

    #Removing Outliers

    mean = np.mean(major)
    standardDeviation = np.std(major)
    print('The standard deviation is ',standardDeviation)

    distanceFromMean = abs(major - mean)
    maxDeviations = 1.5
    notOutlier = distanceFromMean < maxDeviations *
   standardDeviation

    newMajor = major[notOutlier]
    newMinor = minor[notOutlier]
    newArea = area[notOutlier]
    newAngle = angle[notOutlier]
    newListy = listy[notOutlier]

    data = []
    data.append(newMajor)
    data.append(newMinor)
    data.append(newArea)
    data.append(newAngle)
    data.append(newListy)

    lengthBefore = len(major)
    lengthAfter = len(newMajor)
```

```
46      lengthDifference = lengthBefore - lengthAfter
47      print('Removed ',lengthDifference,' elements.')
48
49      return data
50
51  def analyzeSizes(data):
52      avgMajor = sum(data[0])/len(data[0])
53      avgMinor = sum(data[1])/len(data[1])
54
55      ideal = []
56      for i in range(len(data[4])):
57          ideal.append(0.00785)
58
59      plt.scatter(data[4],data[2],color = color1)
60      plt.plot(data[4],ideal,color = color2)
61
62      plt.xlabel('Particle Number')
63      plt.ylabel('Area')
64      plt.show()
65
66      return avgMajor,avgMinor
67
68  def analyzeEllipticity(data):
69      el = []
70      major = data[0]
71      minor = data[1]
72      angle = data[3]
73
74      for i in range(len(major)):
75          el.append(major[i]/minor[i])
76
77      averageEllipticity = sum(el)/len(el)
78
79      plt.scatter(angle,el)
80      plt.xlabel('Angle')
81      plt.ylabel('Ellipticity')
82      plt.show()
83
84      return averageEllipticity
85
86  def createPolarBarChartAngles(data):
87      #Create Polar Bar Chart for distibution of angles
88      N = 15
89      divide = int(180/N)
90      angle = data[3]
91
92      bars = []
93      averageAngles = []
94      radii = []
95
96      for i in range(N):
```

```
        angles = []
        avg = (i*divide+divide*i+divide)/2
        averageAngles.append(avg*np.pi/180)

        for j in range(len(angle)):
            if angle[j] > i*divide and angle[j] < divide*i+divide:
                angles.append(angle[j]*np.pi/180)

        bars.append(angles)
        radii.append(len(angles))

    for i in range(len(averageAngles)):
        averageAngles.append(averageAngles[i]+np.pi)
        radii.append(radii[i])

    theta = averageAngles

    width = np.pi / N

    ax = plt.subplot(111, projection='polar')
    ax.bar(theta, radii, width=width, bottom=0, color=color1, alpha
   =1,edgecolor=color2)

    plt.show()

    data = dataReader('AJ-results.txt')
    size = np.mean(dataD1[2])
    print('The average particle size is: ',size,'um^2')
    mx,mi = analyzeSizes(dataD1)
    el = analyzeEllipticity(dataD1)
    createPolarBarChartAngles(dataD1)
```

A.3 Plotting Hysteresis Curves

```
import numpy as np
import pandas as pd

from sklearn.linear_model import LinearRegression
import matplotlib.pyplot as plt
import statsmodels.api as sm


from matplotlib import rc
rc('font',**{'family':'serif','serif':['Palatino'],'size': 12})
rc('text', usetex=True)

#colors
color1 = '#FBE6C5'
color2 = '#F5BA98'
```

```
color3 = '#EE8A82'
color4 = '#DC7176'
color5 = '#C8586C'
color6 = '#9C3F5D'
color7 = '#70284A'
color8 = '#542059'
color9 = '#2A204A'
color10 = '#222024'

AreaDisk = np.pi*(50e-9)**2
thickness = 20e-9
NoDisks = 460*678*678
totVol = AreaDisk * thickness * NoDisks

PermalloyMsat = 860e3 #A/m^2
PermalloyMomentSat = PermalloyMsat*totVol

def dataReader(textfile):
    data = np.genfromtxt(textfile,delimiter=',',skip_header=0,
   skip_footer=3)
    return data

def informationExtract(data):
    magneticField = []
    moment = []

    for i in range(len(data)):
        magneticField.append(data[i][0]*1e3)
        moment.append(data[i][1])

    return magneticField, moment

def quickplotter(textfile):
    #Returns a list of data from .txt file
    data = dataReader(textfile)

    magneticField = []
    moment = []

    for i in range(len(data)):
        magneticField.append(data[i][0])
        moment.append(data[i][1])

    plt.plot(magneticField,moment)
    plt.title(textfile)
    return

def normalize(moment,area):
    #area should be in m^2 as magneticField is in Am^2
    momentNorm = []

```

```
66      for i in range(len(moment)):
67          momentNorm.append(moment[i]/area)
68
69      return momentNorm
70
71  def removeBackground(dataSample,dataEmpty):
72      #Filter away diamagnetic contribution
73      newDataSample = []
74      for i in range(len(dataSample)):
75          newDataSample.append(dataSample[i]-dataEmpty[i])
76
77      return newDataSample
78
79  def coercivityData(mField,mMoment):
80
81      coercivity = []
82      tc = []
83      tempCoercivity = []
84
85      for i in range(len(mField)-1):
86          if (mMoment[i] > 0 and mMoment[i+1] < 0) or (mMoment[i] < 0
        and mMoment[i+1] > 0):
87              tempCoercivity.append(mField[i])
88
89
90      if len(tempCoercivity) > 2:
91          negative = []
92          positive = []
93
94          for i in range(len(tempCoercivity)):
95              if tempCoercivity[i] < 0:
96                  negative.append(tempCoercivity[i])
97              elif tempCoercivity[i] > 0:
98                  positive.append(tempCoercivity[i])
99
100         tc.append([np.mean(negative),np.mean(positive)])
101
102     else:
103         tc.append(tempCoercivity)
104
105     for i in range(len(tc)):
106         coercivity.append(tc[i][1])
107
108     return coercivity
109
110 def projectMoment(mField,mMoment,pos,plotyes):
111     #mMoment is a list of moments, mField is field strength
112     #Returns yfit, the
113
114     moment = []
115     field = []
```

```
116
117     if pos == "positive":
118         #Filtering relevant range
119         for i in range(len(mField)-1):
120             if mField[i] > 20:
121                 moment.append(mMoment[i])
122                 field.append(mField[i])
123     elif pos == "negative":
124         for i in range(len(mField)-1):
125             if mField[i] < -20:
126                 moment.append(mMoment[i])
127                 field.append(mField[i])
128
129     x = np.array(field)[:]
130
131     y = np.array(moment)[:]
132
133     model = LinearRegression(fit_intercept=True)
134
135     model.fit(x[:, np.newaxis], y)
136
137     xfit = np.linspace(0, 500,1000)
138     yfit = model.predict(xfit[:, np.newaxis])
139
140     #print("Model slope:    ", model.coef_[0])
141     #print("Model intercept:", model.intercept_)
142     if plotyes == True:
143
144         plt.scatter(x, y)
145         plt.plot(xfit, yfit)
146         plt.ylim(min(y),max(y))
147         plt.xlim(-50,max(x))
148         plt.show()
149
150     projectedPoint = model.intercept_
151
152     return model.coef_[0]
153
154 def line(slope):
155     #Creates a line with with slope and origin in origo
156     line = []
157
158     for i in range(-50,50):
159         line.append(slope*(i))
160         line.append(slope*(i+0.5))
161
162     for i in range(-50,50):
163         line.append(slope*(-i))
164         line.append(slope*(-i+0.5))
165
166     return line
```

```
167
168 def centerY(field,moment):
169     #CENTERS GRAPH ON Y-AXIS
170
171     #normMoment with fields [-500,-200] and [200,500]
172
173     centeredMoment = []
174
175     minMoment = []
176     maxMoment = []
177
178     for i in range(len(moment)):
179
180         if field[i] < -20:
181             minMoment.append(moment[i])
182         elif field[i] > 20:
183             maxMoment.append(moment[i])
184
185
186     avgMin = np.mean(minMoment)
187     avgMax = np.mean(maxMoment)
188
189     diff = (avgMin + avgMax)/2
190
191     for i in range(len(moment)):
192         centeredMoment.append(moment[i]-diff)
193
194     return centeredMoment
195
196 def centerX(field,moment):
197     #CENTERS GRAPH ON X-AXIS
198     cField = []
199
200     for i in range(len(field)-1):
201         if (moment[i] > 0 and moment[i+1] < 0) or (moment[i] < 0
    and moment[i+1] > 0):
202             cField.append(field[i])
203
204     if len(cField) > 2:
205         positive = []
206         negative = []
207
208         for i in range(len(cField)):
209             if cField[i] > 0:
210                 positive.append(cField[i])
211             else:
212                 negative.append(cField[i])
213
214         k =  (np.mean(positive)+np.mean(negative))/2
215     else:
216         k = np.mean(cField)
```

```
217
218     centeredField = []
219
220     for i in range(len(field)):
221         centeredField.append(field[i]-k)
222
223     return centeredField
224
225
226 def curveFix(field,moment):
227     #Should rotate the graphs and center about y-axis and x-axis
228
229     #ROTATION
230     slopePos = projectMoment(field,moment,'positive',False)
231     slopeNeg = projectMoment(field,moment,'negative',False)
232
233     linePos = line(slopePos)
234     lineNeg = line(slopeNeg)
235
236     avgLine = []
237     for i in range(len(linePos)):
238         avgLine.append((linePos[i]+lineNeg[i])/2)
239
240     tempMoment = []
241     for i in range(len(moment)):
242         tempMoment.append(moment[i]+avgLine[i])
243
244     #CENTERING
245     centeredMoment = centerY(field,tempMoment)
246     centeredField = centerX(field,centeredMoment)
247
248     correctedMoment = centeredMoment
249     correctedField = centeredField
250
251     return correctedMoment,correctedField
252
253 def plotAll(field,moment,yaxis,xaxis):
254     for i in range(len(field)):
255
256         deg = i*5
257
258         name = str(deg) +'degrees.png'
259
260         plt.plot(field[i],moment[i],color=color5)
261         plt.xlabel(xaxis)
262         plt.ylabel(yaxis)
263         plt.ylim(-1.5,1.5)
264         plt.xlim(-60,60)
265         plt.title(name)
266         plt.savefig(name, format='png', dpi=800)
267         plt.show()
```

```
268
269 def satMoment(field,moment):
270     momentSat = []
271
272     for i in range(len(field)):
273         msat = []
274         for j in range(len(field[i])):
275             if field[i][j] < -20:
276                 msat.append(abs(moment[i][j]))
277             elif field[i][j] > 20:
278                 msat.append(moment[i][j])
279
280         momentSat.append(np.mean(msat))
281
282     return momentSat
283
284 #READS IN DATA AND REMOVES DIAMAGNETIC CONTRIBUTION
285 data = []
286
287 data.append(dataReader('rot180-0.txt'))
288 data.append(dataReader('rot180-1.txt'))
289 data.append(dataReader('rot180-2.txt'))
290 data.append(dataReader('rot180-3.txt'))
291 data.append(dataReader('rot180-4.txt'))
292 data.append(dataReader('rot180-5.txt'))
293 data.append(dataReader('rot180-6.txt'))
294 data.append(dataReader('rot180-7.txt'))
295 data.append(dataReader('rot180-8.txt'))
296 data.append(dataReader('rot180-9.txt'))
297 data.append(dataReader('rot180-10.txt'))
298 data.append(dataReader('rot180-11.txt'))
299 data.append(dataReader('rot180-12.txt'))
300 data.append(dataReader('rot180-13.txt'))
301 data.append(dataReader('rot180-14.txt'))
302 data.append(dataReader('rot180-15.txt'))
303 data.append(dataReader('rot180-16.txt'))
304 data.append(dataReader('rot180-17.txt'))
305 data.append(dataReader('rot180-18.txt'))
306 data.append(dataReader('rot180-19.txt'))
307 data.append(dataReader('rot180-20.txt'))
308 data.append(dataReader('rot180-21.txt'))
309 data.append(dataReader('rot180-22.txt'))
310 data.append(dataReader('rot180-23.txt'))
311 data.append(dataReader('rot180-24.txt'))
312 data.append(dataReader('rot180-25.txt'))
313 data.append(dataReader('rot180-26.txt'))
314 data.append(dataReader('rot180-27.txt'))
315 data.append(dataReader('rot180-28.txt'))
316 data.append(dataReader('rot180-29.txt'))
317 data.append(dataReader('rot180-30.txt'))
318 data.append(dataReader('rot180-31.txt'))
```

```
data.append(dataReader('rot180-32.txt'))
data.append(dataReader('rot180-33.txt'))
data.append(dataReader('rot180-34.txt'))
data.append(dataReader('rot180-35.txt'))
data.append(dataReader('rot180-36.txt'))

tempField = []
tempMoment = []

#READS IN DIAMAGNETIC CONTRIBUTION FROM EMPTY SAMPLE HOLDER
data1 = dataReader('emptySample.txt')
data2 = dataReader('emptySample90.txt')

mField1,moment1 = informationExtract(data1)
#plt.plot(mField1,moment1)

mField2,moment2 = informationExtract(data2)
#plt.plot(mField2,moment2)

background = []

#Averaging background for both angles
for i in range(len(moment1)):
    background.append((moment1[i]+moment2[i])/2)

#Removing background from signal
for i in range(len(data)):

    tempField2,tempMoment2 = informationExtract(data[i])
    removeBackgroundMoment = removeBackground(tempMoment2,
   background)

    tempField.append(tempField2)
    tempMoment.append(removeBackgroundMoment)

plt.axhline(y=0, color=color10, linewidth = 1, linestyle='-')
plt.axvline(x=0, color=color10, linewidth = 1, linestyle='-')
plt.plot(field[0],moment[0],color=color8,label='0 degrees')
plt.plot(field[36],moment[36],color=color2,label='180 degrees')

plt.xlabel('Applied Field [mT]')
plt.ylabel('Magnetic Moment [Am$^2$]')
plt.xlim(-60,60)
plt.legend()
plt.title('Hysteresis Curves of DEC20-2')
plt.savefig('beforeNorm.png', format='png', dpi=800, bbox_inches='
   tight')
plt.show()

#PLOTS SAMPLE DIAMAGNETIC RESPONSE
plt.axhline(y=0, color=color10, linewidth = 1, linestyle='-')
```

```
plt.axvline(x=0, color=color10, linewidth = 1, linestyle='-')
plt.plot(mField1,moment1,color=color7,label='0 degrees')
plt.plot(mField2,moment2,color=color3,label='90 degrees')

plt.xlabel('Applied Field [mT]')
plt.ylabel('Magnetic Moment [Am$^2$]')
plt.xlim(-60,60)
plt.legend()
plt.title('Hysteresis of Empty Holder')
plt.savefig('EmptyHolder.png', format='png', dpi=800, bbox_inches='
    tight')
plt.show()

#DATA FIX
field = []
moment = []

for i in range(len(data)):
    m,f = curveFix(tempField[i],tempMoment[i])
    field.append(f)
    moment.append(m)

#PLOTS SATURATION MOMENT AND COERCIVITY OVER ALL ANGLES
coercivity = []
for i in range(len(data)):
    coerc = coercivityData(field[i],moment[i])

    coercivity.append(coerc)

degrees = []

for i in range(len(data)):
    degrees.append(i*5)


plt.plot(degrees,coercivity,color=color5)
plt.xlabel('Degrees')
plt.ylabel('Coercive Field [mT]')
plt.title('Coercivity over Measurement Rounds')
plt.savefig('Coercivity.png', format='png', dpi=800, bbox_inches='
    tight')
plt.show()

#0deg
plt.axhline(y=0, color=color10, linewidth = 1, linestyle='-')
plt.axvline(x=0, color=color10, linewidth = 1, linestyle='-')
plt.plot(field[0],normMoment[0],color=color8,label='0 degrees')

plt.xlabel('Applied Field [mT]')
plt.ylabel('Normalized Moment')
plt.xlim(-60,60)
```

```
plt.title('Normalized Hysteresis Curves for 0 Degree Rotation')
plt.savefig('0deg.png', format='png', dpi=800, bbox_inches='tight')
plt.show()

#90deg
plt.axhline(y=0, color=color10, linewidth = 1, linestyle='-')
plt.axvline(x=0, color=color10, linewidth = 1, linestyle='-')
plt.plot(field[18],normMoment[18],color=color5,label='90 degrees')

plt.xlabel('Applied Field [mT]')
plt.ylabel('Normalized Moment')
plt.xlim(-60,60)
plt.title('Normalized Hysteresis Curves for 90 Degree Rotation')
plt.savefig('90deg.png', format='png', dpi=800, bbox_inches='tight'
    )
plt.show()

#180deg
plt.axhline(y=0, color=color10, linewidth = 1, linestyle='-')
plt.axvline(x=0, color=color10, linewidth = 1, linestyle='-')
plt.plot(field[36],normMoment[36],color=color2,label='180 degrees')

plt.xlabel('Applied Field [mT]')
plt.ylabel('Normalized Moment')
plt.xlim(-60,60)
plt.title('Normalized Hysteresis Curves for 180 Degree Rotation')
plt.savefig('180.png', format='png', dpi=800, bbox_inches='tight')
plt.show()

#PLOT ALL ANGLES
plotAll(field,normMoment,'Normalized Magnetization','Applied field
    [mT]')
```

Appendix B

Micrographs and Outlines

The presented code was run on data from the analysis of micrographs in Fiji. Micrographs and outlines used in the analysis is presented below.

IPA test

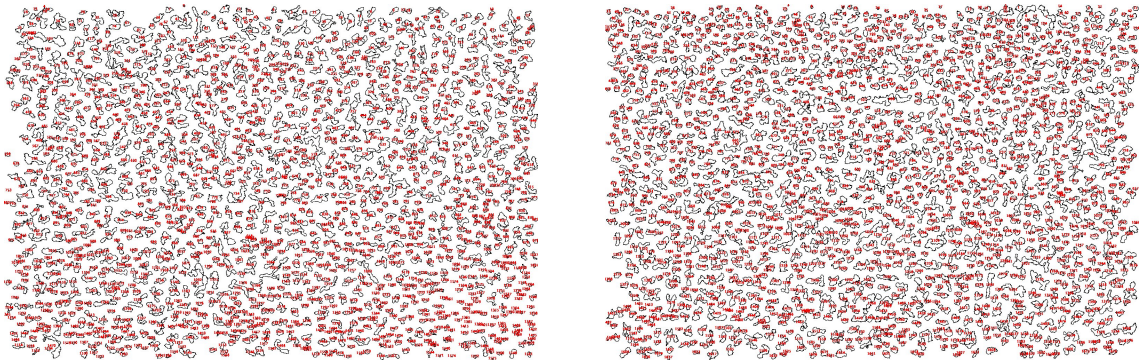

(a) OCT20-2A **(b)** OCT20-2B

Figure B.1: Outlines of particles from Fiji

Exposure Dose Analysis

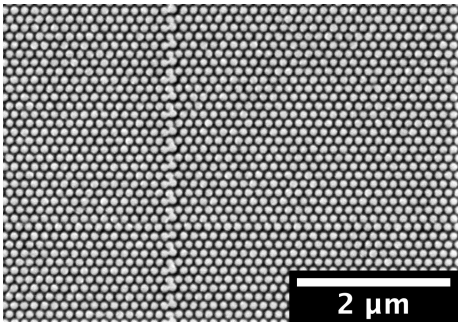

(a) Image of Dose 2 = 220 µC/cm²

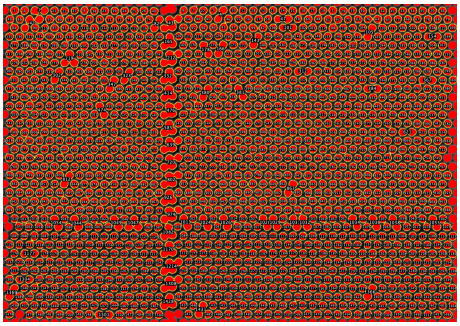

(b) Overlay of Dose 2 = 220 µC/cm²

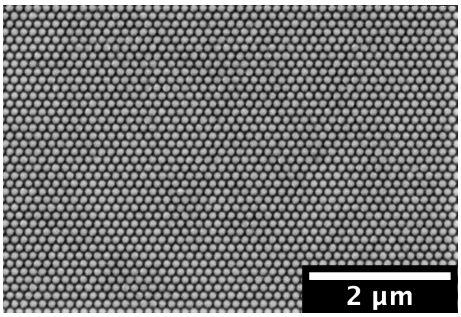

(c) Image of Dose 3 = 240 µC/cm²

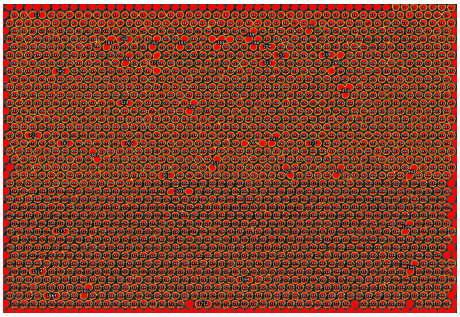

(d) Overlay of Dose 3 = 240 µC/cm²

Figure B.2: Micrographs and overlays from Fiji of DEC20-1A

Metalization

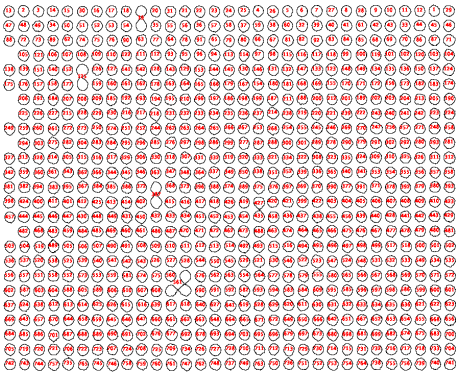

(a) DEC20-1A

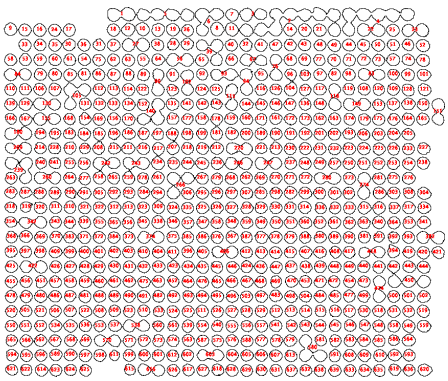

(b) DEC20-1B

Figure B.3: Outlines of disks from Fiji

Large Sample Analysis

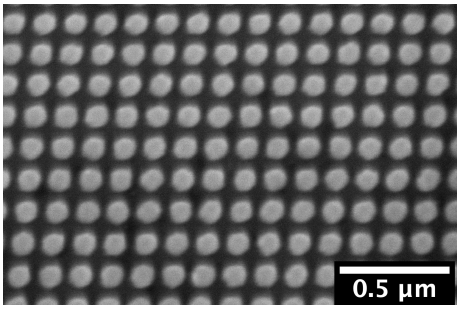

(a) North Micrograph

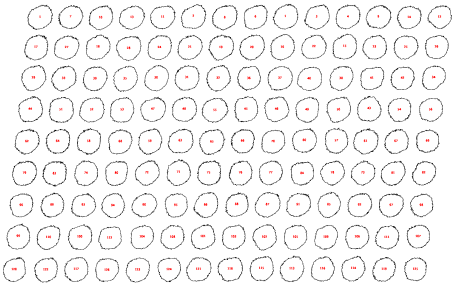

(b) North Outline

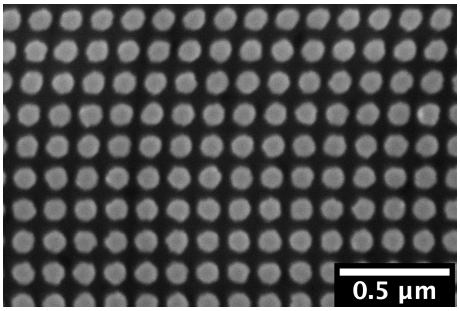

(c) South Micrograph

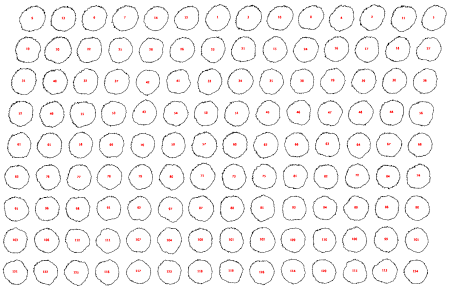

(d) South Outlines

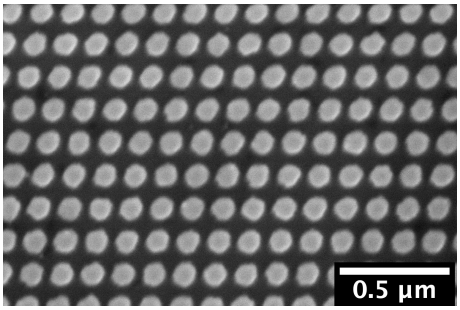

(e) West Micrograph

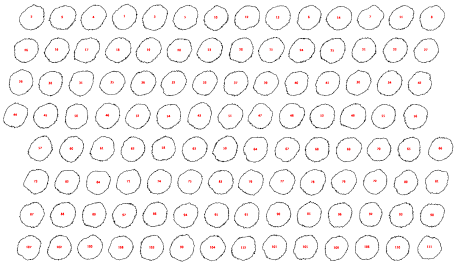

(f) West Outlines

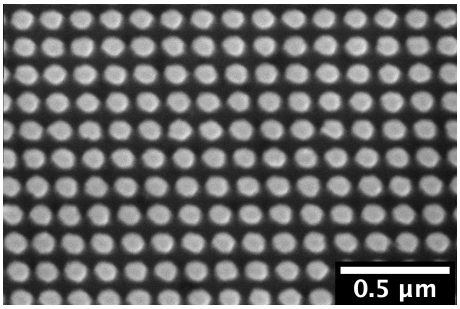

(g) Middle Micrograph

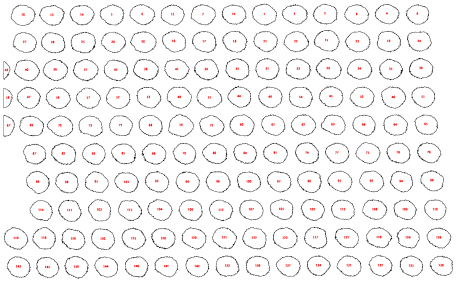

(h) Middle Outline

Figure B.4: Micrographs and outlines of DEC20-2 at different locations on the sample